Steam temperature and flow maldistribution in superheater headers

Prepared by:

Jean-Pierre du Preez

DPRJEA008

Department of Mechanical Engineering

University of Cape Town

Supervisor:

Professor P.G. Rousseau

Industrial Mentor:

Alton Naidoo

September 2019

Submitted to the Department of Mechanical Engineering at the University of Cape Town in complete fulfilment of the academic requirements for a Master of Science degree in Mechanical Engineering

Key Words: Final superheater headers, thermal stress, CFD, FEA.

Abstract

Heat exchangers and steam headers are at the heart of any boiler and are susceptible to a range of failures including tube leaks, ligament cracking, creep and fatigue. These common forms of header failure mechanisms can be exacerbated by local thermal stresses due to temperature and flow maldistribution at full and partial boiler load operations.

The purpose of this project is to develop process models of the outlet stubbox header of a final superheater (FSH) heat exchanger in a 620MW coal-fired drum type boiler. The process models were used to assess the impact of steam flow and temperature distribution on the thermal stresses in the header material. The process models were developed using Computational Fluid Dynamics (CFD) and Finite Element Analysis (FEA). Thermocouples were installed at key locations on the stubbox headers to monitor metal temperatures and the measured metal temperatures served as boundary values and for validation of the CFD results.

The thermocouple data was analysed for three different steady state boiler loads, namely full load, 80% load and 60% load. It showed that the temperature distribution across these headers was not uniform, with a maximum temperature difference across the outlet stubbox of 40℃ at full load and 43℃ at partial loads. Other relevant power plant data, such as steam pressure, was provided from the power plant's Distributed Control System (DCS) and was used as boundary conditions for the CFD models. The exact mass flow distribution across the inlet stubs of the outlet stubbox header was unknown and was estimated using a CFD model of the inlet stubbox header and steam mass flow values from power plant's DCS system.

A CFD model was created for each of the three boiler loads at steady state conditions. The CFD results provided the metal temperature profile, internal steam temperature distribution and pressure distribution across the header. The CFD solid temperatures were validated using the thermocouple readings and found to be in agreement. The CFD results were exported to the FEA models, where specific displacement constraints for thermal expansion were utilised. The FEA models were used to assess the extent of thermal stresses due to thermal expansion only, as well as stresses due to thermal expansion combined with internal pressure.

High local stresses were found at the borehole crotch corners of the rear outlet branch and inlet stubs. However, these are below 0.2% proof strength at elevated temperatures. The high local stresses thus did not result in local plastic deformation but contribute to exacerbate steady state failure mechanisms such as creep.

Declaration

I, *Jean-Pierre du Preez*, hereby declare the work contained in this dissertation to be my own. All information which has been gained from various journal articles, text books or other sources has been referenced accordingly. I have not allowed, and will not allow, anyone to copy my work with the intention of passing it off as their own work or part thereof.

Signed by candidate

2019/09/10

Jean-Pierre du Preez Date

Acknowledgements

I would like to thank the following people for their support and contribution throughout the thesis.

Prof Pieter Rousseau who constantly provided direction, motivation and technical support. Imparting the necessary knowledge to enable me to complete the work.

Babcock for funding my post graduate studies as well as flights down to Cape Town when it was required to be present at UCT.

The EPPEI programme for allowing me to partake in a post graduate program that was practical and relevant to power plant problems.

To Eskom, and especially RT&D, who gave permission and funded the installation of thermocouples at a specified 620MW coal-fired power plant.

My family, wife and friends who were patient and encouraged me through all the late nights over the years.

Lastly and most importantly, I want to thank Yeshua my saviour for the blessings, strength and opportunity.

Table of Contents

List of Figures

List of Tables

List of Nomenclature

General symbols

A	Area [mm]
A_s	Surface area [mm^2]
$[B]$	Geometric matrix in FEA thermal expansion
c_p, C	Specific Heat [J/kgK]
D, d	Diameter [mm]
$[D]$	Elastic modulus matrix in FEA thermal expansion
$\{d\}$	Nodal displacement vector
D_i	Inside diameter [mm]
E	Young's Modulus [GPa]
e	Energy per unit mass [J/kg]
$\Delta E_{element}$	Change of energy content in an element [J]
e_{ms}	Header thickness [mm]
e_{mb}	Branch thickness [m]]
f	Darcy friction factor
F_{pp}	Physical fluid factor
F_T	Temperature factor
$[f_T]$	Global force matrix
G	Steam mass flux [lb/hft^2] or [kg/ m^{2}s]
h	Heat transfer coefficient [W/m^{2}K]
h_i, h_1	Steam-side forced convection [W/m^{2}K]
h_1'	Basic convection velocity and geometry factor for longitudinal flow
k	Thermal conductivity [W/mK]
[K]	Stiffness matrix FEA
L	Length [mm]
N_u	Nusselt number
ΔP	Pressure drop [Pa]
P_i	Internal pressure [Pa]
P_0	External pressure [Pa]
P_r	Prandtl number
$\dot{Q}_{conduction}$	Conduction heat transfer rate [W]
$\dot{Q}_{conv}$	Convection heat transfer rate [W]
$\dot{Q}_{element}$	Rate of heat generation in a rectangular element [W]
$\dot{q}$	Heat flux [W/m^2]

$\dot{Q}_x, \dot{Q}_y, \dot{Q}_z$	Rate of heat conduction at x, y & z [W]
r	Cylinder radius [m]
r_2, r_o	Radius at outer wall of a tube [m]
r_1, r_i	Radius at inner wall of a tube [m]
R_e	Reynolds number
T	Temperature [K]
ΔT	Temperature difference [K]
t	FEA element thickness [mm]
Δt	Change in time or rate of change [s]
T_2	Outer wall temperature of tube [K]
T_1	Inner wall temperature of tube [K]
T_b	Bulk fluid temperature [K]
T_f	Film temperature [K]
T_m	Mean fluid temperature [K]
T_s	Surface temperature [K]
T_t	Temperature at a specific time [K]
T_∞	Ambient temperature [K]
$u_{elastic}(r)$	Radial displacement [m]
v	Poisson ratio
$\vec{V}$	Vector velocity
$V_{element}$	Volume of element
V_m	Mean velocity [m/s]
x, y, z	Dimensions in Cartesian coordinate system [m]

Greek symbols

α	Thermal expansion [10^{-6}/K]
β, γ	Distance in Cartesian coordinate system between FEA nodes [mm]
ε	Equivalent roughness value
ε_{creep}	Creep strain
$\varepsilon_{elastic}$	Elastic strain due to mechanical loads
$\varepsilon_r(r)$	Radial strain due to pressure
ε_T	Strain due to temperature increase across FEA element
$\varepsilon_{thermal}$	Thermal strain
ε_{total}	Total strain
$\varepsilon_\theta(r)$	Tangential elastic strain
μ	Dynamic viscosity [kg/ms]

ρ	Density [kg/m^3]
σ	Thermal stress [Pa]
$\sigma_r(r)$	Radial stress due to pressure [Pa]
$\sigma_{rt}(r)$	Radial stress due to thermal expansion through the cylinder thickness [Pa]
$\sigma_\theta(r)$	Hoop stress due to pressure [Pa]
$\sigma_{\theta t}(r)$	Hoop stress due to thermal expansion through the cylinder thickness [Pa]
σ_z	Axial stress due to pressure [Pa]
$\sigma_{zt}(r)$	Axial stress due to thermal expansion through the cylinder thickness [Pa]
τ	Shear and normal stresses acting on fluid [Pa]
Φ	Heat per unit volume [J/K/m^3]

Acronyms and Abbreviations

ASME	American Society of Mechanical Engineers
CFD	Computational Fluid Dynamics
DCS	Distributed Control System
EPPEI	Eskom Power Plant Engineering Institute
FEA	Finite Element Analysis
FEM	Finite Element Modelling
HEX	Hexahedral elements
MW	Mega Watt
TET	Tetrahedral elements

1. Introduction

1.1 Background

Heat exchangers and steam headers are at the heart of any boiler. Heat exchangers are used in power generation boilers to exchange heat from combustion gasses to the steam circuit flowing inside the heat exchangers. These heat exchangers are called indirect contact heat exchangers as the two fluids do not mix; rather the heat energy is exchanged between the gas and the steam though a heat transfer surface [1]. In most cases, the heat transfer surfaces consist of tube walls with the tubes attached in a specific configuration to their associated inlet and outlet headers. The hot combustion gasses, or flue gasses, flow across (crossflow configuration) these tubes and transfers heat via convection and radiation. The heat is then transferred from the surface of the tubes, through the tube wall and into the steam via conduction and convection. The heated steam then proceeds to the outlet header where it will either be directed to the next heat exchanger, to be heated further, or to the steam turbines.

The focus of this thesis is on the outlet headers of the final superheater heat exchangers of a 620MW coal-fired power plant with a drum type boiler. Figure 1-1 shows the process flow of the steam circuit before the steam enters the high-pressure turbine. The flue gas passes across the heat exchanger elements before entering the rear pass of the boiler. The steps for the process flow are as follows:

1. Steam enters the front and rear platen superheaters from the outlet of the primary superheater.
2. Steam exits the front and rear platen superheaters.
3. Steam enters the final superheater
4. Steam exits the final superheater, passes through the outlet stubbox and passes to the outlet manifold headers. From the manifold headers the steam flows into the main steam pipe network which feeds the high-pressure turbine with superheated steam.

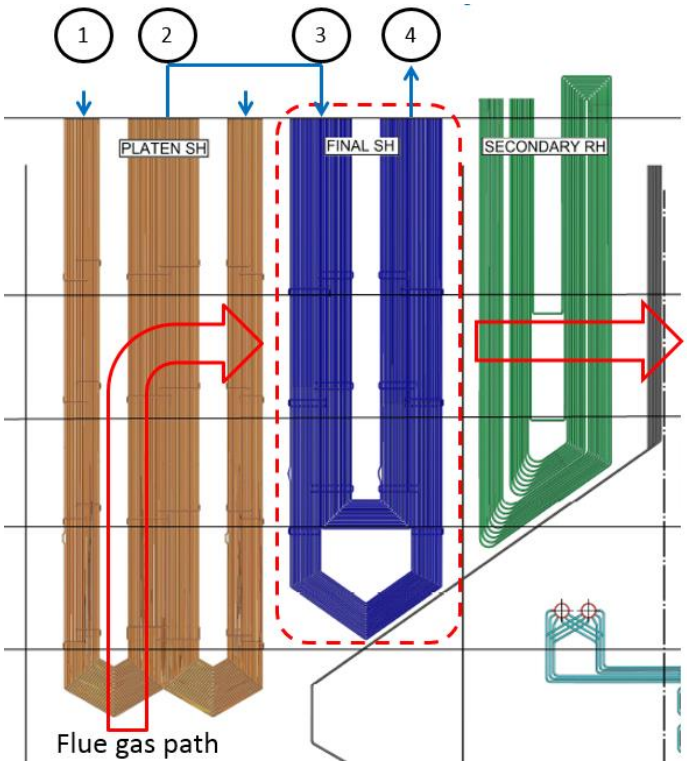

Figure 1-1: Process flow of the superheater steam circuit.

The final superheater element together with its inlet and outlet stubbox headers are shown in Figure 1-2. As shown in Figure 1-1 above, the steam enters the inlet stubbox header, flows through the element and exits through the outlet stubbox header.

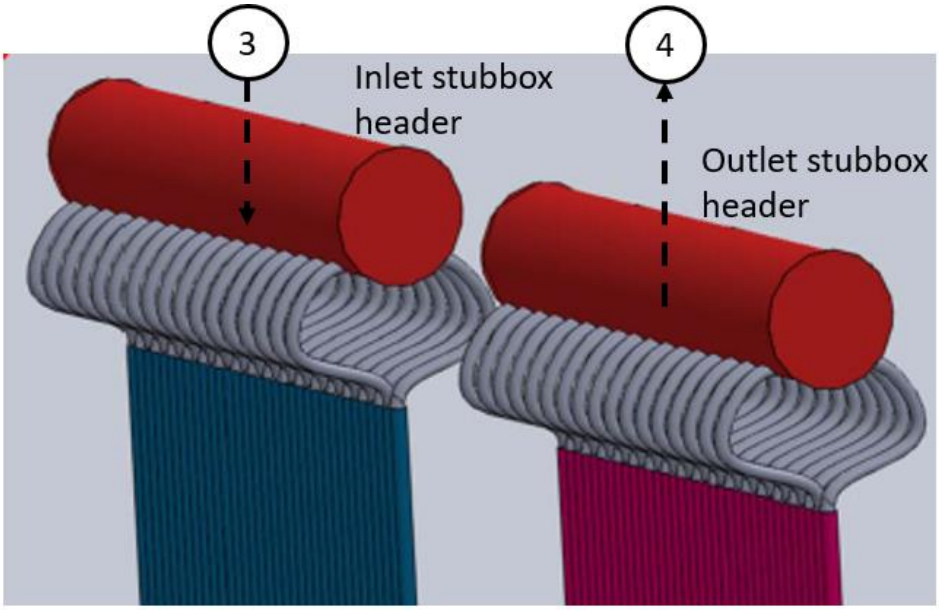

Figure 1-2: Inlet and outlet stubbox headers.

The steam leaves the outlet stubbox headers and enters one of two outlet manifold headers situated at the top in the penthouse.

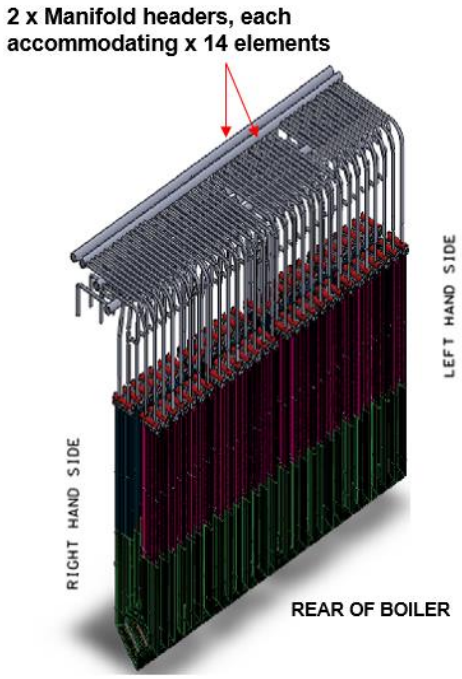

Figure 1-3: Final superheater elements and manifold headers.

1.2 Motivation

The Energy Efficiency group of the Eskom Power Plant Engineering Institute (EPPEI), which is hosted at the University of Cape Town, has been striving to develop various process models for the different components and systems within power plants. The goal of each process model is to assist in providing a better understanding of the operation of the components and their associated failure mechanisms. Each process model focuses on specific process conditions and specific failure mechanisms. This dissertation focuses on the final superheater outlet stubbox of a final superheater heat exchanger. The end goal is to use these various models in order to capture a more holistic view of boiler performance and to predict a wider range of failures. This dissertation will assist that goal by focusing on the extent of temperature and flow maldistribution and how it contributes to stresses in the outlet header.

1.3 The research problem

Understanding the impact of steam temperature and flow maldistribution on the header's temperature distribution is crucial, especially in terms of understanding ligament cracking. Cracking often occurs on the internal surface at the boreholes of the header and has been identified as one of the main contributors to header failures. There are many factors which influence the propagation and growth of ligament cracks, with one of the main factors being thermal stresses. The extent of temperature maldistribution across the header will influence the magnitude of thermal stresses. By using the current design of the final superheater outlet stubbox header, the magnitude of the

ligament stresses can be evaluated at steady state conditions. The simulations are performed for full load and partial load operations. Partial load conditions are important to evaluate as they are increasingly required from base load coal-fired power plants.

1.4 Research objectives:

I. Install thermocouples on the inlet stubbox, outlet stubbox and outlet manifold headers, for the purpose of capturing on-site temperature measurements. The effect of the attemperator spray on the steam distribution before the inlet of the superheater is not included in this dissertation.
II. Develop suitable CFD process models of the outlet stubbox by using the measured temperature data points as temperature boundary conditions. Pressure values were to be provided from power plant data.
III. Estimate the potential mass flow distribution across the outlet header using suitable process models and power plant mass flow data.
IV. Use the temperature profile calculated in the CFD model and perform a thermo-mechanical coupling with suitable FEA models.
V. Use FEA to find the steady state stresses due to a combination of mechanical (internal pressure) and thermal loading (thermal expansion).

2. Literature review

2.1 Common causes of superheater header damage

Over the years it has been found that the primary failure mechanism for superheater and reheater headers is cracking at the bore holes, where the header and ligaments are attached. Cracking can occur both inside the header's surface, between the bore holes, as well as on the outer surface where the stubs and other header attachments are located. Ligament cracking was first truly recognised in the UK during the 1980's. Large cracks, more than 50% of the wall depth, were found in superheater and reheater headers within very few start-ups (less than 500). Major costs were undertaken to replace the header material from 2.25Cr1Mo to P91, so as to increase creep resistance and decrease header thickness. The failure investigations found that ligament cracking is a function of bore hole spacing, header material, wall thickness and operating conditions. The arrangement of stubs plays a large role in header stress concentrations and rearranging the stubs from a straight to a diagonal set-up greatly reduces these stresses. [2]

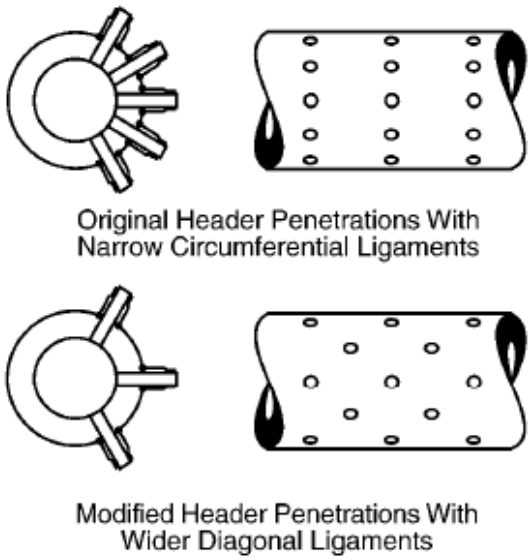

Figure 2-1: Improved ligament design [2].

Fabricius and Jackson [3] compiled a list of four different case studies of premature failure of P91 power plant headers. One of the case studies revolved around a failure of a high-pressure superheater manifold header in Europe. Both a creep life estimation and FEA analysis were performed on this header as per the British (BS) European (EN) 12952 pressure part codes. For this particular case study, the plant shifted between high and low loads and within 15000 hours the manifold header already showed signs of premature creep damage with indications <0.25 mm deep.

It was found that during low loads the header constantly reached metal temperatures as high as 650°C, which was much higher than its design temperature of 569°C. However, the elevated temperature alone could not explain the premature creep damage. FEA analysis showed that additional hoop stress concentrations were found at the T-joint connection to the header. From [3] it was concluded that joint geometries can, in some cases, be the root cause for premature creep damage.

Thielsch et.al [4] performed a case study on a superheater outlet header which failed due to a large circumferential crack. The crack was a severe ligament crack which spread around the full circumference, through each bore hole and penetrated the full cross-sectional wall. The header was made from P22 (10CrMo9-10 or 11CrMo9-10) material with an operating temperature of 540°C. Through several analytical and finite element analyses, it was found that the failure was due to thermal fatigue. High thermal gradients and mechanical stresses were found at the borehole of the tube, inside the header. Given enough time, with stresses caused by high thermal gradients and mechanical loads which were also cyclic in nature, the crack initiated and spread. The root cause of the failure was established as periodic overheating of the header, where any temperature fluctuation in the header greatly increased the stresses at the corner of the borehole.

Tilley [5] wrote a report describing the impact of operating factors on boiler availability. One of the key analysers used by plants is the Boiler Stress and Condition Analyser (BSCA) which is used to monitor accumulated creep and thermal fatigue damage on thick-walled pressure components such as headers. A combination of creep and fatigue damage is considered the main cause for damage and cracking in the headers. Thermal stresses which arise from transient thermal gradients can often exceed yield strength, causing plastic deformation. These permanent deformations together with creep strains can accelerate failures. Due to the high cost of header replacement, routine non-destructive testing is used to inspect the formation and spread of any indications.

Paterson and Wilson [6] described the importance of damage monitoring systems for life optimisation of power plant components. From Figure 2-2 below it can be seen that even a slight increase in temperature above design can significantly decrease the time until creep rupture and thus remaining header life.

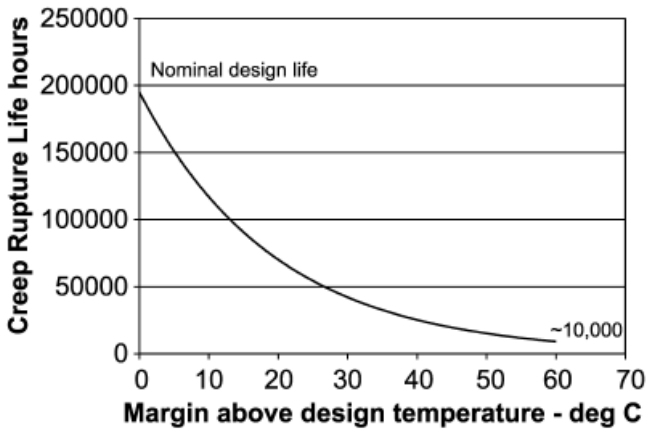

Figure 2-2: Effect of temperatures above design temperature on creep life [6].

In order to ensure satisfactory creep life at high operating temperatures and pressures, a large wall thickness is required. However, from Figure 2-3 it can be seen that superheater headers with large wall thicknesses, are more prone to crack initiations at a lower number of cycles.

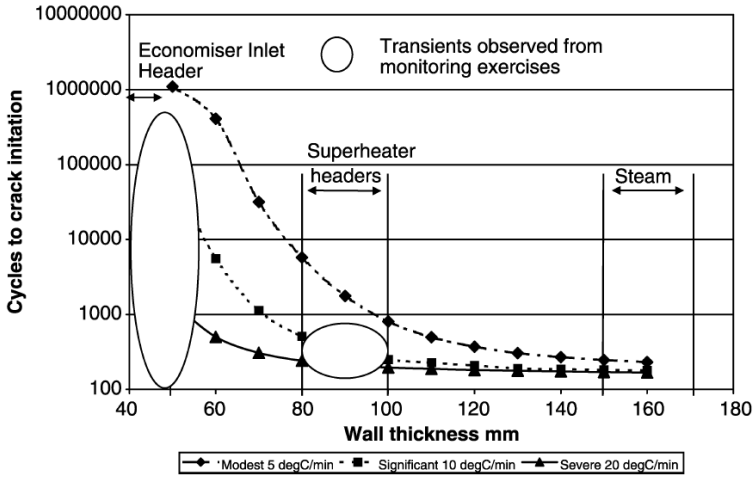

Figure 2-3: Cycles to crack initiation vs wall thickness [6].

Cycles are generally categorised between two types, namely up and down-shock cycles. Superheater outlet headers experience more damage during down-shock cycles. Figure 2-4 illustrates what happens during a down-shock cycle, by showing different points (A-E) which correspond to the temperature (a) and stress-strain (b) cycle. The stress at A is assumed to be zero, which is followed by a heat ramp up to point B. If the heat ramp is great enough then compressive yielding can occur at a stress-raising feature inside the header's surface (at any location where joints are connected to the header). The local stress occurs because a point on the surface attempts to expand due to the heat and is constrained by the rest of the cooler component. Rapid cooling takes places between point B and C which causes a tensile yielding at point C. Thermal stresses decrease on load (C-D) as extreme heat ramps are not present. As thermal stress relaxation takes place, creep strain

accumulates at fairly constant mechanical load and high temperatures which can lead to a damaging event. The creep-fatigue life assessment was performed using the R5 procedure [6].

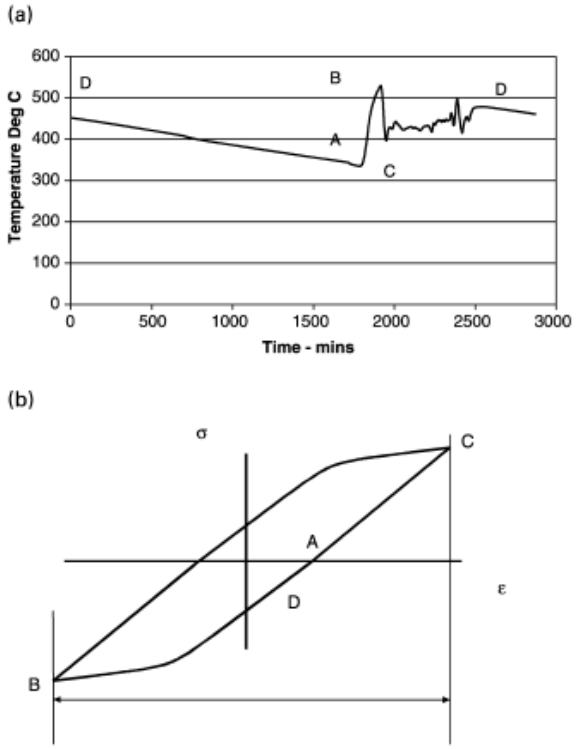

Figure 2-4: (a) Temperature change during transient down-shock, (b) stress-strain hysteresis loop for down-shock cycle [6].

King [7] investigated two cases where superheater outlet headers were experiencing severe cracking. In both cases, the circumferential cracks were primarily found between the header's tube holes. The cracks usually initiate on the inside surface where the stresses are the highest. The major contributor for the internal ligament cracks was identified as the cross-sectional thermal gradient over the header's wall thickness. During low load operations, the thermal gradient is higher as temperatures can vary significantly from element to element and from tube to tube. Figure 2-5 shows a wide circumferential crack in the header and through the borehole.

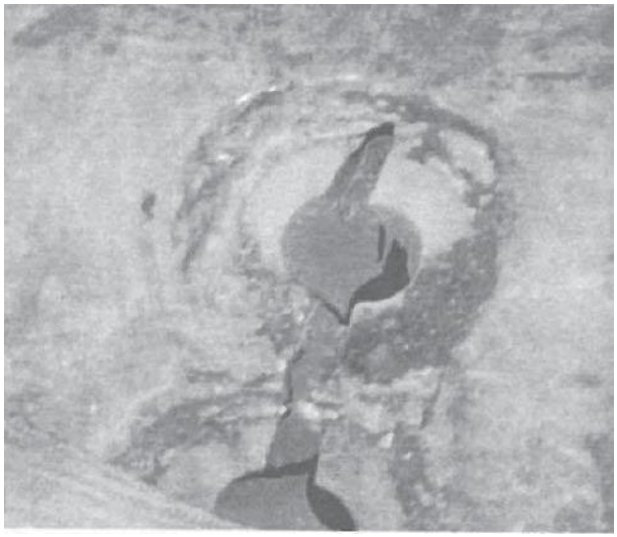

Figure 2-5:Wide circumferential crack in header [7].

In 1995 Babcock and Wilcox [8] performed a thorough investigation of several superheater outlet headers with cracks. For secondary superheater outlet headers as many as 22% of the headers were found to have had cracks after 20 years. The cracks were most commonly found at welds and ligament areas between tube-stub boreholes. See Figure 2-6 for crack progression between ligaments. The mechanisms which contribute to ligament crack initiation were identified as a combination of local creep and thermal fatigue damage. These two mechanisms are a result of significant thermal stresses that occur during load cycling and on/off operations. For headers to resist high pressures, large wall thicknesses are required. The drawback that was found was that an increase in wall thickness resulted in an increase in thermal gradient and thus thermal stresses. The higher the wall thickness, the higher the thermal stress through the wall. The highest local stresses due to internal pressure occur at geometry discontinuities such as header borehole penetrations. An FEA analysis was conducted and found that borehole locations influence the adverse effects of thermal stresses and temperature differences between the outlet legs and headers. The temperature difference leads to temperature maldistribution in the header material.

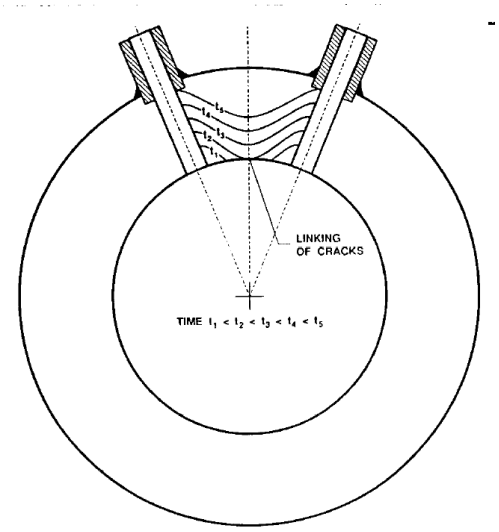

Figure 2-6: Progression of ligament cracking in header [8].

An expert structural integrity analysis [9] was performed on the Kogan Creek Reheater header. The unstable and fluctuating steam temperatures entering the header were acknowledged as being the main contributor to thermal fatigue damage and cracking. The analysis used a large collection of thermocouple data on key locations of the header to measure the extent of the fluctuation. The thermocouples were placed on the header stubs, outside the header, buried in the header (mid-wall) and inside the header to measure steam temperatures. The data from the mid-wall metal thermocouples was used to thermally calibrate steam and metal temperatures predicted in a FEA model. The calibration allowed identification of the surface heat transfer coefficients. A non-linear power law equation was created to correlate steam temperature ramp rates and overall temperature change to ligament stress. The stress values from the power law equation and FEA correlated well. The analysis proceeded to assess the creep-fatigue life and found that the time required before ligament cracks initiated significantly exceeded the life of the plant. It was concluded that cracking due to thermal fatigue was unlikely during the header's life.

An investigation was carried out to examine the failure of a platen superheater outlet header of a 210MW power plant [10]. After conducting macroscopic and microscopic examinations as well as finite element modelling, it was concluded that transient temperature fluctuations (minor, but large in number) and abnormal thermal shock (few but severe) are possible causes of fatigue cracks between the ligaments.

2.2 Temperature maldistribution in headers

Due to various reasons, which include combustion and steam flow parameters of a specific power station, temperature maldistribution can occur in a header. The tubes in the superheater element can experience different steam flows and can combine with a variation of gas temperature to result in significant temperature variations across the tubes. Together with a temperature variation across

the tubes an even larger variation can occur between the header's overall temperature and the tube legs connected to the header. There can be a mismatch between the steam temperature in the boreholes and the main cavity of the header at the same location. From Figure 2-7, it can be seen that it is not uncommon for the header and tube legs to have a temperature difference of up to 39°C [8].

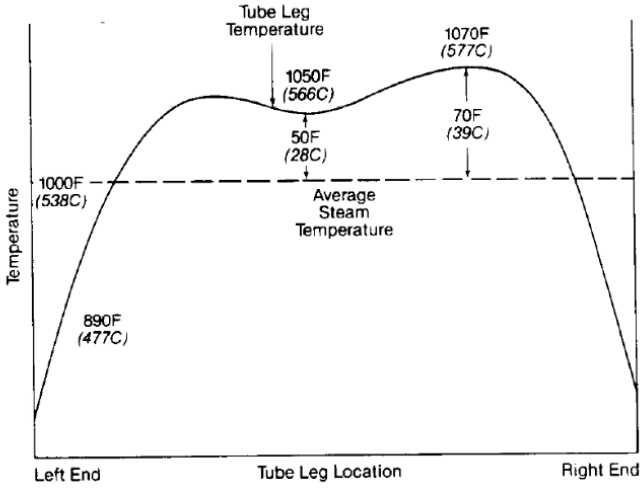

Figure 2-7: Temperature difference- header and tube legs [8].

Transient conditions such as start-ups and shut-downs are prone to worsen temperature variations. When boiler loads are decreased, the firing rate decreases faster than steam flow which results in a decrease in tube leg temperature relative to the header's bulk temperature. When the boiler loads are increased the opposite occurs, as the steam flow increases and the boiler is over-fired and the tube leg temperatures increase relative to the header bulk temperature. Figure 2-8 below illustrates how the header bulk temperature varies relative to the mean tube leg temperature as boiler load changes. It can be deduced from this figure that the thinner tube legs are more susceptible to boiler load conditions than the thicker header material. The mismatch in temperature due to localised heating/cooling can be a source of significant thermal stress. [8]

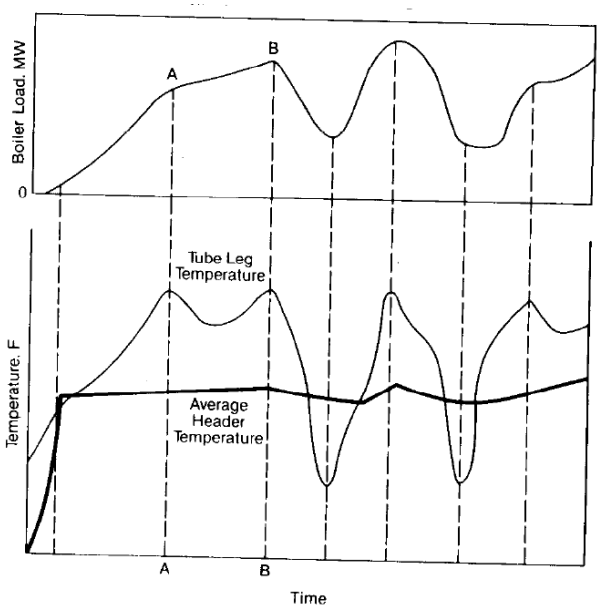

Figure 2-8: Header and tube leg temperature variation with load [8].

Kwon et al. [11] employed a thermo-mechanical FE analysis, through which they identified that the remnant life of the investigated header was greatly influenced by thermal fluctuations at quasi-steady state load conditions. The time history of steam temperature during cold start, warm and hot start was constructed using measured tube/header metal temperatures. The tube metal temperature was regarded as an equivalent to steam temperatures. From the historical data used in the study, it was shown that temperature fluctuations during quasi-steady state operations were high. The thermal stresses which arose from the high temperature fluctuations were analysed. Figure 2-9 shows the temperature distribution on the simulated header section 127 seconds after cold start. Figure 2-10 illustrates severe temperature and stress fluctuation caused by a negative thermal gradient through the header soon after steady state (full load) operations were reached. Note that the node numbers used on Figure 2-9 correlate with those on Figure 2-10.

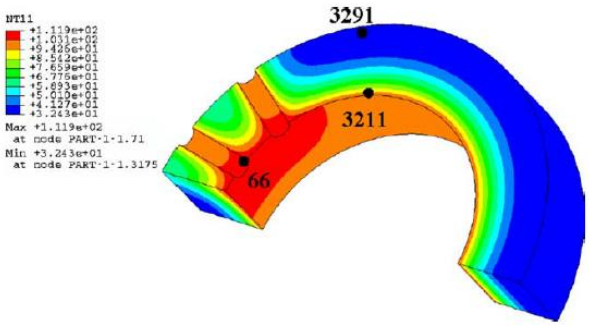

Figure 2-9: Header temperature distribution during cold start [11].

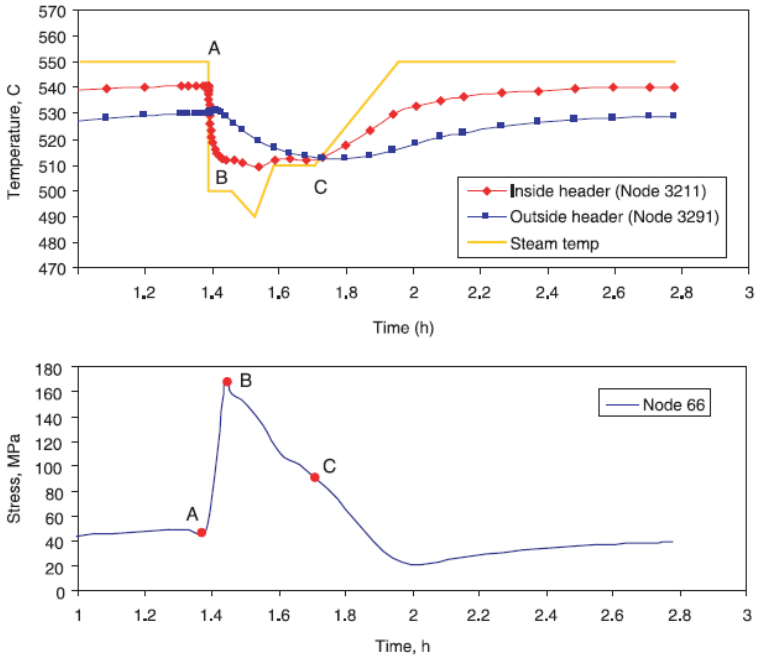

Figure 2-10: Temperature and thermal stress fluctuation during steady state conditions [11].

The study went on to state that the frequency of temperature fluctuation during transient and steady state conditions differ. It was concluded that 68 % of the total header life was depleted by crack growth due to steady state temperature fluctuations [11].

The extent of steam temperature maldistribution or deviation was investigated at a 300 MW utility boiler [12]. It was found that steam temperature maldistribution experienced in reheater and superheaters causes approximately 40% of forced outages. One of the key contributing factors for temperature maldistribution is the flow rate deviation found between the different row of tubes in superheaters and reheaters. Power plants operating at high pressure and temperatures results in increased thermal maldistribution across the heat exchanger elements. Figure 2-11 shows the extent of temperature deviation (measured and calculated) across reheater tube rows. It was stated that the reheater tubes had a maximum flow rate deviation between the rows of about 12%. It was concluded from this investigation that thermal load deviation across superheaters and reheaters can be above design calculation standards and needs to be monitored to decrease boiler tube failures.

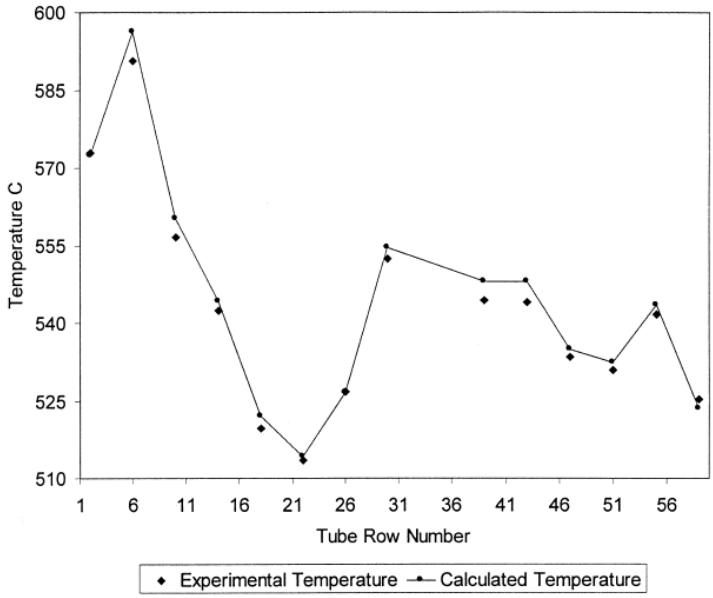

Figure 2-11: Calculated thermal load deviations across a final reheater for a 300 MW boiler [12].

A finite element study was performed on the outlet header using various load scenarios [13]. Measured plant data, including steam pressure, transient metal and steam temperature, was employed to validate the predicted thermal response of the header. The finite element model (using ABAQUS) was based on a transient heat transfer model in order to predict the coupled thermal and mechanical stress-strain response in the header section due to temperature maldistribution. Forced steam convection was modelled on the inside surfaces of the header, using transient thermal heat transfer with temperature dependent conductivity. By using the measured data, the study modelled two specific times during the transient process. From Figure 2-12, the temperature distribution can be seen for a heating transient (image on the left) and a cooling transient (image on the right). These transients mirror the transients of the realistic cycle. Significant thermal gradients were found at the stub-header intersection and between the stubs (ligament regions). A temperature difference of up to 117°C was found in a region between the pipe stubs during the heating transient. During the cooling transient a thermal gradient of approximately 75°C was predicted through the thickness of the header wall.

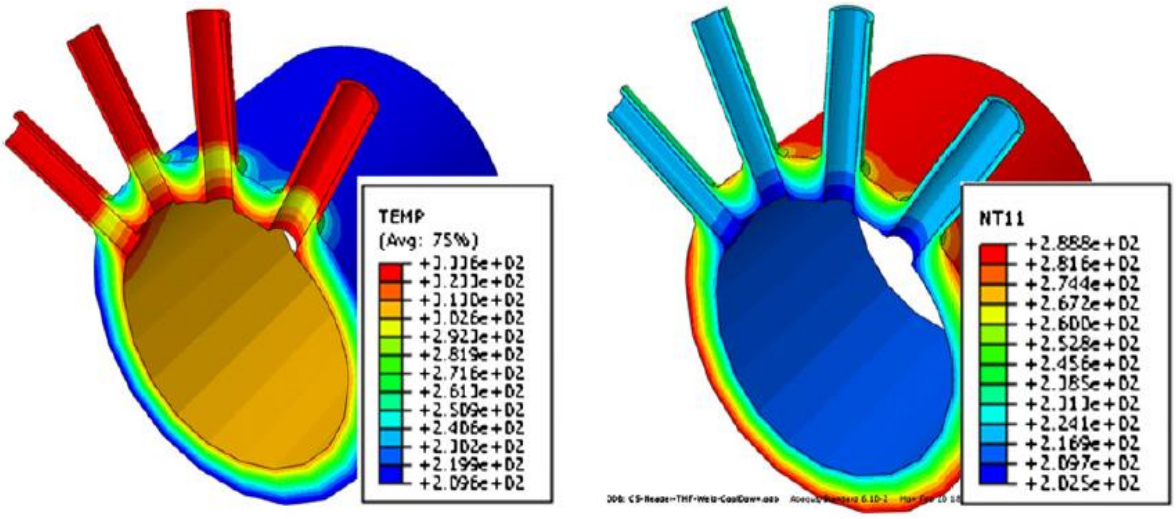

Figure 2-12: Header temperature distribution during two different transient loads [13].

Thermal stresses which resulted from the temperature distribution shown in Figure 2-12, were simulated and are illustrated in Figure 2-13 below. Significant stress concentrations were predicted at the inside surface of the stubs intersection corners for both load scenarios. Of the two transient loads, the cooling transient stresses were shown to be the most detrimental to leading crack initiation [13].

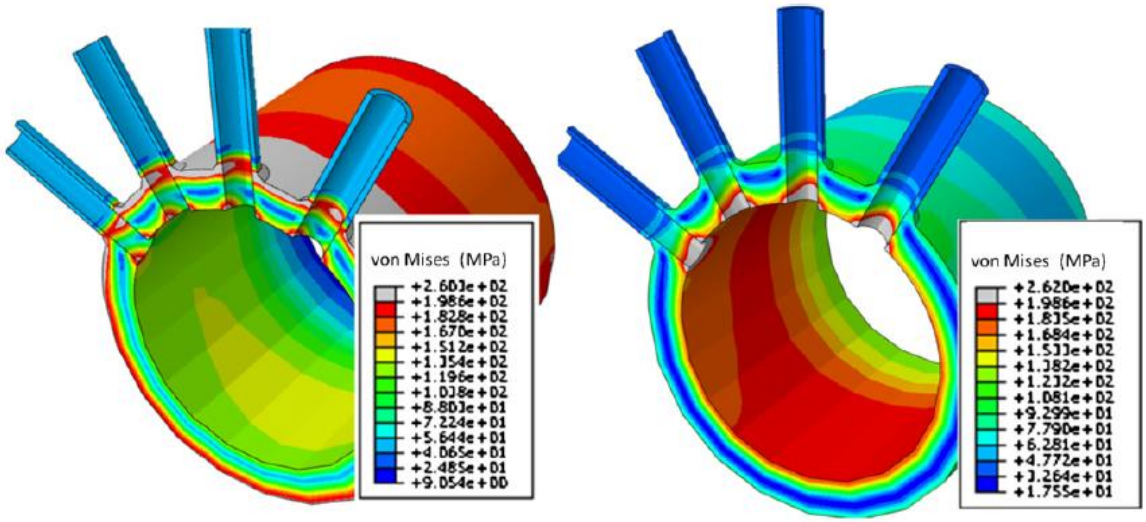

Figure 2-13: von Mises stress distribution using elastic-viscoelastic material [13].

A lifetime estimation study [14], was conducted on superheater headers. The aim of the study was to estimate the residual life of the header from initial defect size up to the maximum allowable one. The primary factor driving the lifetime was identified as the fluctuations of temperature under steady mode of operation. Steam temperature measurements during steady state operations were measured using chromel-alumel thermocouples and were registered during 54.5 hours on an analogue potentiometer. The study classified steam temperature fluctuation ranges, similarly to [13], during steady state conditions and can be seen in Table 2-1 below.

Table 2-1: The ranges of steam temperature fluctuations under steady state [14].

Class	Temperature range, ΔT,°C	Number of temperature fluctuations, per day	Maximum stress σ_{yy}, MPa	Stress range σ_{yy}, MPa
0	$\Delta T < 10$	151	to 58.4	19.0
1	$10 < \Delta T < 30$	87	to 96.3	56.9
2	$\Delta T > 30$	1	to 127	87.5

The temperature distribution field throughout the simulated header section can be seen in Figure 2-14 below. The normal stress distribution caused by a combination of an applied internal pressure of 14MPa and the temperature fluctuation can be seen in Figure 2-15. The average calculated magnitude of temperature fluctuation for Class 1 was 15°C and 46.2°C for Class 2. The study concluded that steady state loading cycles due to thermal fluctuations greatly contributed to the growth of a crack. Class 1 and 2 load cycles, as described in Table 2-1, were identified as the most influential factor on the growth of cracks on superheater headers.

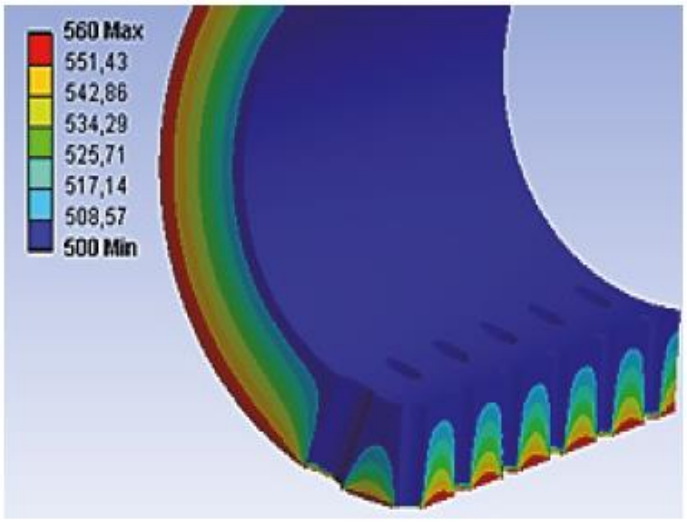

Figure 2-14: Temperature distribution field of superheater header [14].

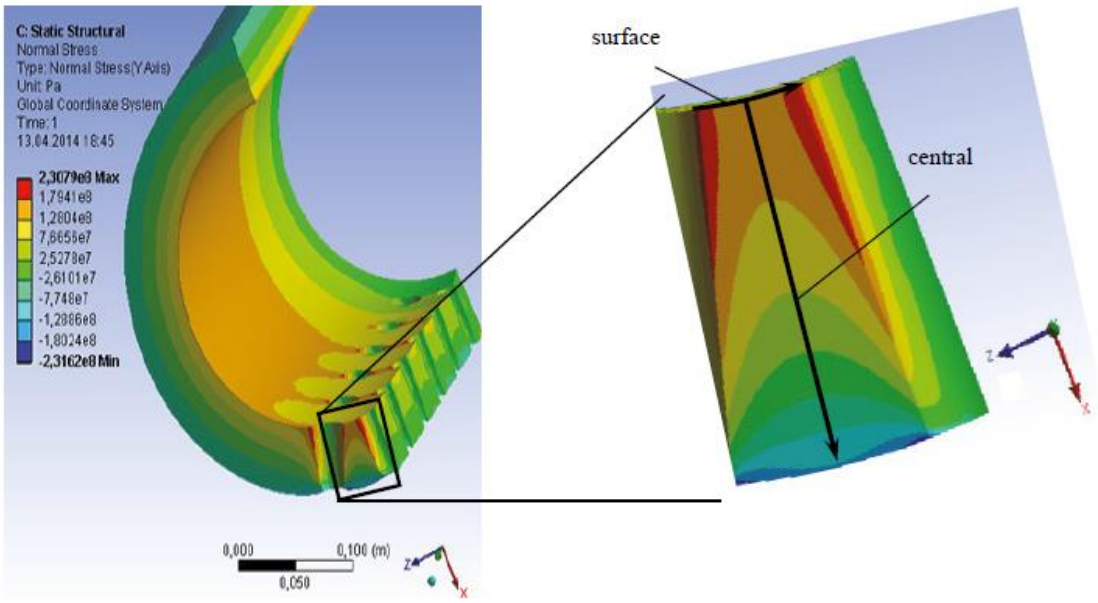

Figure 2-15: Normal stress distribution during both internal pressure and temperature fluctuations [14].

Okrajni [15] employed a thermo-mechanical fatigue analysis, through which it was found that stresses and strains caused by the influence of a non-uniform temperature field may be significantly higher than those caused by internal pressure. High tensile thermal stresses were found on a superheater header under unsteady operation in a power plant. The analysis used a FEM model prepared in Algor in order to calculate temperature, stresses and strain fields for different load conditions. Internal heat transfer coefficients, based on supporting literature, were assumed and applied to the inner surface of the header. High temperature gradients were found in the areas near the holes in the inside surface of the header during cooling period operations. The high thermal stresses found at the boreholes provide favourable circumstances for crack initiation and growth.

2.3 Flow maldistribution in headers

Gross flow maldistribution in an experimental electric heater was compared to that of similar shaped heat exchangers [16]. The comparison was made with a counter-flow heat exchanger, a condenser and a crossflow heat exchanger. It was found that the effect of fluid distribution in a condenser and a counter-flow heat exchanger is not of great importance; however fluid maldistribution in an unmixed crossflow heat exchanger can cause a loss of effectiveness of more than 25%.

A CFD simulation for steam distribution in a header and tube assemblies was done to investigate the effect of geometry on pressure drop and flow distribution [17]. The effects which influence the steam distribution, and which were investigated in this study were the tube pitch, inner header diameter, inner tubes/stubs diameter, inlet pipe diameter and the number of tubes connected to the header. It was stated that maldistribution is sufficient to produce thermal induced failures such

as excessive thermal stresses. For the CFD, both Fluent and Openfoam were used to solve turbulent flow models under steady state conditions. The study used a large range of inlet steam velocities (0.545-1.25 m/s) and pressures (up to 6MPa).

2.3.1 Effect of stub pitch

Whenever the inlet or outlet pipes are in line with the connected stubs, highly non-uniform flow distributions occur in the header. Some of the fluid bypasses neighbouring stubs when a stub/tube is aligned with the inlet/outlet pipe. By decreasing the pitch ratio (ratio of pitch between tubes at the centre to that of the pitch between any neighbouring tubes away from the inlet and outlet pipe), a higher-pressure recovery for the tubes/stubs close to the inlet or outlet pipe is found. Decreasing the pitch ratio also results in a higher steam mass flow (velocity magnitude) through the tubes. When the pitch ratio is increased however, the flow maldistribution increases as frictional pressure increases. Figure 2-16 illustrates how variation in pitch influences the mass flow distribution, where number 1 on the graph is the distribution when a stub is perfectly aligned with the inlet branch and numbers 3 & 7 are when the stubs are not aligned with the inlet branch [17].

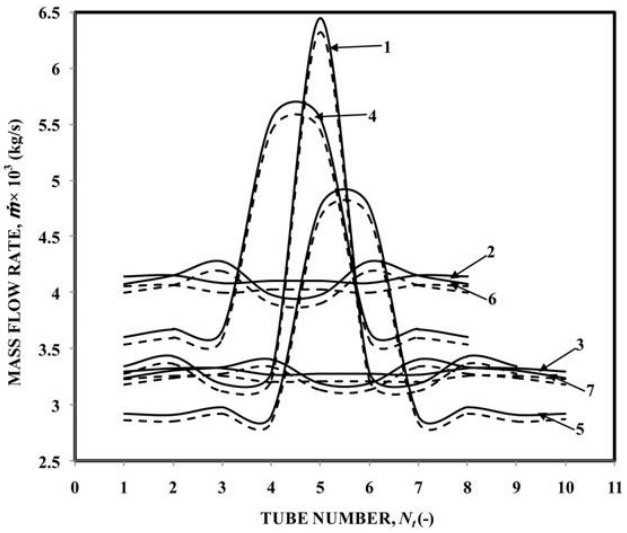

Figure 2-16: Mass Flow Distribution due to pitch variation [17].

2.3.2 Effect of inner header diameter

If the inside diameter of the header is decreased (from 100 to 50mm) it will result in a recirculation near the inlet pipes; this causes an increase in pressure drop. The larger the inside diameter of the header, the higher the momentum recovery effect as compared to friction losses [17].

2.3.3 Effect of inner tube/stub diameter

Increasing the tube diameter from 25mm to 32 mm (with header diameter and tube pitch constant), results in higher mass flow but also in higher non-uniformity of flow distribution in the header. In the case when the diameter is reduced from 25mm to 15mm, it results in more uniform flow distribution [17].

2.3.4 Effect of number of tubes

The number of tubes was increased over a wide range. In one case the tubes were increased from 9 to 27 tubes. The increase in tubes resulted in some tubes being in alignment with the inlet and outlet pipes. The inline tubes received significantly more mass flow than that of the neighbouring tubes. An increase in the number of tubes results in a decrease in fluid flow resistance and results in a high non-uniform flow distribution. The increase in total number of tubes needs to go hand in hand with the sizing of the tube inside diameter. A more uniform flow distribution is achieved if both the tube numbers are increased and the tube diameters are decreased (25mm to 5 mm) [17].

2.3.5 Effect of inlet steam mass flow

As the inlet steam mass flow rate was increased from 0.033 kg/s to 0.075 kg/s, the ENU % (Extent of Non-Uniformity) increased over the tubes/stubs. An increase in Reynolds number results in higher flow maldistribution, because the flow becomes more turbulent [17].

2.4 Thermo-mechanical analysis on cylinders

Kandil [18] evaluated stresses commonly found in cylindrical pressure vessels due to the effects of both cyclic temperature and pressure. A forward finite difference technique was used to obtain time-dependant stress distributions within the cylinder. The study investigated the effect of both the stress caused by pressure, expressed with Lame equations, and the thermal stress caused by temperature gradients. The stresses were combined and an effective stress using von-Mises theory was calculated. The influence of mean pressure and temperature as well as geometry on each of these stresses were studied and relationships were found under different working conditions.

Nabavi and Shahani [19] analytically solved a quasi-static transient thermo-elastic problem by using a finite Hankel transform. Two different thermal boundary condition cases were considered on the inner surface of a hollow cylinder: namely an exponentially decaying applied temperature and a constant prescribed temperature. Together with temperature loading, mechanical loading was also applied to the cylinder. It was found that the hoop and radial stress distribution as well as

temperature distribution through the thickness were in accordance with their cited references in literature.

Al-Zaharnah [20] conducted his thesis on thermal stresses in pipes under different flow conditions. The effects of the Reynolds number and geometry on the thermal stress was specifically studied. Pressure differences and oscillating frequency were used in the case of pulsating flow to find their influence on thermal stress.

2.5 CFD/FEA coupling for thermo-mechanical analysis

There are three general approaches that can be used for CFD solutions for fluid/solid heat transfer calculations. The approaches are listed below:

i) Conjugate heat transfer analysis.
ii) Non-coupled or one way coupled FEA/CFD procedure.
iii) Coupled FEA/CFD procedure.

For the conjugate heat transfer analysis, the fluid and solid parts are solved simultaneously using the same CFD solver. The CFD simulation solves both the internal convection and the conduction heat transfer solutions. By establishing the boundary conditions for the fluid, the model will thus produce the solids temperature profile. This process, unlike the other approaches which will be mentioned, is generally more efficient when compared to iterative coupling. The conjugate solution is better suited for steady flow conditions, as unsteady flow will result in huge (undesirable) time scale depravity between fluid convection and solid conduction. [21]

The non-coupled or one-way coupled FEA/CFD method is based on CFD simulations made in key operating points. This procedure can alleviate CFD solving cost, where only a selected number of steady state CFD calculations are performed and then used as thermal boundary conditions for FEA calculations. Heat transfer coefficients, at key points, are extracted from the CFD results and imported into FEA, which uses conduction heat transfer analysis to predict the metal temperatures. The non-coupled procedure can come at the expense of some accuracy [22].

The coupled FEA/CFD procedure is one in which different or separate CFD and FEA software packages are used for the fluid and solid regions, respectively, and thermal information exchanged between these two packages to ensure continuity of temperature and heat flux [23]. This method must employ some other developed code which smoothly exchanges relevant information from the CFD to the FEA and vice versa. A coupled FEA/CFD analysis [24], used communication library software to transfer data from their in-house finite element code to the commercial computational fluid dynamics code. Of all three the approaches mentioned, this method is the fastest in terms of running time and can produce reliable results. However, an expensive (time and money wise) exercise has to be performed to create a reliable communication code.

3. Theoretical background

3.1 Thermo-mechanical approach

The prediction of any thermal environment can be made through simple correlations/equations derived though experimental data or by using Computational Fluid Dynamics [22]. Common methods of predicting heat transfer coefficients are described in section 3.1.1 below.

3.1.1 Simple correlation method

The header studies listed in the Literature Review (section 2.2), make use of simple correlations derived from experimental data in order to perform the thermo-mechanical analysis. The correlations are for internal forced convection in tubes.

i) The fatigue thermo-mechanical header analysis [13], calculated the steam side forced heat transfer coefficients, using the equations as shown below:

$$Nu = 0.0214(Re^{0.8} - 100).Pr^{0.4} \qquad (3\text{-}1)$$

In the empirical equation above, Nu is the Nusselt number, defined in terms of Reynolds number, Re and the Prandtl number, Pr. This empirical correlation is suggested to provide better results for turbulent flow in smooth tubes [25]. Another common and accurate equation for smooth tubes, is the Dittus-Boelter equation:

$$Nu = 0.023(Re^{0.8}).Pr^{n} \qquad (3\text{-}2)$$

where $n = 0.3$ for cooling and $n = 0.4$ for heating. Equations *(3-1)* and *(3-2)* are only applicable for turbulent flow, when $Re \geq 10000$.

After determining the Nusselt number, one can proceed to calculate the forced convection heat transfer coefficient from the following equation.

$$h_i = \frac{Nu.k}{d} \qquad (3\text{-}3)$$

In the equation above, h_i is the steam-side forced convection coefficient, k is the thermal conductivity (temperature dependant) and d is the inside diameter of the header or tube.

ii) The thermo-mechanical FE analysis [11], applied heat transfer coefficients to both the tube bore hole and header inside surfaces. The steam side forced convection heat transfer coefficients were calculated using standard steam to metal correlations for single phase steam. The correlations were supplied from the Babcock and Wilcox Steam book [26]. The heat transfer coefficient equation is listed below:

$$h_1 = h_1' F_{pp} F_T \qquad (3\text{-}4)$$

From equation *(3-4)*, h_1 is the steam side heat transfer coefficient, h_1' is the basic convection velocity and geometry factor for longitudinal flow, F_{pp} is the physical property factor which combines all the properties of the fluid into one term and F_T which is the temperature factor. Each one of these terms can be read from graphs in the Steam book or can be derived from equations *(3-5)* to *(3-7)*, which are only applicable for English units.

$$h_1' = 0.023 G^{0.8} / D_i^{0.2} \qquad (3\text{-}5)$$

From equation *(3-5)*, G is the mass flux of the steam inside the tubes and D_i is the inside diameter of the tubes or header.

$$F_{pp} = c_p^{0.4} k^{0.6} / \mu^{0.4} \qquad (3\text{-}6)$$

In equation *(3-6)*, c_p is the specific heat capacity, k is the thermal conductivity of the tube or header and μ is the dynamic viscosity. All these parameters are dependent on the steam's temperature and pressure.

$$F_T = \left(\frac{T_b}{T_f}\right)^{0.8} \qquad (3\text{-}7)$$

In equation *(3-7)*, T_b is the bulk fluid temperature and T_f is the film temperature. The bulk fluid and film temperature are in Kelvin.

For both the studies reported in [11] and [13], heat transfer coefficients were calculated for the header and the tube borehole separately. The associated heat transfer coefficients were applied to

the entire inner surface of the header and the stubs. Thus, these studies assume that no real temperature or flow maldistribution occurs across the header's length. These analyses focus on the temperature difference between the stubs and the header only. The assumption that there is no temperature maldistribution across the header's length must be made in order to justify using simple empirical correlations for complex 3D geometry like that of the header. Table 3-1 shows three heat transfer coefficient values used in two sources listed in the literature review.

Table 3-1: Heat Transfer Coefficient Estimation Comparison.

Heat Transfer Coefficients [W/m^{2}K)	Area	Method	Literature source
4786	Stubs	Calculated	[13]
3611	Header (thick walled pipe)	Calculated	[13]
3663	Header (thick walled pipe)	Calculated	[10]

3.2 Convection heat transfer

Convective heat transfer is the transfer of energy between a fluid and the adjacent solid. The fluid motion can either be caused by buoyancy forces (free convection) or the fluid motion can be forced over or within a structure (forced convection). The faster the fluid motion, the greater the rate of heat transfer between the fluid and the solid. Convection heat transfer is complicated but can conveniently be expressed by Newton's law of cooling, shown below [27] :

$$\dot{Q}_{conv} = hA_s(T_s - T_\infty) \qquad (3\text{-}8)$$

where A_s is the surface area exposed to the fluid, h is the heat transfer coefficient or film coefficient, T_s is the surface temperature and T_∞ is the fluid temperature sufficiently far from the surface. The local film coefficient can thus be expressed as follows:

$$h = \frac{\dot{q}}{(T_s - T_m)} \qquad (3\text{-}9)$$

where $\dot{q}$ is the surface heat flux and T_s and T_m are the surface and mean fluid temperature at that specific location. One of the most important variables is that of the mean fluid temperature (T_b in equation *(3-7)*, T_∞ in equation *(3-8)* and T_m in equation *(3-9)*), which is also known as the reference temperature. For CFD simulations, the inlet and outlet temperatures must be specified together with the relevant heat transfer coefficients and/or heat flux values, depending on the heat transfer with the surroundings. For adiabatic conditions, the heat flux on the outside surface of a component is assumed to be zero and results in the outside surface being at the same temperature as that of the internal surface. Thus, for adiabatic conditions the rate of heat transfer is zero through the solid wall.

3.2.1 Pressure drop

When analysing flow in tubes and headers, pressure drop across the component becomes a quantity of interest. A convenient expression for pressure drop for all types of internal flow is [27]:

$$\Delta P = f \frac{L}{D} \frac{\rho V_m^2}{2} \qquad (3\text{-}10)$$

where f is the Darcy friction factor, ρ is the fluid density, V_m is the average fluid velocity, L is the length of the tube and D is the inside diameter of the tube. For turbulent flows, the Colebrook equation can be used to find the friction factor:

$$\frac{1}{\sqrt{f}} = -2\log\left(\frac{\varepsilon/D}{3.7} + \frac{2.51}{Re\sqrt{f}}\right) \qquad (3\text{-}11)$$

where ε is the equivalent roughness value for a specific material of commercial pipe. Equation *(3-9)* requires an equation solver or iterative scheme to determine the factor. The friction factor can also be read from the Moody chart, using the corresponding Reynolds number and relative roughness ($\frac{\varepsilon}{D}$) value. In order to avoid reading errors from the Moody chart, it is recommended to rather use the given implicit equation.

3.3 Conduction heat transfer

Conduction heat transfer occurs when energy is transferred from a more energetic particle to an adjacent and less energetic particle. The energy is transferred through collisions, diffusion and/or vibrations, depending on whether the substance is a liquid, gas or solid. Conduction is driven by a temperature gradient within the substance. There are also other factors which can influence the rate of heat conduction such as the material of the substance/medium and its thickness. The ability

of any medium to transfer heat via conduction is called the medium's thermal conductivity. The higher the thermal conductivity, the higher the rate of conduction will be in this specific medium.

Heat conduction differential equations, as all differential equations, depend on the coordinate system used in the application. The coordinate systems are rectangular (Cartesian), cylindrical and spherical [27].

Consider a plate or slab which represents a small rectangular element. This rectangular element has a width Δy, length Δx and height Δz. The rate of heat conduction at x, y and z are represented by $\dot{Q}_x$, $\dot{Q}_y$ and $\dot{Q}_z$ respectively. The rate of heat conduction is expressed in the differential form by Fourier's law of heat conduction. The differential equation below is for one dimensional heat conduction in the x-direction [27].

$$\dot{Q}_{conduction} = -kA\frac{\partial T}{\partial x} \tag{3-12}$$

where k is the thermal conductivity of the medium and A is the surface area of the medium. An example of surface area is $A = \Delta x \Delta z$.

The rate of heat conduction at x+Δx, y+ Δy and z+zΔ are $\dot{Q}_{x+\Delta x}$, $\dot{Q}_{y+\Delta y}$ and $\dot{Q}_{z+\Delta z}$ respectively. These rates are equal to the original rate plus the change across the control volume. The rates can therefore be expressed as follows.

$$\dot{Q}x + \Delta x = \dot{Q}x + \frac{\partial \dot{Q}x}{\partial x}dx \tag{3-13}$$

$$\dot{Q}y + \Delta y = \dot{Q}y + \frac{\partial \dot{Q}y}{\partial y}dy \tag{3-14}$$

$$\dot{Q}z + \Delta z = \dot{Q}z + \frac{\partial \dot{Q}z}{\partial z}dz \tag{3-15}$$

The rate of heat generation inside the rectangular element can be expressed as:

$$\dot{Q}_{element} = \dot{q}V_{element} = \dot{q}\Delta x\Delta y\Delta z \tag{3-16}$$

where $\dot{q}$ is the rate of heat generation in a medium and is specified per unit volume and $V_{element}$ is the volume of the element.

The rate of change of the energy content of the element can be expressed as:

$$\frac{\Delta E_{element}}{\Delta t} = \frac{\rho C V_{element}(T_{t+\Delta t} - T_t)}{\Delta t} \qquad (3\text{-}17)$$

where ρ is the density of the medium and C the specific heat of the medium.

The energy balance equation across the differential control volume, combines Equations *(3-13)*-*(3-17)* to form:

$$\dot{Q}_x + \dot{Q}_y + \dot{Q}_z - \left(\dot{Q}_{x+\Delta x} + \dot{Q}_{y+\Delta y} + \dot{Q}_{z+\Delta z}\right) + \dot{q}\Delta x\Delta y\Delta z = \frac{pCV_{element}(T_{t+\Delta t} - T_t)}{\Delta t} \qquad (3\text{-}18)$$

Substituting the rates of heat transfer in equation *(3-18)* with equation *(3-12)* and then dividing both ends by the volume, $V_{element} = \Delta x\Delta y\Delta z$ results in:

$$\frac{\partial}{\partial x}\left(k\frac{\partial T}{\partial x}\right) + \frac{\partial}{\partial y}\left(k\frac{\partial T}{\partial y}\right) + \frac{\partial}{\partial z}\left(k\frac{\partial T}{\partial z}\right) + \dot{q} = \frac{pC\partial T}{\partial t} \qquad (3\text{-}19)$$

Equation *(3-19)* is the general heat conduction equation for the rectangular coordinate system.

By using coordinate transformation through relations between the rectangular and cylindrical coordinates of a point, we can derive the general heat conduction equation for the cylindrical coordinate system. The relations between the two coordinate systems are as follows:

$$x = r\cos(\emptyset) \quad y = rsin(\emptyset) \quad z = z$$

Substituting the relations into equation *(3-19)* we obtain equation *(3-20)* for the cylindrical coordinate system:

$$\frac{1}{r}\frac{\partial}{\partial r}\left(kr\frac{\partial T}{\partial r}\right) + \frac{1}{r^2}\frac{\partial}{\partial \emptyset}\left(kr\frac{\partial T}{\partial \emptyset}\right) + \frac{\partial}{\partial z}\left(k\frac{\partial T}{\partial z}\right) + \dot{q} = \frac{pC\partial T}{\partial t} \qquad (3\text{-}20)$$

By assuming one dimensional steady state conditions ($\frac{\partial}{\partial t} = 0$) with no heat generation ($\dot{q} = 0$), Equation *(3-20)* can be greatly simplified to:

$$\frac{1}{r}\frac{\partial}{\partial r}\left(r\frac{\partial T}{\partial r}\right) = 0 \qquad (3\text{-}21)$$

Based on Equation *(3-12)*, the general solution, at any radius, to the above equation is given by:

$$\dot{Q}_{conduction} = -k(2\pi rL)(\frac{dT}{dr}) \quad (3\text{-}22)$$

By using boundary conditions for the cylinder, we can derive a better solution for the equation above. The boundary conditions are stated below:

Inner wall temperature, where $r = r_1$: $T = T_1$
Outer wall temperature, where $r = r_2$: $T = T_2$

Solving Equation *(3-22)* for the given boundary conditions, gives the heat transfer per unit length of a cylinder as [27]:

$$\dot{Q}_{conduction} = -k(2\pi rL)(\frac{T_1 - T_2}{\ln(\frac{r_2}{r_1})}) \quad (3\text{-}23)$$

3.4 Stress categories

According to ASME Section VIII div 2 [28], there are three categories of stress, namely:

Primary stress:

Primary stresses can best be characterised by being describing as not self-limiting. Not self-limiting implies that the stress is generated by unrelenting loads which remain constant after the stresses in a pipe cross section go beyond the yielding point (reference). If primary stresses exceed yield strength by considerable margins, then it will result in a failure or at least gross distortion. Primary stresses are usually classified into two categories, namely general and local [29]. General membrane primary stresses are caused when circular cylinders or headers are exposed to internal pressure. The general primary stresses can be further divided into circumferential hoop stress and radial stresses (due to internal pressure).

Secondary stress:

Secondary stresses develop due to constraints of adjacent parts or by self-constraint of a structure. Unlike primary stresses, secondary stresses are self-limiting. When secondary stresses exceed yielding and the material goes into the plastic region, relaxation will occur and the load will start to disappear. Local yielding and minor distortion can be expected from secondary stresses. One of the best examples of secondary stresses is thermal stress.

Peak Stress:

Peak stresses are associated with local discontinuities, local thermal stress and/or any stress concentration. It does not cause noticeable distortion and is objectionable only as a possible source of fatigue crack or brittle fracture.

3.4.1 Combined header stress and strains

In the literature review section, it was shown that headers operating at high temperatures usually fail due to a combination of high sustained internal pressure, local thermal stresses and cyclic loading. For this project we will only be focusing on steady-state conditions. It should be noted that steady state conditions are not truly steady, and headers may experience high cycle fatigue in these conditions. However, a previous study [30] has shown that fatigue damage can be neglected if one assumes purely steady state conditions.

The British-European pressure part codes list the steels used for steam station pipes and headers and at which temperatures these steels will be subject to creep damage. By neglecting fatigue, we can assume that the strains (and their associated stresses) on the superheater headers during steady state creep behaviour are composed of three parts [31]:

$$\varepsilon_{total} = \varepsilon_{elastic} + \varepsilon_{thermal} + \varepsilon_{creep} \quad (3\text{-}24)$$

Since this dissertation is focused on determining the impact of thermal maldistribution and thus thermal stresses, creep will be excluded. This leaves the total strain as follows:

$$\varepsilon_{total} = \varepsilon_{elastic} + \varepsilon_{thermal} \quad (3\text{-}25)$$

Elastic strain (due to primary stress) is obtained from the standard Hooke's law and thermal strain (due to secondary stress) from Fourier's law of thermal conductivity.

Additional pressure code specific design checks [32] should be performed to test whether the header's plastic strain is within acceptable limits. If significant plastic strain is present then it should also be taken into account.

3.5 Elastic stress & strain

Cylindrical pressure vessels, such as headers, develop tangential (hoop), radial and axial stresses due to internal pressure caused by superheated steam. The hoop and radial stresses are functions of the vessel's radius and change in magnitude though the vessel's wall. The axial stress for a closed ended thick walled cylinder (header) is independent of the cylinders radius. We can say that the headers are thick walled cylinders as their wall thicknesses are more than one tenth that of the outside radius. The minimum header ratio of wall thickness to outside radius is 0.35, which is larger than 0.1 and thus they can be considered thick walled cylinders [33].

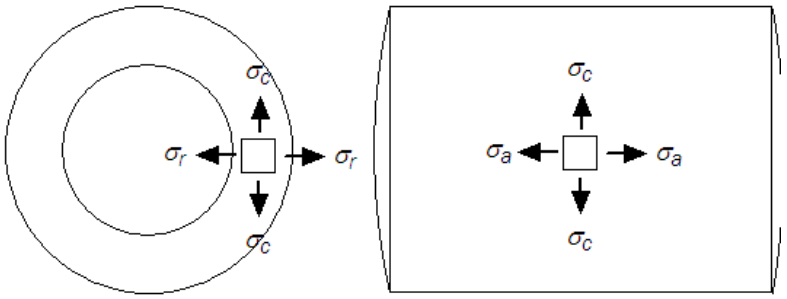

Figure 3-1: Circumferential, axial and radial stress on a cylinder [34].

The Lame equations for radial, hoop (circumferential) and axial stresses for thick walled components are as follows [33]:

$$\sigma_r(r) = \frac{r_i^2 P_i - r_0^2 P_o}{r_o^2 - r_i^2} - \frac{(P_i - P_o)(r_0^2 . r_i^2)}{r^2(r_o^2 - r_i^2)} \quad (3\text{-}26)$$

$$\sigma_\theta(r) = \frac{r_i^2 P_i - r_o^2 P_o}{r_0^2 - r_i^2} + \frac{(P_i - P_o)(r_o^2 . r_i^2)}{r^2(r_o^2 - r_i^2)} \quad (3\text{-}27)$$

$$\sigma_Z = \frac{r_i^2 P_i - r_o^2 P_o}{r_o^2 - r_i^2} \quad (3\text{-}28)$$

The axial/longitudinal stress is only applicable if both ends of the cylinder are closed and prevent displacement in that direction. If the cylinder's ends are open then it can move freely and no stresses will be induced on the material.

In the three equations above, P_i is the internal pressure acting on the entire inner surface of the vessel, P_o is the outer pressure, r_i is the internal radius, r_o is the outer radius and r is the radius at the point of interest. Figure 3-2 illustrates the magnitude of stresses due to pressure on a cylinder as distributed across the radius. The stress component due to pressure can be expressed as principle stresses, with $\sigma_1 = \sigma_\theta, \sigma_2 = \sigma_r$ and $\sigma_3 = \sigma_z$. From Figure 3-2 it can be seen that the hoop or tangential stress has the highest magnitude on the inside of the cylinder and decreases as it approaches the outside surface of the cylinder.

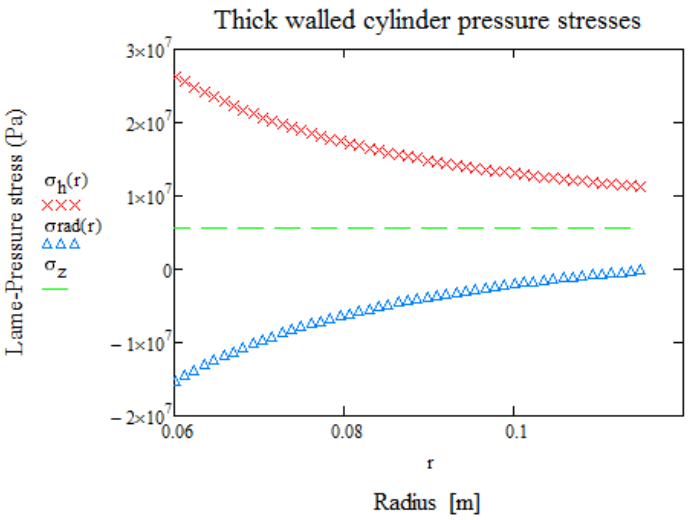

Figure 3-2: Example of a cylinder with Pi=16MPa, Po=101.32kPa, r_i = 59mm and r_o = 115mm.

The radial displacement can be expressed as follows [33]:

$$u_{elastic}(r) = \left(\frac{1-v}{E}\right)\left(\frac{r_i^2 P_i - r_0^2 P_o}{r_o^2 - r_i^2}\right)(r) + \left(\frac{1+v}{E}\right)\left(\frac{(P_i - P_0)(r_o^2 . r_i^2)}{r(r_o^2 - r_i^2)}\right) \quad (3\text{-}29)$$

From the radial displacement, the radial and tangential elastic strains are determined as follows:

$$\varepsilon_r(r) = \frac{du_{elastic}(r)}{dr} = \left(\frac{1-v}{E}\right)\left(\frac{r_i^2 P_i - r_o^2 P_0}{r_o^2 - r_i^2}\right) - \left(\frac{1+v}{E}\right)\left(\frac{(P_i - P_0)(r_o^2 . r_i^2)}{(r_o^2 - r_i^2)(r^2)}\right) \quad (3\text{-}30)$$

$$\varepsilon_\theta(r) = \frac{u_{elastic}(r)}{r} = \left(\frac{1-v}{E}\right)\left(\frac{r_i^2 P_i - r_o^2 P_o}{r_o^2 - r_i^2}\right) + \left(\frac{1+v}{E}\right)\left(\frac{(P_i - P_o)(r_o^2 . r_i^2)}{(r_o^2 - r_i^2)(r^2)}\right) \quad (3\text{-}31)$$

3.6 Thermal stress & strain

Thermal stresses are localised stresses in the header and can be greater than the stresses associated with steam pressure, dependant on the load conditions. As the loads are changed through the header's service life, these thermal stresses increase and decrease in cycles and can contribute to crack initiation. It has been found that most of these localized thermal stresses are found at the header bore hole penetration which acts as a geometric discontinuity. The stress caused by the pressure increases the adverse effects of the thermal stress [8].

A material is either internally or externally constrained. External constraints are constraints which prohibit the whole system from displacing. Internal constraints are constraints that are present

locally within a material and prevent other locations in the same material from expanding or contracting [35].

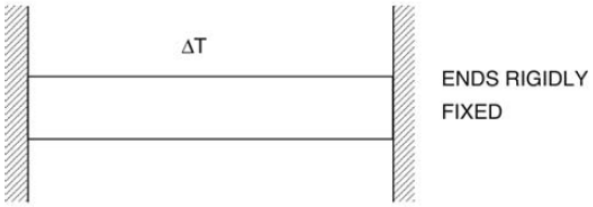

Figure 3-3: Externally constraint bar [35].

Figure 3-3 above shows a system (bar) externally constrained on either side via two walls. Due to a temperature difference present within the beam, expansion wants to occur but is prohibited by the walls. Stresses will arise within the bar and, if high enough, will cause bending and buckling until complete beam failure occurs. Using the bar, we can express the simplest equation for thermal stress as a function of material properties and temperature difference, namely:

$$\sigma = -\alpha E \Delta T \qquad (3\text{-}32)$$

From equation *(3-32*), we note that the stress is dependent on linear expansion coefficient α, Young's modulus E and the temperature difference or temperature change ΔT.

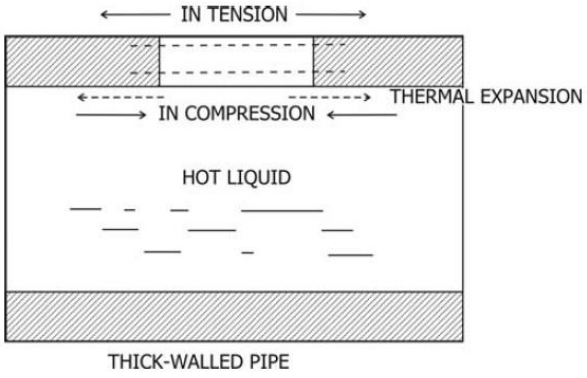

Figure 3-4: Internal constraint [35].

With high pressure pipes and headers found in boilers, internal constraints are more common. Figure 3-4 above illustrates what will happen when a thermal gradient occurs across the tube wall. The inside surface of the wall is hotter than the outside surface due to the rate of heat transfer between the tube material and the fluid inside the tube. The thermal gradient will cause the inside surface to expand but will be resisted by the colder outer layer as the two layers are not allowed to move independently. The thicker the wall, the higher the thermal gradient and the higher the stresses which will be induced into the material. This phenomenon is thus especially important for thick walled pressure parts with high steam temperatures [35]. According to [20], many attempts

were made using different techniques to avoid problems resulting from temperature differentials, such as functionally gradient materials and compound cylinders.

Thermal stress calculations can quickly become a very complex and time-consuming ordeal. By assuming a simple geometry such as a hollow cylinder at steady state heat transfer conditions, the problem is greatly simplified. See below radial, tangential and axial stresses caused by thermal gradients through the header wall [35]:

$$\sigma_{rt}(r) = \left(\frac{-\alpha E(T1 - T2)}{2(1-v)}\right)\left[\frac{\ln\left(\frac{r}{r_o}\right)}{\ln\left(\frac{r_i}{r_o}\right)} - \left(\frac{(\frac{r_o}{r})^2 - 1}{(\frac{r_o}{r_i})^2 - 1}\right)\right] \quad (3\text{-}33)$$

$$\sigma_{\theta t}(r) = \left(\frac{-\alpha E(T1 - T2)}{2(1-v)}\right)\left[\frac{1 + \ln\left(\frac{r}{r_o}\right)}{\ln\left(\frac{r_i}{r_o}\right)} + \left(\frac{(\frac{r_o}{r})^2 + 1}{(\frac{r_o}{r_i})^2 - 1}\right)\right] \quad (3\text{-}34)$$

As with the stresses caused by pressure, axial thermal stress will only occur if the cylinder's ends are closed or constrained from displacing in the axial direction (zero axial strain).

$$\sigma_{zt}(r) = \left(\frac{-\alpha E(T1 - T2)}{2(1-v)}\right)\left[\frac{1}{\ln\left(\frac{r_i}{r_o}\right)} + \frac{2\ln(\frac{r}{r_o})}{\ln\left(\frac{r_i}{r_o}\right)} + \frac{2}{(\frac{r_o}{r_i})^2 - 1}\right] \quad (3\text{-}35)$$

For the three stresses illustrated above, α is the thermal expansion, E is the Young's Modulus, *T1* is the temperature inside the cylinder, $T2$ is the temperature outside the cylinder, v is the Poison ratio, r_i inside radius and r_o is the outside radius.

By taking the geometry of the cylinder used in Figure 3-2 and giving it thermal properties shown in Table 3-2, the magnitudes of the three thermal stress components were compared with one another using a hand calculation and shown in in Figure 3-5. Both the tangential and axial stress components increase with an increase in radius.

Table 3-2: Thermal properties for example cylinder

Property description	Value	Units
Young's Modulus	165	GPa
Poisson's ratio	0.33	-
Thermal expansion	16 x 10^{-6}	K^{-1}
Inside temperature	793	K

Property description	Value	Units
Outside temperature	773	K

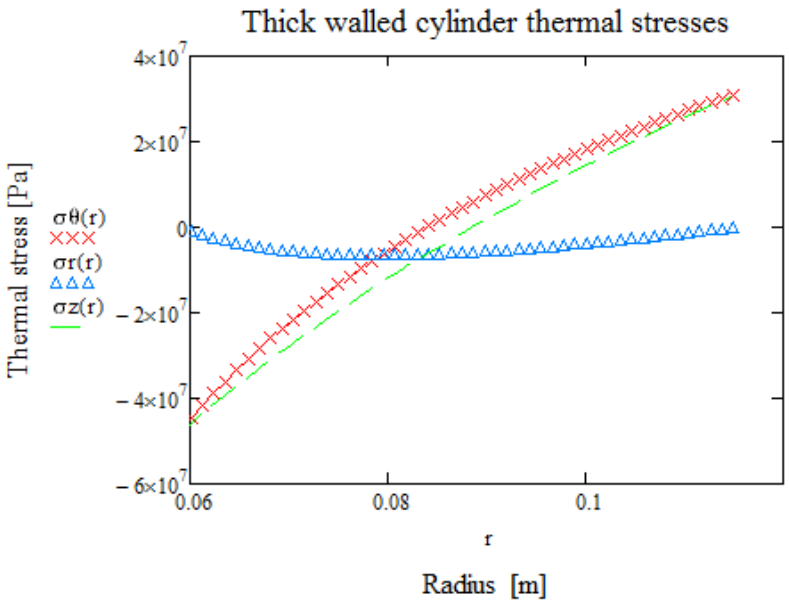

Figure 3-5: Example of Figure 3-2 cylinder under pure thermal loading.

3.7 Computational fluid dynamics

Instead of solving a continuous domain, CFD discretizes the domain into a grid. Conventionally, the flow variables are defined at every grid point in the continuous domain. For the discrete domain, the flow variables are only defined at certain grid points. The values at other grid locations are determined by interpolating between the grid points. The continuous variables from the governing partial differential equations can be approximated into discrete variables. The whole discrete system will then comprise of a set of equations in the discrete variables. Solving the large number of equations over the grid (matrix inversion problem), requires many iterations. Using CFD software with the aid of ever-increasing computational power, allows engineers to greatly decrease solving time and cost. CFD has been shown to provide accurate results when describing fluid motion and heat transfer and is more cost effective than physical testing [36].

The physics are governed by three fundamental conservation principles, namely: mass, momentum and energy, combined with the equations of state. The governing equations used in CFD are given by [37] as:

Continuity
$$\frac{\partial \rho}{\partial t} + div(\rho \overrightarrow{V}) = 0 \quad (3\text{-}36)$$

Momentum-x
$$\frac{\partial (\rho u)}{\partial t} + div(\rho u \overrightarrow{V}) = -\frac{\partial p}{\partial x} + \frac{\partial \tau_{xx}}{\partial x} + \frac{\partial \tau_{yx}}{\partial y} + \frac{\partial \tau_{zx}}{\partial z} + \rho f_x \quad (3\text{-}37)$$

Momentum-y
$$\frac{\partial (\rho v)}{\partial t} + div(\rho v \overrightarrow{V}) = -\frac{\partial p}{\partial y} + \frac{\partial \tau_{xy}}{\partial x} + \frac{\partial \tau_{yy}}{\partial y} + \frac{\partial \tau_{zy}}{\partial z} + \rho f_y \quad (3\text{-}38)$$

Momentum-z
$$\frac{\partial (\rho w)}{\partial t} + div(\rho w \overrightarrow{V}) = -\frac{\partial p}{\partial z} + \frac{\partial \tau_{xz}}{\partial x} + \frac{\partial \tau_{yz}}{\partial y} + \frac{\partial \tau_{zz}}{\partial z} + \rho f_z \quad (3\text{-}39)$$

Energy
$$\frac{\partial (\rho e)}{\partial t} + div(\rho e \overrightarrow{V}) = -p\, div(\overrightarrow{V}) + div(k grad T) + \Phi + \rho \dot{q} \quad (3\text{-}40)$$

Equations of state
$$e = e(\rho, T)\ and\ p = p(\rho, T) \quad (3\text{-}41)$$

Equation *(3-36*), known as the continuity equation, describes the conservation of mass over a local control volume (computational cell) and guarantees mass flow throughout the domain. Equations *(3-37*)-*(3-39*) describes the momentum conservation equations split into three scalar relations along the x, y and z axes. Newton's 2nd law, on which these equations are based, states that the net force on the fluid element equals its mass times the acceleration of the element. The forces acting on the fluid are mainly attributed to body forces such as gravity or magnetic forces and surfaced forces, such as pressure distribution or shear and normal forces acting on the fluid surface. Equation *(3-40*) describes the conservation of energy, which is based on the first law of thermodynamics. Equation *(3-40*) also contains the dissipation term Φ. The equation of state relates the internal energy and pressure of the fluid to the density and temperature.

3.8 Finite element analysis

Structural engineering problems contain a combination of complex geometries, loadings and material properties. Due to these complexities, analytical solutions are not always obtainable. As in the case of CFD, a numerical approach is required. FEA involves discretising the entire body into smaller units (finite elements) which are interconnected at points, commonly called nodes. Equations are formulated for each element and combined to find the solution for the whole body. The primary reason for using FEA, is to determine the stress distribution throughout the solid's body and to evaluate the displacements [38].

For a two-dimensional thermal stress problem, the following general steps are applied in FEA to solve the stresses due to temperature difference:

Step 1:

Evaluating the thermal force matrix for each of the elements. The shape of the element will change the form of the thermal force matrix equations. Assuming a constant-strain, triangular element with constant thickness we find the thermal force matric to be:

$$f_T = \begin{Bmatrix} f_{Tix} \\ f_{Tiy} \\ \vdots \\ f_{Tmy} \end{Bmatrix} = \frac{\alpha E t T}{2(1-v)} \begin{Bmatrix} \beta_i \\ \gamma_i \\ \beta_j \\ \gamma_j \\ \beta_m \\ \gamma_m \end{Bmatrix} \qquad (3\text{-}42)$$

where α is the thermal expansion, E is the Young's Modulus, t is the element thickness , T is the uniform temperature rise across the element,v is the Poison ratio, β and γ refers to the distance in the y and x direction between the element's nodes respectively, and notations i,j and m refer to different nodes on the triangular element.

The global thermal force matrix is found by direct assemblage of the element force matrices.

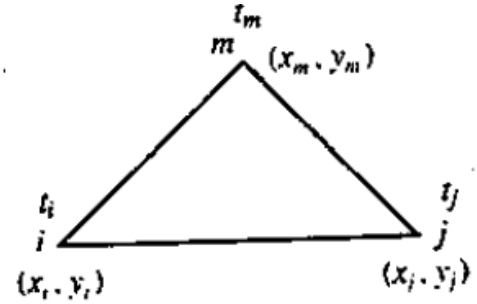

Figure 3-6: Basic triangular element [38].

Step 2:

Evaluate the stiffness matrix for each of the elements and combine them to find the global stiffness matrix.

We obtain the element stiffness matrix using:

$$[k] = tA[B]^T[D][B] \qquad (3\text{-}43)$$

where $[B]$ is a geometric (solely depends on element nodal coordinates) matrix used in the strain/displacement relationship and $[D]$ represents the modulus of elasticity in the stress/strain relationship.

Matrix $[B]$ can be expressed as follows:

$$[B] = \frac{1}{2A}\begin{bmatrix} \beta_i & 0 & \beta_j & 0 & \beta_m & 0 \\ 0 & \gamma_i & 0 & \gamma_j & 0 & \gamma_m \\ \gamma_i & \beta_i & \gamma_j & \beta_j & \gamma_m & \beta_m \end{bmatrix} \quad \textit{(3-44)}$$

where A is the surface area of the element.

The matrix representing the modulus of elasticity and Poisson ration can be expressed as follows:

$$[D] = \frac{E}{(1-v^2)}\begin{bmatrix} 1 & v & 0 \\ v & 1 & 0 \\ 0 & 0 & \frac{1-v}{2} \end{bmatrix} \quad \textit{(3-45)}$$

The global stiffness matrix, $[K]$,is then found by assembling all the element stiffness matrices.

Step 3:

Assuming that only thermal loading is considered, the global force matrix can be expressed in terms of the global stiffness matrix and nodal displacements, as seen from the equation below:

$$[f_T] = \text{[K].\{d\}} \quad \textit{(3-46)}$$

Since both the global force and stiffness matrices have been solved, the nodal displacement vector can be solved.

Step 4:

After solving the nodal displacements, one can now proceed to obtain the thermal stresses in each of the triangular elements, using the following equation:

$$\{\sigma\} = [D][B]\{d\} - [D]\{\varepsilon_T\} \quad \textit{(3-47)}$$

where ε_T is the strain due to the temperature increase over the element. The thermal strain, as referred in Equation *(3-32)*, is most commonly expressed as:

$$\{\varepsilon_T\} = \{\alpha \Delta T\} \quad \textit{(3-48)}$$

As in Equation *(3-32)*, α is the linear expansion coefficient and ΔT is the temperature change.

4. Thermocouple installation

4.1 Location and quantity of thermocouples

Thermocouples were installed at key locations on the final superheater headers, during a maintenance outage. The superheater headers include the inlet and outlet stubbox headers, as well as the manifold headers. See Figure 1-2 and Figure 1-3 for the location of the headers. Numerous site visits and measurements were completed together with the contractor responsible for the supply and installation of the K-type thermocouples. The site measurements were conducted prior to the outage. The site visits were essential for establishing the required thermocouple lengths in the penthouse and determining a safe location for the data logger cage. The final thermocouple lengths were determined using a combination of site measurements and drawings of the penthouse and location of the superheater headers. The K-type thermocouples were used due to their large temperature range for which the thermocouples sensitivity (Seebeck coefficient) remains fairly constant [39]. The proposed locations of the thermocouples were presented to the utility management on several occasions and the final locations were decided on in order to capture both a detailed and global view of the metal temperature distribution across the headers. The thermocouples were installed on the outside metal surfaces of the header and stubs and were attached using Inconel wires. See Table 4-1 below for the location and quantity of the thermocouple installed during the maintenance outage.

Table 4-1: Thermocouple location and quantities.

Area	**Location**	**Quantity**
Inlet stubbox- element 3,10,17 & 23	Inlet branches	4 (one for each element)
Outlet stubbox- element 23	Header	2
	Stubs	34
	Outlet branches	2
Outlet manifold header 1	Header	1
	Tubes	14
Outlet manifold header 2	Header	1

Area	Location	Quantity
	Tubes	14
Total Thermocouples		72

Four thermocouples were installed on the inlet pipes of the inlet stubbox headers (see Figure 4-1) and were divided so that one inlet header from each of the four legs was captured. Thermocouples were installed on the inlet pipes of these headers to compare the temperature distributions across the element legs and to serve as inlet boundary conditions if the inlet header need to be modelled.

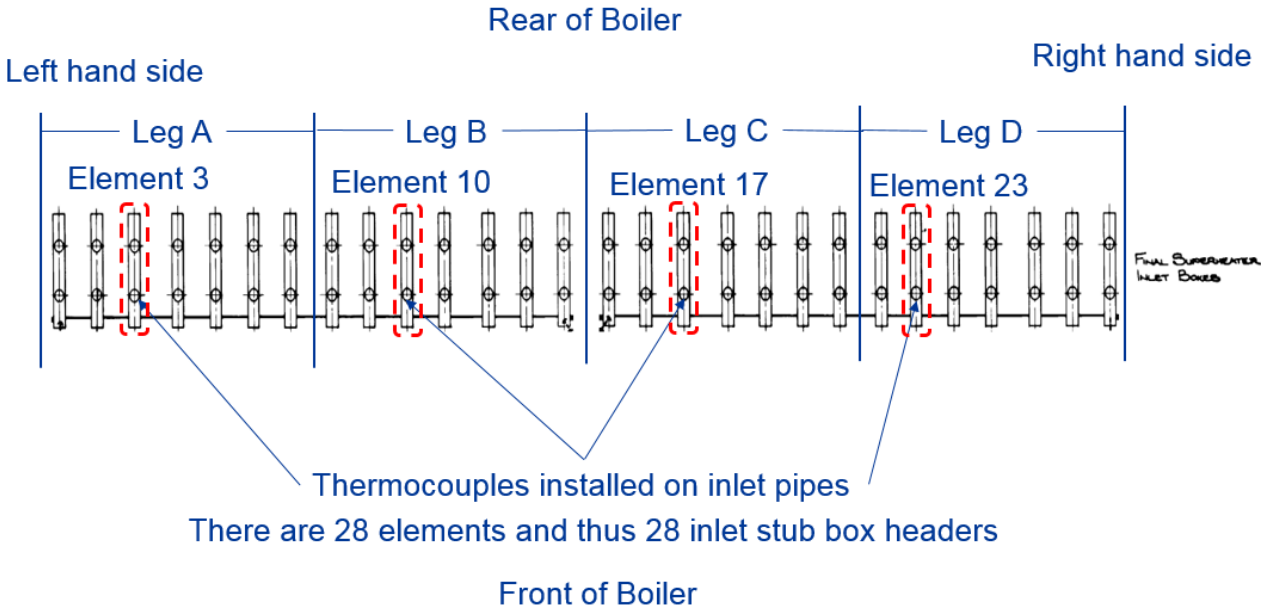

Figure 4-1: Inlet stubbox thermocouple installation.

A thermocouple, originally installed by the power plant team on one of the stubs, indicated that element 23 was on average one of the hottest elements. The outlet stubbox header for element 23 was specifically chosen because of the high temperatures and frequent failures. Before the new thermocouples were installed, there was only one thermocouple per header. See Figure 4-2 below for the location of the 36 installed thermocouples.

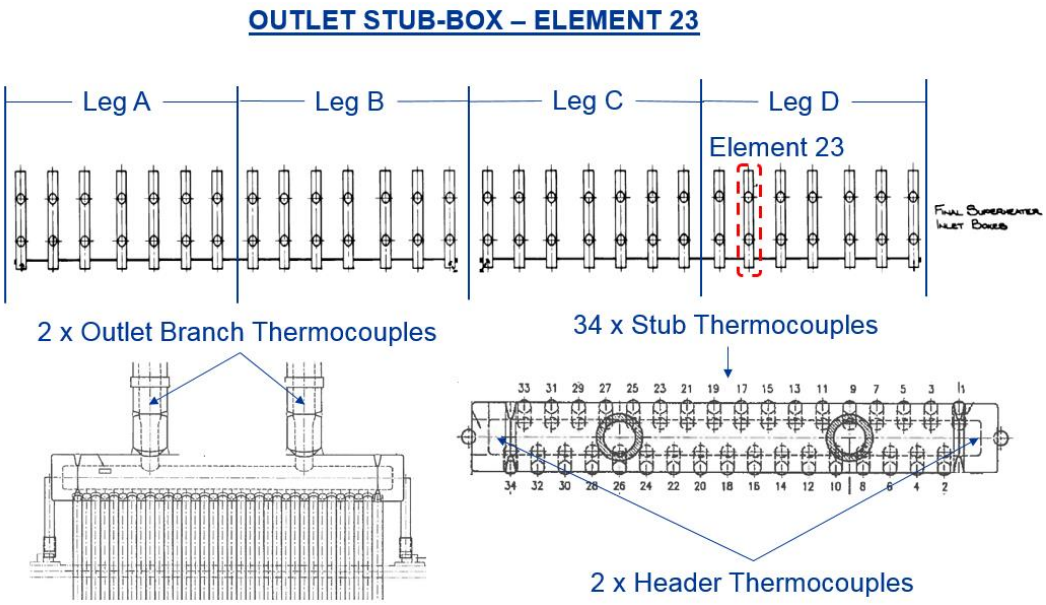

Figure 4-2: Outlet stubbox thermocouple installation.

For the two manifold headers, thermocouples were installed on every second outlet pipe (highlighted in green in Figure 4-3). The two outlet branches from the outlet stubbox header (see Figure 4-2) become outlet pipes that connect to one of the two manifold headers. There are thus two outlet pipes per element and thus by installing a thermocouple on every second outlet pipe, an outlet temperature for each of the 23 elements was measured.

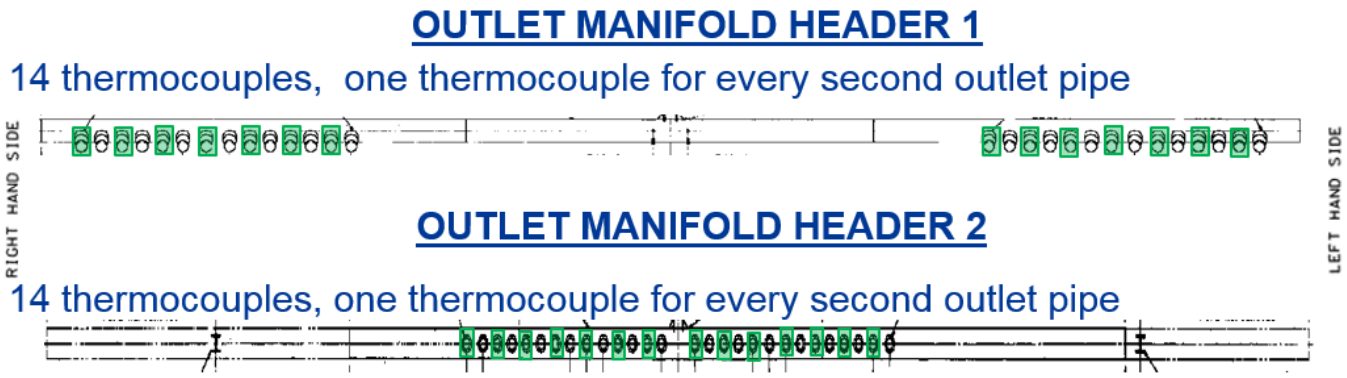

Figure 4-3: Outlet manifold header thermocouple locations.

4.2 Data logger

The DT80 Series data logger was used in conjunction with the CEM 20 Channel Expansion Module, see Figure 4-4. An expansion module was necessary as the data logger only had 5 channels, with a maximum of three common reference inputs per channel. The expansion module adds 20 universal data logging channels, but one of the 20 channels was used to connect the expansion module to the data logger. The combination essentially provided 24 channels and thus a maximum of 72 thermocouples could be connected. The data logger and expansion module were safely installed

into a secure steel cabinet, which is padlocked in order to prevent unauthorized access on site. The DT80 data logger can be set up via either an USB connection or remote Ethernet connection to the dEX configuration editor. In the dEX editor, the logger was instructed to send the measured data to specified email addresses. Each email was set up to contain data measurements for a 12-hour period, set at one-minute sampling frequency. Once the logger's internal memory reached full capacity, all the accumulated data was manually taken from the logger using an USB storage device. After all the data was gathered, the memory was wiped clean and the data capturing process was reset.

Before the installation took place, thermocouple numbers were assigned to dedicated locations on the superheater headers. Each thermocouple wire was numbered inside the penthouse and carefully routed to the logger, where it was given a corresponding number which was also placed on the wire. A voltage test was performed in order to confirm that the numbering outside the boiler matched the numbering inside the penthouse. Once it was established that the numbers matched, the wires were connected to the logger and the expansion module. A dedicated on-site power supply was arranged for the data logger.

Figure 4-4: Data logger and expansion module in the protective cabinet.

4.3 Certified calibration of thermocouples

Prior to installation, the thermocouples were calibrated and certified in accordance with the conditions of the accreditation granted by the South African National Accreditation System (SANAS). The results of the calibration are traceable to the national measuring standards. The thermocouples were calibrated by directly comparing them against a reference thermometer and the difference in

temperature was found to be slightly higher than ± 1°C. Figure 4-5 shows the temperature deviation from measured temperature readings, over a range of 0 to 575°C.

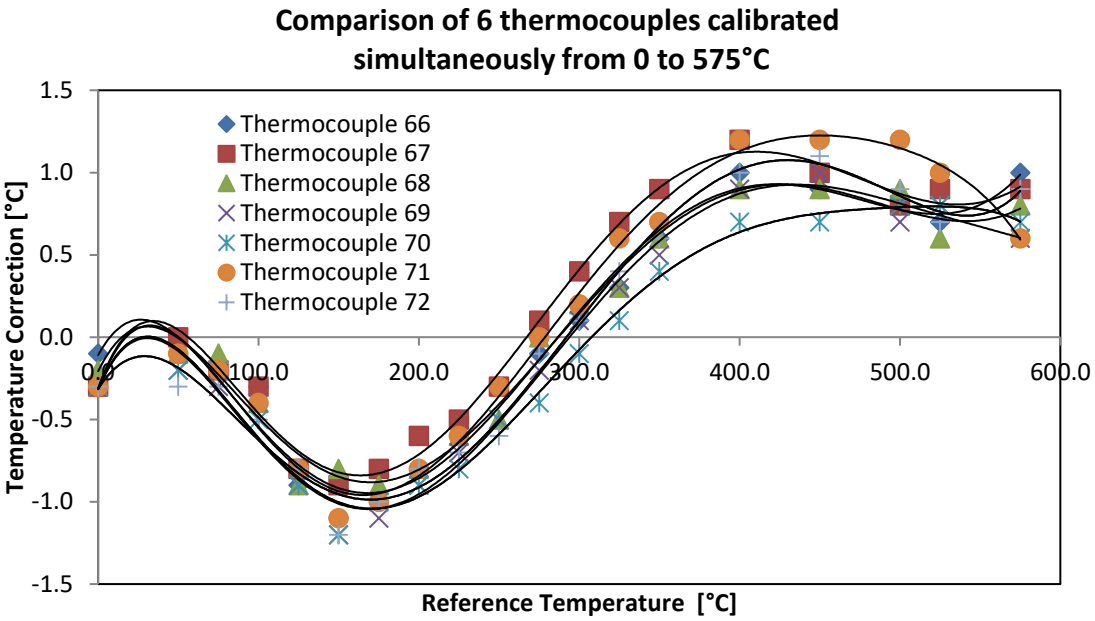

Figure 4-5: Six thermocouples calibrated over a temperature range of 0 to 575°C.

The ASTM standard [5] states an allowable error limit or drift limits for a Type K thermocouple. The limit states should apply throughout the thermocouple's life. If the limits are exceeded, then the wire's metal properties have changed too much and must be replaced. If limits are exceeded during calibration drift, then according to [5] the wire is simply not a Type K.

Table 4-2: Initial calibration tolerances for thermocouples.

Initial calibration tolerances for thermocouples			
Type	Alloy	Temperature range	Limit range
K	Chromel vs Alumel	0°C – 1250°C	±2.2°C or ±0.75% of reading in °C, whichever is greater

The thermocouple error falls within the described limit range shown in Table 4-2.

5. Methodology

The study to determine the extent of temperature and flow maldistribution for the final superheater outlet stubbox header required various methods. Each method was dependant on the completion of the previous method. The methods used during the dissertation are listed below:

- Data analysis
- CFD modelling
- FEA modelling using CFD results
- FEA modelling without CFD results

5.1 Data analysis

The data as received daily from the data logger, contained data collected over a time period of 24 hours (starting from 5 am) with a one-minute sampling frequency. Thus, there were 1440 temperature measurements for each of the 72 thermocouples, per data sheet (per day). In order to process the data, it first had to be sorted according the desired load conditions. Corresponding final steam pressure, steam temperature, outlet mass flow and boiler load data were requested from the plant DCS. It was requested that the data also be provided with one-minute sampling frequency so as to correlate with the thermocouple data. Using the boiler load data, the thermocouple measurements were sorted into three different load conditions, namely 100% load, 80% load and 60% load. These three loads were chosen due to the large amount of data that corresponded between the thermocouples and the boiler load measurements. By using the boiler load data, it could be verified when the thermocouple measurements were capturing transient conditions (boiler loads were ramping up or down) or approximate steady state conditions (if boiler loads were stable for long periods of time, see Figure 5-2). Since the aim of the dissertation was to compare results from different steady state load conditions, only the steady state data were used.

After sorting the thermocouple data between the three boiler loads, the final steam pressure, steam temperature and outlet mass flow data (from the plant's DCS) were also filtered for each of the three load conditions. As mentioned in the previous section, each of the 72 thermocouples correspond with a certain location on the final superheater headers. The locations for each of the thermocouples were added to the sorted data sheets, to better distinguish which metal temperatures matched with which location.

For each of the three load conditions, box and whisker plots were created in order to gauge the skewness for each of the 72 thermocouple data sets. For steady state conditions, the data should

be close to symmetrical and the median and mean values should be approximately the same. The structure of the box and whisker plot is shown in Figure 5-1 and gives an indication of the distribution of data and is comparable to a histogram [40].

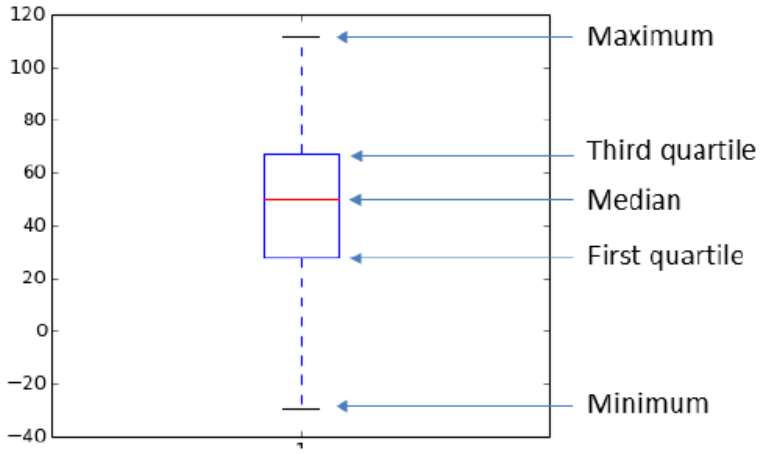

Figure 5-1: Box and whisker plot [40].

Figure 5-2 illustrates a section of approximate steady state data that was used during the data analysis. Although the temperatures fluctuated, the fluctuations were statistically stationary, with the maximum and minimum values staying constant.

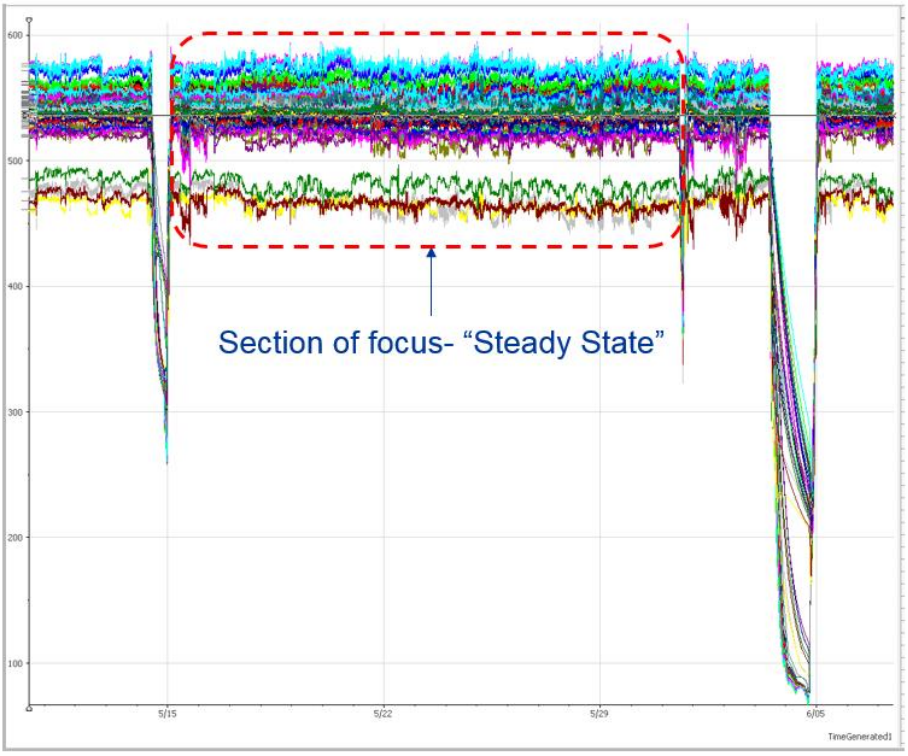

Figure 5-2: Approximate steady state data of the thermocouples.

5.2 CFD header process models

5.2.1 CFD model set up

The inlet and outlet final superheater headers were modelled in NX10, using detailed drawings of the superheater headers. The models were imported into FloEFD, keeping the model in SI units. In the CFD project set up, heat conduction, turbulent flow and adiabatic wall conditions were chosen. Adiabatic conditions assume that the outside wall of the headers is perfectly insulated (this assumption is justified in section 5.2.4). The internal fluid was set to steam and was chosen from the existing database in FloEFD.

5.2.2 CFD material properties

The header's material is based on European BS EN code material and was not found within the existing FloEFD database. For the outlet stubbox, the outlet header, end caps and outlet branches consist of 11CrMo9-10 forgings (as per EN 10222-2) and the tube stubs and outlet extension pieces consist of 10CrMo9-10 seamless tubing (as per EN 10216-2). However, 10CrMo9-10 and 11CrMo9-10 have the same heat capacity and thermal conductivity at elevated temperatures, as found in Table D.1, Appendix D of EN 12952-3. Thus, only one table had to be created for the heat capacity and thermal conductivity, as shown as in Figure 5-3.

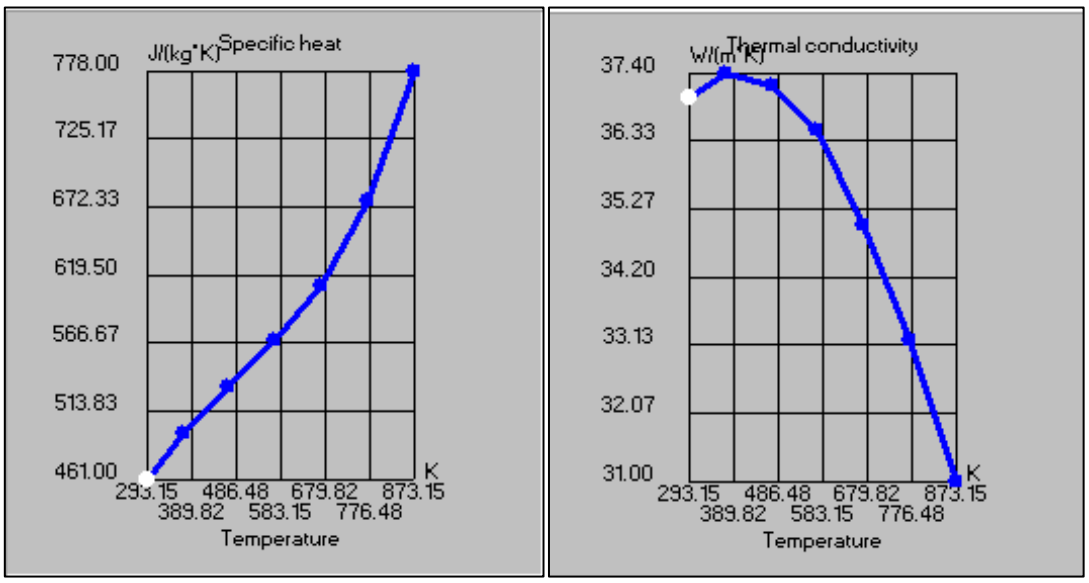

Figure 5-3: Material properties of 11CrMo9-10.

For the inlet stubbox header, the tube stubs consist of 10CrMo9-10 seamless tubes and the rest of the header consists of 13CrMo4-5 forging. Thus, for the inlet header and additional thermal conductivity, a new table had to be created for the forging material (see Figure 5-4).

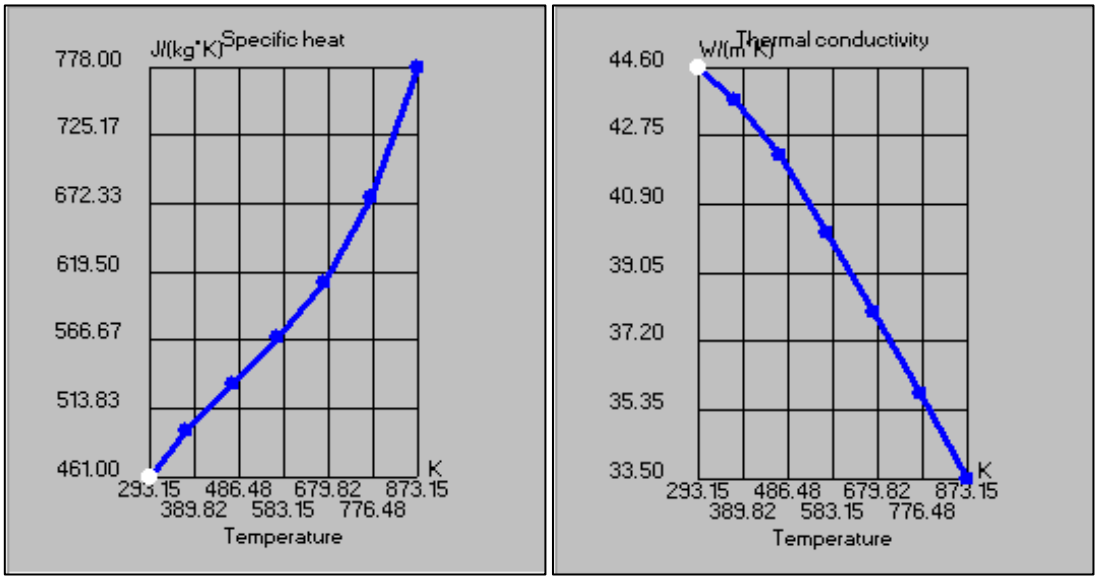

Figure 5-4: Material properties of 13CrMo9-10.

5.2.3 Process boundary conditions

For each of the 34 stubs, an inlet mass flow and steam temperature value were specified. An outlet pressure was specified at each of the two outlet branches. Thus, there were 36 boundary conditions in total for each model, with the location of the boundary conditions shown in Figure 5-5. The outlet pressure of 16MPa was provided from the power plant data and remains fairly constant for all three load conditions. Since adiabatic wall conditions were assumed and the stub walls are thin (12.5mm), it was assumed that the stub steam temperatures were approximately equal to that of the thermocouple metal temperature readings. A similar approach was used in a transient header simulation of reference [13]. For an initial estimation the total mass flow at the superheaters, as provided from plant data, was divided up equally among the 34 inlet stubs. At full load, the average total mass flow for Leg D (see Figure 4-1 and Figure 4-2) was 120.2 kg/s. Since there are seven elements per leg and 34 stubs per header, the estimated mass flow per stub was found to be 0.5kg/s (120.2/ [7x34]). The mass flow of 0.5kg/s was assumed for each stub in the adiabatic comparison and mesh convergence study, described in section 5.2.4 and 5.2.5 respectively. A more detailed mass flow estimation was conducted in section 5.2.6 and was used for the final CFD models.

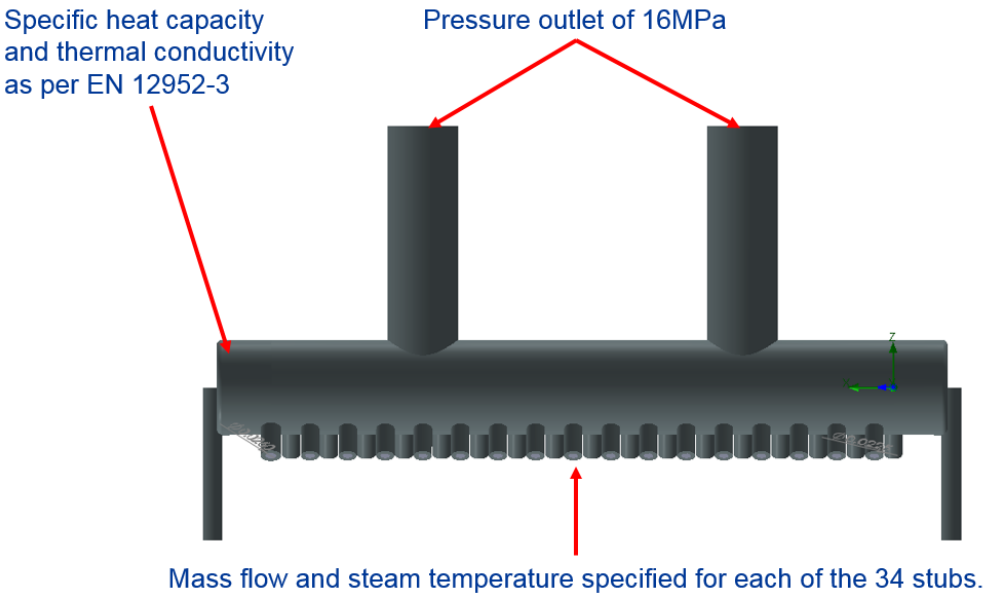

Figure 5-5: CFD boundary conditions.

5.2.4 Adiabatic assumption

In order to simplify and reduce the run time for each CFD run, it was assumed that the outside wall was perfectly insulated. The assumption closely resembles what occurs in reality, as casing boxes are installed around the stubbox headers and filled with insulation. In order to support the adiabatic assumption, a CFD model was created with insulation and was compared to a separate model without insulation, but assumed adiabatic conditions on the outside surface. The insulation geometry surrounding the outlet header was based on the header casing box drawing. The surrounding temperature of 300 °C was provided from site and is the standard temperature of the Penthouse at steady state conditions. The insulation's thermal conductivity was set at 0.2 W/m.K and is based on mineral wool insulation above 800K. Mineral wool insulation is typically used on these headers. Figure 5-6 shows the model with the modelled insulation (highlighted in blue). The exposed surface walls of the outlet branches on the top and the restrain posts at the bottom were insulated be applying wall boundary conditions set at zero heat transfer coefficient.

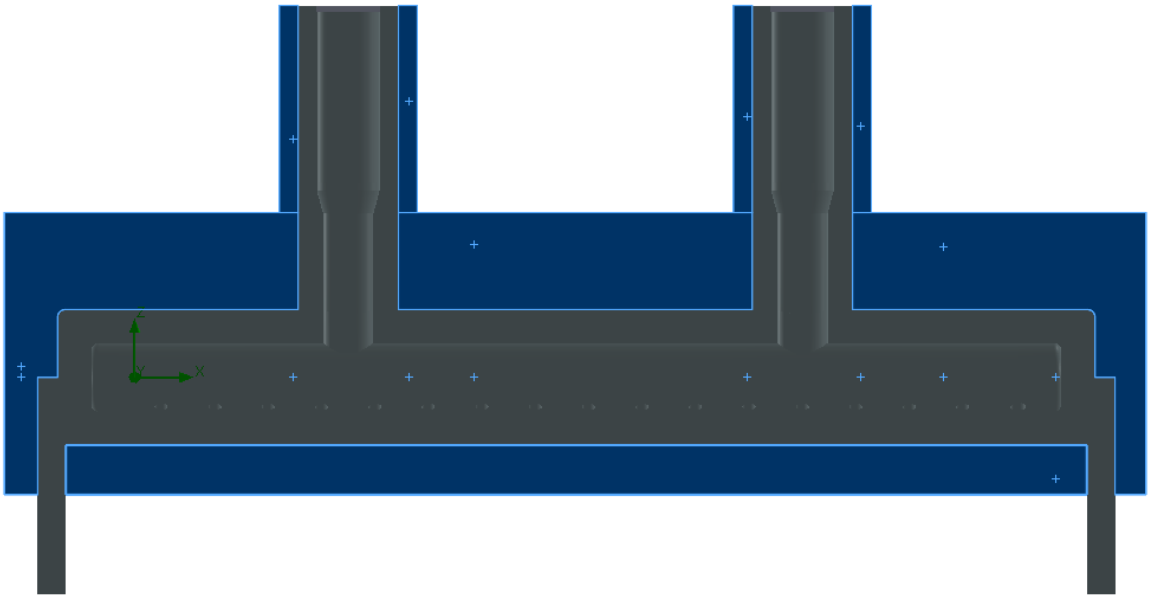

Figure 5-6: Outlet stubbox insulation.

The temperature distribution of the insulated header is shown in Figure 5-7. By comparing the surface plot shown in Figure 5-7 to that of an adiabatic model shown in Figure 6-5 (results section), it is evident that the temperature distribution is slightly different at either end of the header. The end caps of the header are the closest sections to the outside casing and thus have the least amount of insulation between them and the penthouse ambient temperature. The temperature distributions are more alike closer to the outlet branches and the centre of the header.

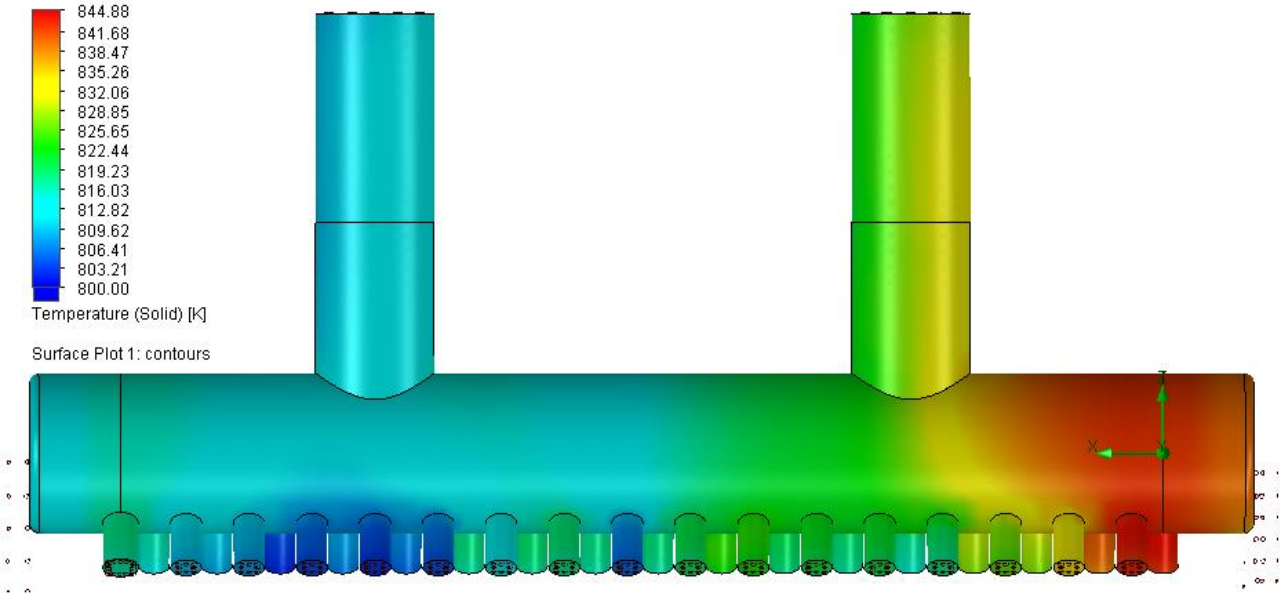

Figure 5-7: Temperature distribution for the insulated model [K].

The maximum temperature difference between the insulated model and the adiabatic model was found to be 3.7K at the rear (right-hand side) end cap. However, the temperature differences are negligible at the outlet branches, which implies that the overall steam temperature distribution

inside the header remains very similar between the two methods. See Table 5-1 for the comparison between the insulated and adiabatic model's average surface temperatures at the indicated locations.

Table 5-1: Average surface temperature comparisons between insulated and adiabatic model.

Front Outlet Branch			Rear Outlet Branch		
Insulated CFD Model [K]	Adiabatic CFD Model [K]	Temperature Difference [K]	Insulated CFD Model [K]	Adiabatic CFD Model [K]	Temperature Difference [K]
811.72	812.28	0.56	826.96	827.62	0.66
Front End Cap			Rear End Cap		
Insulated CFD Model [K]	Adiabatic CFD Model [K]	Temperature Difference [K]	Insulated CFD Model [K]	Adiabatic CFD Model [K]	Temperature Difference [K]
814.13	817	2.87	840.97	844.71	3.74

5.2.5 CFD mesh convergence

It is good engineering practice to perform a mesh convergence study for CFD simulations. Mesh convergence aids in finding a balance between computational memory during run time and converged results. FloEFD provides numerous methods for refining the mesh and cell densities, namely the minimum gap size, level of initial mesh, advanced channel refinement and manual mesh definition.

The minimum gap size is automatically set by FloEFD and is based on the smallest inlet and outlet openings at which the boundary conditions are set. It is important to apply all the relevant boundary conditions, before analysing the mesh. The gap size governs the computation mesh, so that a certain number of cells normal to the surface of the model will be generated as per the specified gap. In order to satisfy the minimum gap size conditions, corresponding parameters that govern the mesh are set by FloEFD, such as refinement levels and small solid features. If the aspect ratio between the model's overall size and the minimum gap size is more than 1 000, it will result in a large amount of small cells in sections where they are not required. Thus, specifying the minimum gap size is only applicable if the aspect ratio between the overall model and minimum gap size is small, as it is in this case [41].

The level of initial mesh governs the number of cells per the smallest passage height and the mean number of cells per the model's middle/mean size. The higher the level of the initial mesh, the higher

the number of cells in these locations. If both the geometry and flow field are relatively smooth, it is recommended to start at a level of initial mesh of 3.

The ratio of the model's middle size to the minimum gap size is called the geometric resolution coefficient, K_{res}. If the geometric resolution coefficient is much larger than one, it is recommended that the advanced channel refinement option is enabled [41]. When the advanced channel refinement is enabled, the software ensures that a sufficient number of cells are used to predict phenomena like boundary layers. The consequence of using the advanced channel refinement, is that the number of cells can increase by an order of magnitude.

By opting to use the manual option under the global mesh settings, more options are provided for slightly refining the mesh. It was found that by only using the automatic mesh settings, the difference in the number of cells between two consecutive runs was too high (more than a million cells). A high mesh density can result in a converged model but would be computationally expensive to run. Smaller differences in mesh density, between two consecutive mesh refinement runs, can also lead to convergence and will result in less computational effort. Under manual settings, advanced channel refinement can be maintained while adjusting the refinement of the cells and the number of channels. There are three types of cells in FloEFD, namely: solid, fluid and partial (cells intersecting solid and fluid domain) cells. Each of the three cells types can be refined, with the level of refinement denoting the minimum level to which corresponding cells must be split. The refinement level of the partial cells is set as the maximum level among all the selected levels.

It should be noted, that the mesh convergence study was performed before the correct mass flow distribution was established (see next section), and thus the metal temperature values in Figure 5-8, were not yet sufficiently close to that of the thermocouple readings. The initial mass flow of 0.5kg/s per stub was assumed. Although the changes in metal temperatures in Figure 5-8 are very small, the results converged when the model reached a total of 643 763 cells. The same mesh settings at the converged state (at 643 763 cells) were used for the partial loads. The number of cells shown in Figure 5-8 and Table 5-2 are the total number of cells, consisting of solid, fluid and partial cells.

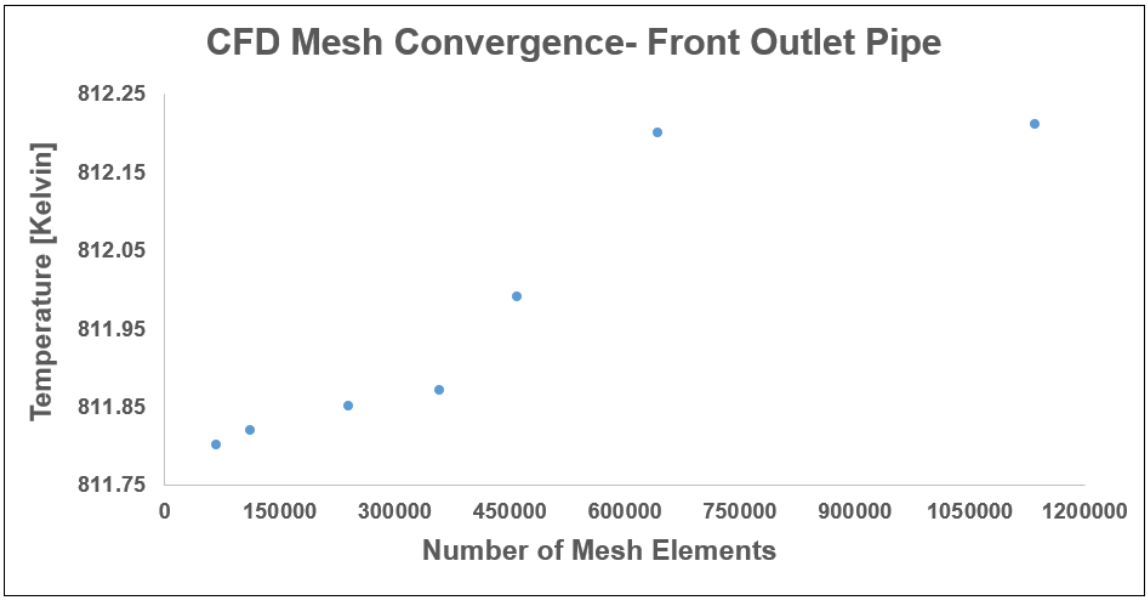

Figure 5-8: Mesh convergence study.

Table 5-2 shows the mesh settings used to refine the CFD model. The settings vary between manual and automatic mesh settings, where manual settings allow for more detailed refinement and automatic a more global refinement.

Table 5-2: Mesh settings for CFD.

Global Mesh	Mesh Settings	Number of Total Cells
Automatic	Initial mesh level at 3 and min gap=22.5mm.	68110
Automatic	Initial mesh level at 4 and min gap=22.5mm.	111000
Automatic	Initial mesh level at 3, min gap=22.5mm and advanced refinement enabled.	240188
Automatic	Initial mesh level at 3, min gap=11.25mm and advanced refinement enabled.	357832
Manual	Refinement level of all cell types set to 2 and number of cell across channel set at 5.	459035
Manual	Refinement level of partial cells set to 3 and number of cell across channel set at 5.	643763

Global Mesh	Mesh Settings	Number of Total Cells
Automatic	Initial mesh level at 5, min gap=22.5mm and advanced refinement enabled.	1134735

Figure 5-9 illustrates the converged CFD mesh that was used for all three load conditions. The cell density is specifically fine for the partial cells at the boundary between the fluid and the solid. Typically, in CFD simulations, time must be spent determining whether enough cells are created to capture the effect of the boundary layer. However, FloEFD makes use of boundary layer models based on a Two-Scales Function to describe flows in near wall regions. The function makes use of well-known wall functions and full velocity profiles, [42], for turbulent and thick boundary layers (number of cells across boundary layer is 6 or greater) [41]. For turbulent and thin boundary layers (number of cells across boundary layer is 4 or less), Prandtl boundary layer equations and the Van Driest hypothesis [42] about mixing length in turbulent boundary layers are used.

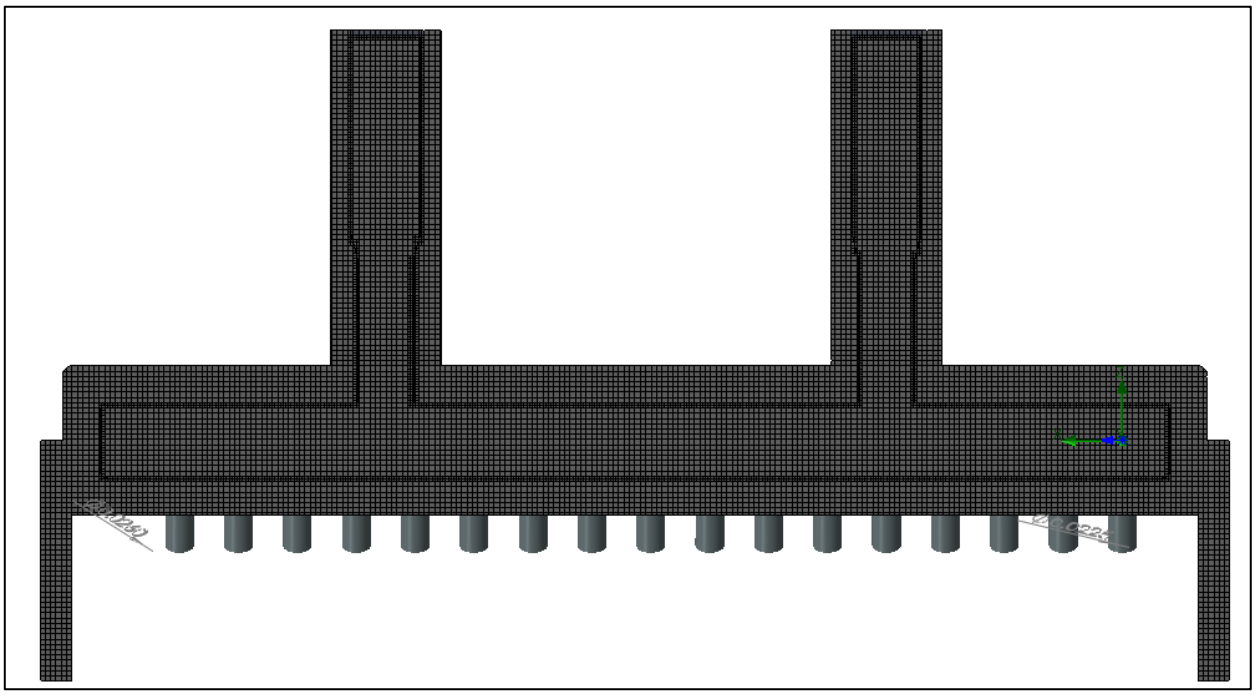

Figure 5-9: Converged CFD mesh for full load.

5.2.6 Mass flow distribution

With the installed thermocouples, the metal temperatures are known. However, the mass flow per tube could not be measured. A study was conducted to estimate the mass flow distribution across the outlet header. The mass flow distribution plays an integral part in determining the heat transfer

across the header. There are 34 tube stubs per header and thus 34 different mass flow values that had to be estimated. Two different methods were used to calculate the mass flow distribution, namely using a Flownex model and using a CFD model of the inlet stubbox header. After consideration the CFD method was chosen as the preferred option, with the reasons listed below:

- Only two assumed input variables were required for the CFD model, whereas the Flownex model required 34 assumed variables.
- There was no evidence to support any of the mass flow distribution combinations estimated with the parametric study in Flownex.
- Using the CFD model of the inlet stubbox would provide more realistic results, as the steam is fed from the inlet stubbox to the outlet stubbox.
- Flownex cannot accurately capture complex 3D mixing of steam in the headers nor the mass flow distribution once inside the header.
- Diagonal stub connection to the header cannot be modelled in Flownex.

Flownex model:

Flownex was initially considered because of the considerable decrease in run time, when compared to CFD, as well as its built-in functions to run parametric studies. The header was discretised into small sections between each of the stub connections. See Figure 5-10 for the layout of the model illustrating the steam temperature and mass flow inputs specified for each stub in different Excel spread sheets. Heat transfer elements were positioned at the corresponding locations of the thermocouples on the header and outlet branch. Excel components were used to specify steam temperature and mass flow values for the inlets of each stub.

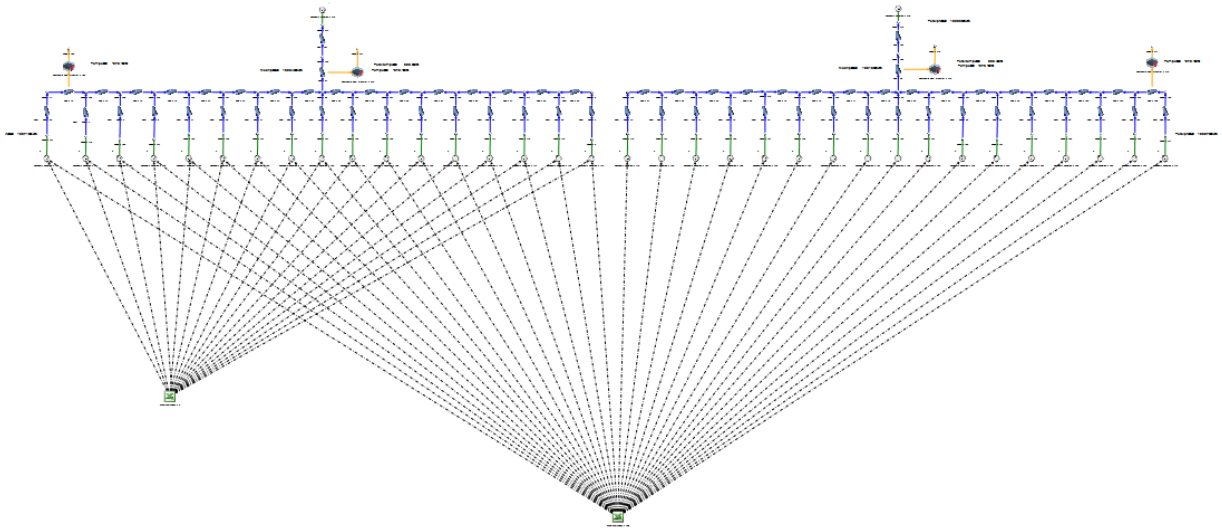

Figure 5-10: Flownex model of the outlet stubbox header.

Inlet Stubbox Header:

In the case for steady state conditions, the outlet mass flow rate at the inlet stubbox header should be equal to that at the inlet mass flow rate at the outlet stubbox header. By using the total mass flow rate per superheater leg, as acquired from the power plant, it was decided to model the inlet stubbox header in CFD in order to determine the mass flow for the outlet stubbox header. Together with the mass flow rates, conventionally one would have to estimate the pressure drop for each of the 34 tube loops across the final superheater element and use these as inputs for the outlet stubbox header. However, modelling the final superheater element was outside the scope of work for this dissertation, so plant data was used to specify the outlet pressure of the header. The common steam pressure of 16MPa, is the operating pressure of the steam leaving the final superheater system. As shown in Figure 5-5, the common steam pressure was applied to the outlet branches of the CFD model. It was assumed that the pressure losses between the outlet pipes and the manifold headers were negligible, implying that the common steam pressure at the outlet of the manifold headers is approximately the same as the outlet pressure of the outlet stubbox headers.

The mass flow entering each of the inlet stubbox headers was approximated by dividing the total mass flow per leg by seven, as there are seven headers per leg. The mass flow can then further be divided by two, assuming that each of the two inlet branches for the inlet stubbox receives an equal amounts of mass flow. From the inlet stubbox CFD results, each of the 34 exiting mass flow values were recorded and mirrored before using them as input boundary conditions for the outlet stubbox header. The mass flow values had to be mirrored due to the layout of the final superheater element. Tube 1 from the inlet stubbox becomes tube 34 for the outlet stubbox, thus each of the tube numbers are mirrored between the inlet and outlet stubbox headers. Figure 5-11 indicates the pathway of the steam flow as it enters the inlet stubbox header, flows through the final superheater element and exits into the outlet stubbox header.

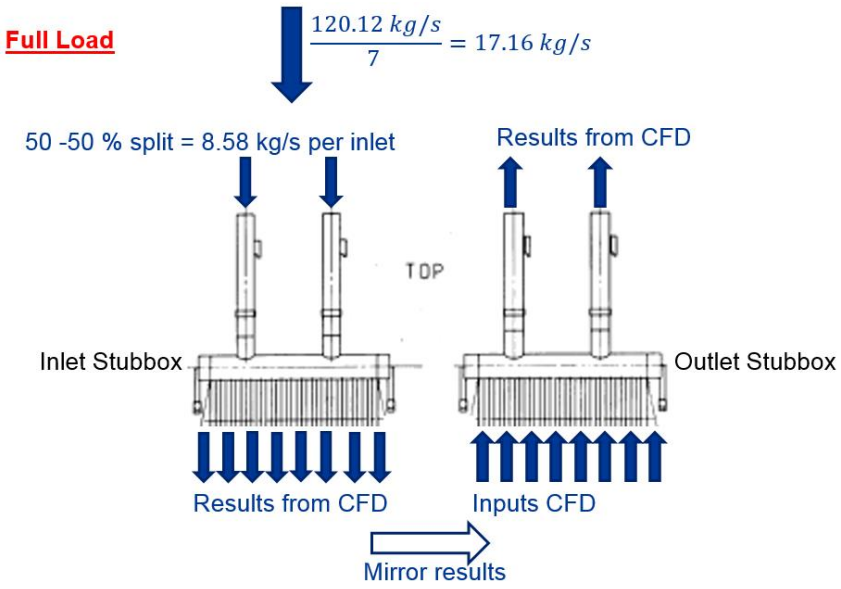

Figure 5-11: Mass flow estimation using the inlet stubbox.

The mass flow distribution results at the outlet of the inlet stubbox, resembles what was seen in a CFD mass flow study (Figure 2-16) for headers [17]. The higher mass flow rates are at the stubs that are aligned with the inlet branches. The mass flow rates increase towards the centre and ends of the header due to the steam build up before exiting through the stubs. Figure 5-12 illustrates how the mass flow values were mirrored between the inlet and outlet headers, for each of the three load conditions.

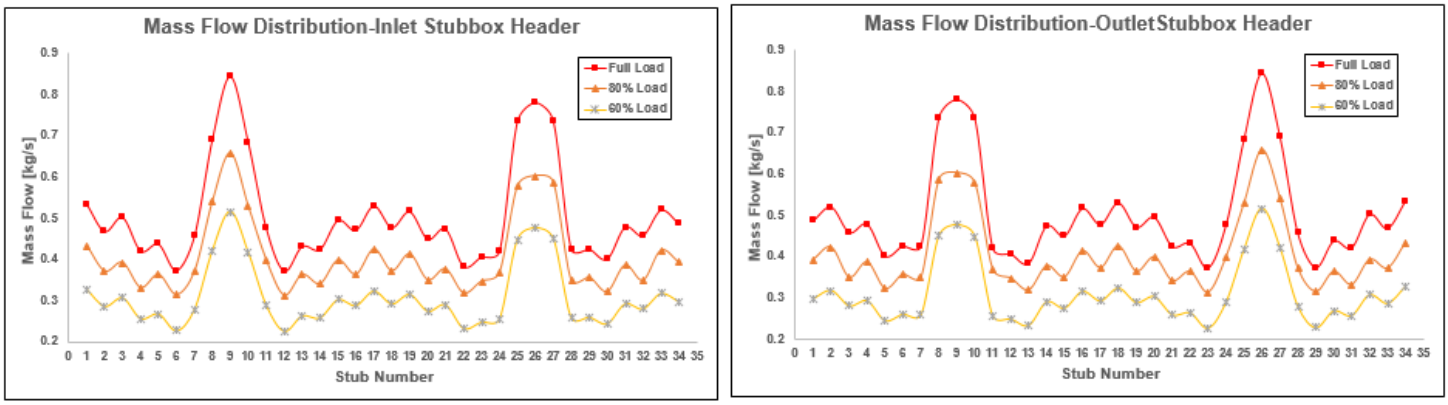

Figure 5-12: Mass flow distribution for the superheater headers.

Each mass flow boundary condition in the CFD models were specified to be fully developed at the entrance of the openings. The steam flow will be fully developed by the time it reaches the outlet stubbox header.

5.3 Thermo-mechanical method

By examining the common thermo-mechanical approaches listed in section 2.5, it was concluded that this dissertation will employ a combination of conjugate and non-coupled FEA/CFD analysis. The conjugate heat transfer, internal convection and conduction heat transfer in CFD analysis determined the metal temperatures at key boiler load conditions and these temperatures were imported (or mapped) into FEA by interpolating the temperature to the FEA model's nodes. The FEA will use the supplied temperature profile to determine the thermal stresses.

5.3.1 Importation of CFD results into FEA

In this particular case, the exact mesh used for CFD simulations cannot be transferred into the FEA simulations, the main reasons being that the elements used by the CFD and FEA software packages are incompatible and the mesh refinement differs. FloEFD has the built-in function to export CFD results to an FEA mesh, by interpolating the temperatures of each node to that of the FEA mesh. After the temperatures have been assigned to the nodes, the solid/metal temperature for each node can be accessed in an output text file. The export function in FloEFD also applies to split FEA models, such as the quarter model shown in Figure 6-12. FloEFD will automatically export the temperature to split sections, as long as the split sections precisely overlap with that of the CFD model.

In MSC Patran, a FEA software package, a spatial field can be created and linked to a boundary condition. The node numbers and corresponding metal temperatures can be imported from the text file into a csv Excel file and in turn be imported into the FEA spatial field. After the spatial field has been created, it can be linked to temperature boundary conditions and applied to all the nodes in the model. It should be noted that MSC Patran was used due to the ease of importing CFD results, compared to other FEA software packages such as Marc Mentat. See Figure 5-13 below for an example of the CFD-FEA coupled output file, containing the node number and the corresponding solid temperature. Depending on the settings in FloEFD, the temperature can either be specified in Kelvin or degrees Celsius.

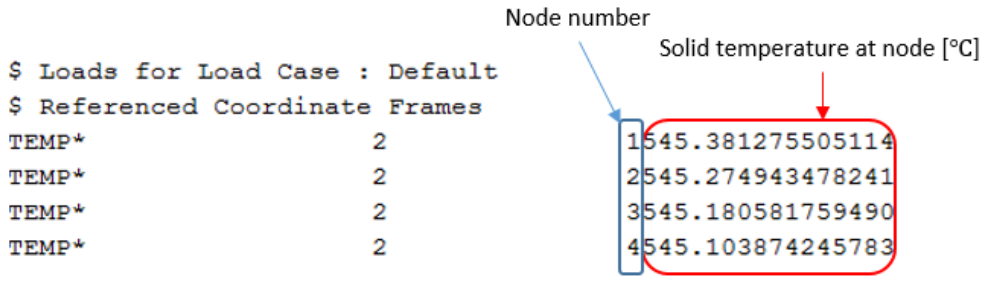

Figure 5-13: CFD-FEA coupled output file.

5.3.2 Symmetrical modelling

Symmetrical modelling is often employed in FEA to simplify and reduce the required amount of boundary conditions as well as to reduce run time. Symmetrical modelling assumes however, that the model geometry, material properties, constraints and load are all symmetrical about the centre lines or planes of symmetry. The temperature profile was found to be close to symmetrical about one of the symmetry planes, as shown in Figure 5-14. It was assumed that the front of the header (left-hand side) will not significantly contribute to thermal stresses and can be ignored when modelling in FEA. In order to justify the assumption, the thermal stress results of the symmetrical model or quarter model were compared to that of the whole model. The comparison of the results is later shown in section 6.5.4.

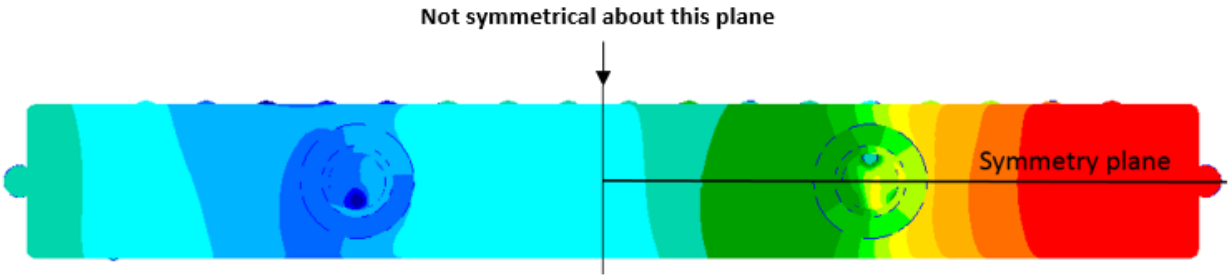

Figure 5-14: Plan view of symmetry planes for thermal loading.

5.3.3 FEA model mesh

Using NX10, a mesh was created specifically for the FEA simulations. Similarly to CFD, a mesh convergence study is generally performed for FEA simulations. When performing mesh convergence studies, the mesh density can be refined in the FEA software and the simulation can be re-run using the same boundary conditions. In this case, each time the mesh is refined, a new model must be saved and exported to CFD. The temperature boundary conditions must be reapplied after the CFD results have been loaded. On average, the FEA models also ran longer and used more storage space, when compared to the CFD models. By taking these factors into account, it was decided to create a mesh for the whole model based on a previous Babcock study [43] of similar headers. Further refinement was conducted with a quarter section of the model (see Figure 5-16) specifically around the borehole regions of the header. In the Babcock study, the outlet header was modelled (only a quarter of the model was created as symmetric boundary conditions were justified) and was used for the Design by Analysis method as specified in the European code EN 13480. For that model, thermal stresses were ignored, and internal pressure was applied. The header's design pressure was used and it resulted in high local stresses. The type and number of elements through the various thicknesses that resulted in converged stress values are listed in Table 5-3. The type and number of elements used for this dissertation's FEA model is also listed and compared in Table 5-3.

Table 5-3: FEA Elements through the Thickness.

Section	Required amount of elements through the thickness	Whole Model	Quarter Model
Outlet branch	HEX20-2 elements	TET10-3 to 4 elements	TET10 – 3 elements
Main header body	HEX20/TET10-5 elements	TET10-6 elements	TET10-7 to 8 elements
Stubs	TET10-1 element	TET10 -1 element	TET10- 1 element
End cap inner radii	TET10-8 elements	TET10 -8 elements	TET10- 8 elements

The cross section of the header in Figure 5-15 below shows the refinement of the whole model. All the elements are connected at the nodes and no glue contacts were used. Glue contact refers to connecting dissimilar elements, such as hexahedral (HEX) to tetrahedral (TET), without having the dissimilar elements share nodes. Glue contact can lead to stress discontinuities between these dissimilar elements, and it was decided to avoid such discontinuities when local thermal expansion occurs between the nodes.

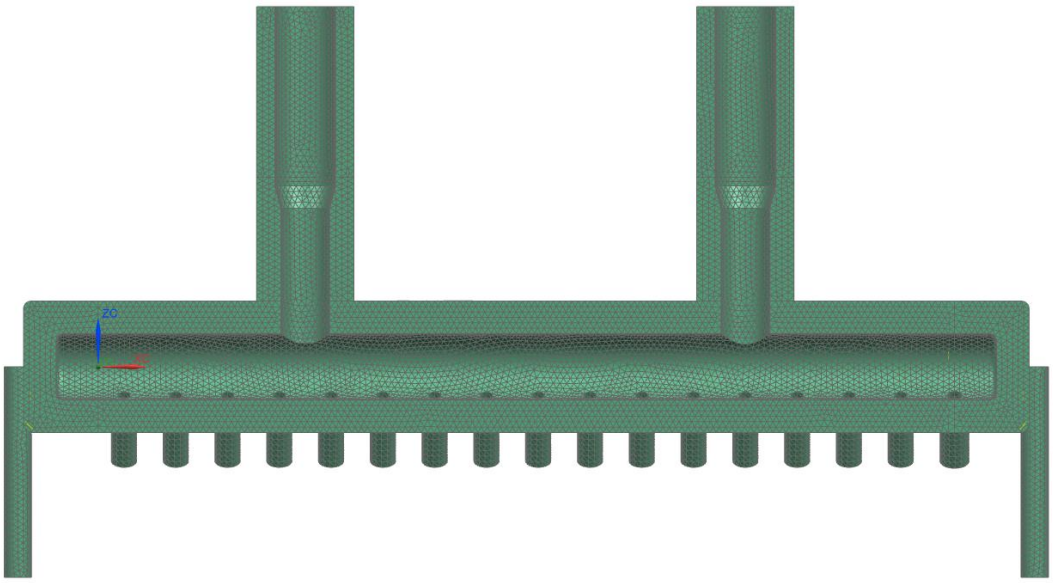

Figure 5-15: FEA mesh density for the whole model.

The quarter model has a refined mesh density at the borehole regions around the stubs and outlet branch. The quarter model contains 142 087 elements and 207 286 nodes. Splitting a model is preferred in terms of run time, as regions of interest can be refined while retaining relatively few nodes. The symmetrical boundary conditions ensure correct expansion under thermal or mechanical loads.

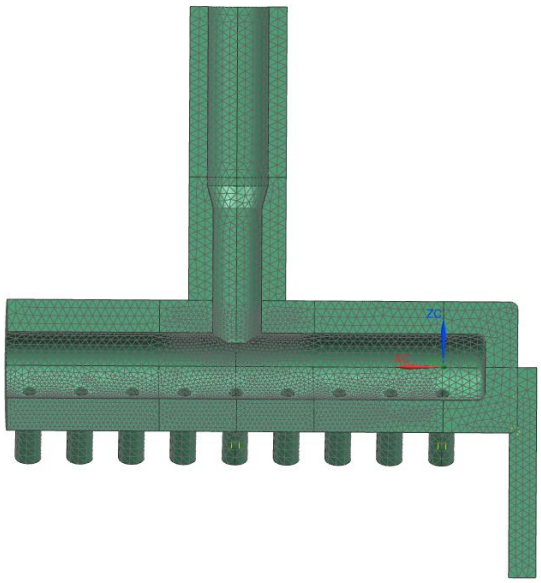

Figure 5-16: FEA mesh density for quarter model.

For each FEA model, second order 10-noded tetrahedral (TET) elements were used, as they have been proven to produce accurate results [44]. TET elements are suitable for non-parametric solids and are generally used for 3D models. Non-parametric solids are shapes that have more than five to six sides, such as solids that contain holes. When TET elements are used, it is preferred to use the second order elements, TET10, rather than first order element, TET4 [45]. Second order elements imply that there are additional mid-nodes and free edges when compared to first order elements. Second order elements are less stiff than first order elements (TET4); they capture sharp edges and curves in a model more accurately and they provide better accuracy in capturing deformation. The drawback of second order elements are that they result in significantly more nodes and thus require more computation power and time.

5.4 FEA header models

For the FEA models, eleven different load cases were used to compare the impact of symmetrical modelling, CFD results, boiler load conditions and internal pressure on thermal expansion in FEA. The thermo-mechanical approach, section 5.3, was used for the all load cases, except for load case 7. For load case 7, the internal convective heat transfer, calculated in the CFD models, was assumed to be negligible. The model only considered thermal expansion due to conductive heat transfer, see section 5.4.4 for more details.

The eleven different load cases are listed below:

Case 1 -3: FEA models for all three load conditions, using CFD results. Only stresses due to thermal expansion were considered. Case 1-3 will indicate full, 80% and 60% load respectively. The whole header was simulated using MSC Patran.

Case 4-6: FEA models for all three load conditions, using CFD results. Only stresses due to thermal expansion were considered. Case 4-6 will indicate full, 80% and 60% load respectively. A quarter of the model was simulated using MSC Patran.

Case 7: FEA model for full load, without CFD results. Only stresses due to thermal expansion were considered, with heat transfer performed within Marc Mentat and the structural analysis performed in MSC Patran.

Case 8: FEA model for internal pressure without thermal expansion. A quarter of the model was simulated using MSC Patran.

Case 9-11: FEA models for all three load conditions, using CFD results. Stresses due to internal pressure and thermal expansion were considered. A quarter of the model was simulated using MSC Patran.

5.4.1 Thermal expansion constraints

For pressure parts subjected to high temperatures, thermal expansion must be considered when the constraints are designed. When boundary conditions are set up for FEA models under thermal expansion, the constraints must not restrict expansion as to induce unrealistic stresses, but at the same time must not allow rigid body motion. Rigid body motions imply that deformation is zero or very small and the model freely translates or rotates in an unconstrained degree of freedom.

Various different combinations of boundary conditions were applied to the model and in most cases the induced stresses due to incorrect constraints were above yield strength. Only after consulting with expert supervisors at the specific power station, was the correct combination of boundary conditions established. The correct boundary conditions will result in realistic magnitude of stresses and expansion in the correct directions. The thermal expansion boundary conditions for the whole header model as shown in Figure 5-17 , were used for load case 1 to 3 and load case 7. Load case 1 to 3 and load case 7 are applicable for the whole model.

The constraints must allow the header to expand in the axial direction (along the x-axis) and downward (z-axis) without rotating. Since the header must be allowed to expand, neither the stubs nor the outlet pipes should be restrained from translating in the x-direction. The axial expansion complicates matters as FEA requires a constraint in the x-direction to prevent rigid body motion, but excessive constraints would result in high stresses. A single node, located at the bottom centre of the header, was constrained in the x-direction and allowed the header to realistically expand from the mid-point without creating stresses in the solid. The top two faces of the outlet pipes were fixed from translating in the z-direction and the two bottom faces of the restraint posts were fixed from rotating in any direction.

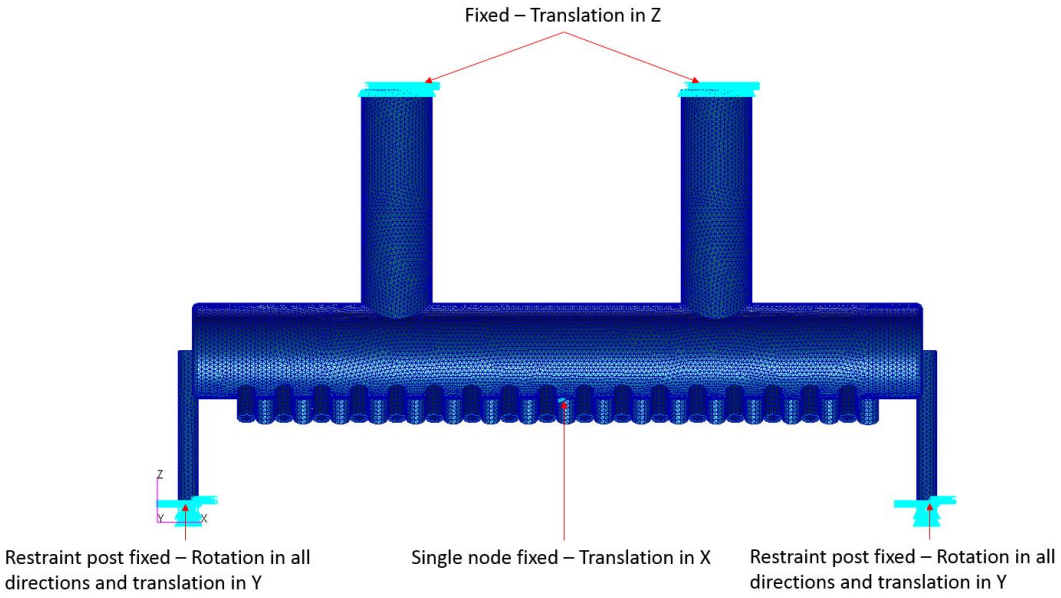

Figure 5-17: Constraints against thermal expansion.

The quarter model, Figure 5-18, uses symmetrical boundary conditions that allow the header to expand in the correct direction, by constraining the translation perpendicular to the planes of symmetry (translation in x and y-direction). Symmetrical boundary conditions also provide more assurance that rigid body motion will not take place, whilst preventing constraints from inducing stresses on the model. As with the boundary conditions applied to the whole model, the top face on the outlet pipe was fixed from translating in the z-direction and the bottom face of the restraint post was fixed from rotation in all directions. The symmetrical boundary conditions shown in Figure 5-18, were used for load cases 4 to 6 and 8 to 9. These load cases use the quarter model in the analysis.

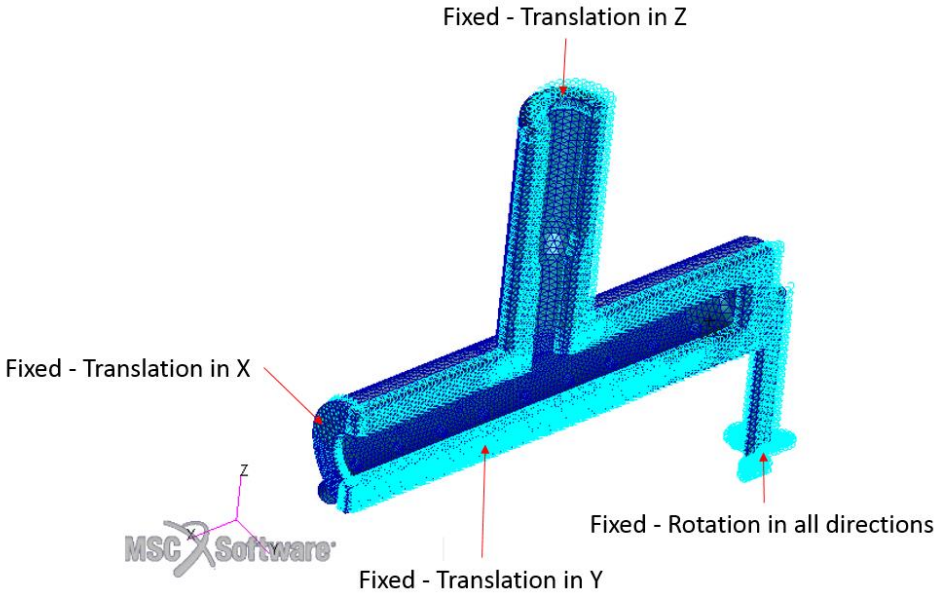

Figure 5-18: Symmetrical boundary conditions utilized for the quarter model.

5.4.2 FEA mechanical loads

The final superheater elements are physically supported from notched support lugs, welded to the inlet pipes of the inlet stubbox header and to the outlet pipes of the outlet stubbox headers. Due to the symmetry of the elements, the support lugs on the inlet pipe should carry the same load as the support lugs on the outlet pipes. It was for this reason that gravity was included in the model and was applied to all the load cases, including thermal expansion. If gravity was not included in the thermal expansion models, the outlet pipes would want to expand upwards against the fixed boundary condition and high stress would be induced on the model. Gravity insures that the header realistically expands downwards during thermal expansion.

Including gravity, additional mechanical loads were added for load case 8 to 11. Half the weight of the longest element tube loop, together with the weight of internal steam, was estimated at 199kg (at stub 34). The load due to the longest tube loop was conservatively applied to the face of each stub. The red highlighted sections in Figure 5-19 illustrate what was modelled for CFD and FEA and the yellow highlighted sections indicate what was excluded from the model. The yellow highlighted section was excluded in order to decrease the required amount of elements and thus running time. Due to the angle at which the stubs are connected to the header, there will both a vertical (F_{VR}) and horizontal reaction force (F_{HR}) component at the connection between the stubs and the header. The horizontal distance between the fixed stub connection to the header and the force due to the tube weight, will result in a bending moment (M_x) about the stub connection.

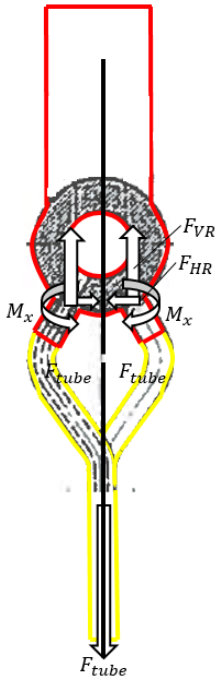

Figure 5-19: Reaction forces at the stub connections.

In FEA, bending moments cannot directly be applied to 3D solid elements. A system of nodal and/or pressure loads can be used to equate to the required bending moment. Figure 5-20 illustrates the location and direction of the mechanical loads applied in FEA. The resultant force,F_R, was estimated using the dead load of the tube weight, F_{tube} and the angle at which the stubs are inclined. The resultant force thus ensured that the correct reaction forces occur at the connection. An additional vertical load, F_V, was applied to create a bending moment about the connection. The resultant force was applied using a pressure load, as pressure loads always act perpendicular to the element face and no local coordinate systems is needed to ensure the force points into the correct direction. The vertical load was applied as a total load, with the specified load evenly distributed across all the nodes on the face of the stub.

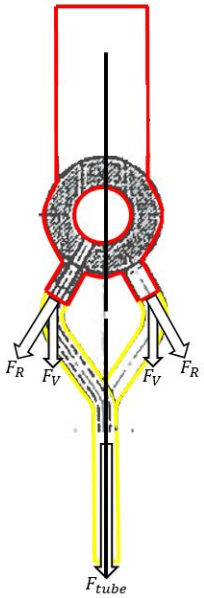

Figure 5-20: FEA applied mechanical loads.

5.4.3 Pressure reaction forces

For load case 8 to 11 (see section 5.4 for descriptions) internal pressure was applied to the inside surface of the quarter model. When internal pressure is applied to a 3D header or vessel, a reaction force equal to that of the internal pressure times the internal area must be applied to each opening. If the correct pressure reaction forces are not applied to each of the header openings, then undesirable model deflection and stresses at the constraints can occur. The magnitude of imbalance can often be measured by examining the reaction forces at the constraints in the FEA results. The pressure reaction forces due to the internal pressure was calculated by multiplying the internal operating pressure by the internal opening area of the applicable stub. The pressure reaction force can then be applied as pressure loading by dividing the force over the area of the applicable stub face.

It should be noted that the mechanical loads described here and in 5.4.2 were only applied to the quarter model, as attempting to balance the reaction forces for the whole model can be complicated and can lead to incorrect results. The inner surface to which the pressure was applied is highlighted in Figure 5-21 and the mechanical loads for each stub are shown in Figure 5-22.

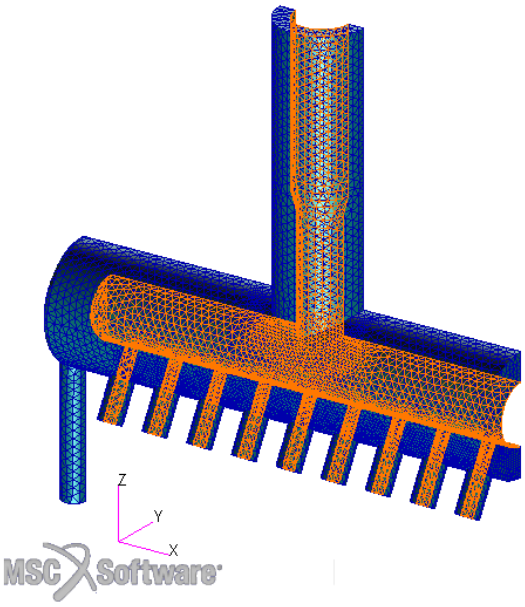

Figure 5-21: Applied internal pressure of 16MPa.

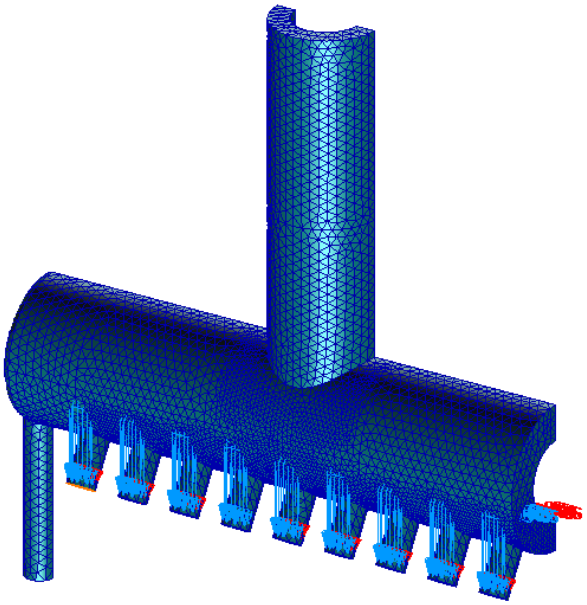

Figure 5-22: Mechanical loads for FEA.

5.4.4 FEA model without CFD results

For load case 7, a FEA model was set up in Marc Mentat, with the aim of assessing solid temperatures and stresses without using the results from CFD simulations. The results of the two different FEA methods are to be compared to see if CFD is necessary for steady state conditions.

The FEA model comprises of two integrated processes, namely a thermal analysis and a structural analysis. The thermal analysis contains its own set of boundary conditions for heat transfer and the temperature results can be imported into the structural analysis as a state variable boundary condition. The structural analysis made use of the same structural constraints shown in Figure 5-17. Marc Mentat does provide the option to run the thermal and structural analysis as one, with the structural analysis initiating after the completion of the thermal analysis. However, the thermal analysis was performed separately in order to verify that the boundary conditions were applied correctly.

Most FEA models for superheater headers found in literature, do not utilize CFD for the calculation of the heat transfer through the headers. In these cases, different heat transfer coefficients were calculated and applied to the inner and outer walls of the superheater header and branches. It is generally assumed that the heat transfer coefficients do not change across the header's length at steady state conditions and thus one heat transfer coefficient value can be applied to the entire surface of the header. It is also assumed that the heat transfer boundary conditions on superheater headers are symmetrical and thus only half or a quarter of the header needs to be modelled. However, from the CFD results it was seen that the heat transfer coefficients change across the header's lengths, and that symmetrical boundary conditions cannot be assumed when performing heat transfer.

This FEA method assumes, at steady state conditions, that heat transfer due to internal convection can be ignored and only thermal conductivity needs to be taken into account. Adiabatic boundary conditions, zero heat flux, were applied to both the outer and inner surfaces of the header, see Figure 5-23.

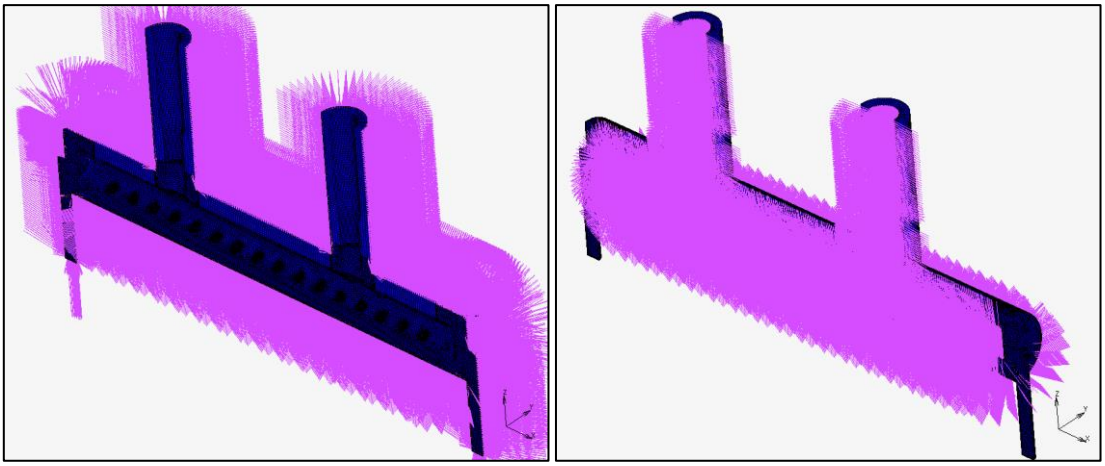

Figure 5-23: Zero heat flux applied to inner and outer surfaces.

Furthermore, each of the 34 stubs were set at the solid temperature value of the corresponding thermocouple reading at full load. An initial boundary condition was created so that the model was

set at a uniform temperature of 528°C. Initial boundary conditions help the model to converge faster during heat transfer analysis.

5.4.5 FEA material properties

For the structural FEA analysis, only two material properties are required, namely thermal expansion and Young's Modulus. Both of these properties vary with temperature. The European code EN 12952-3 provides tables and polynomial equations for these material properties. The two graphs shown in Figure 5-24 were plotted using the polynomial equations together with the corresponding polynomial coefficients.

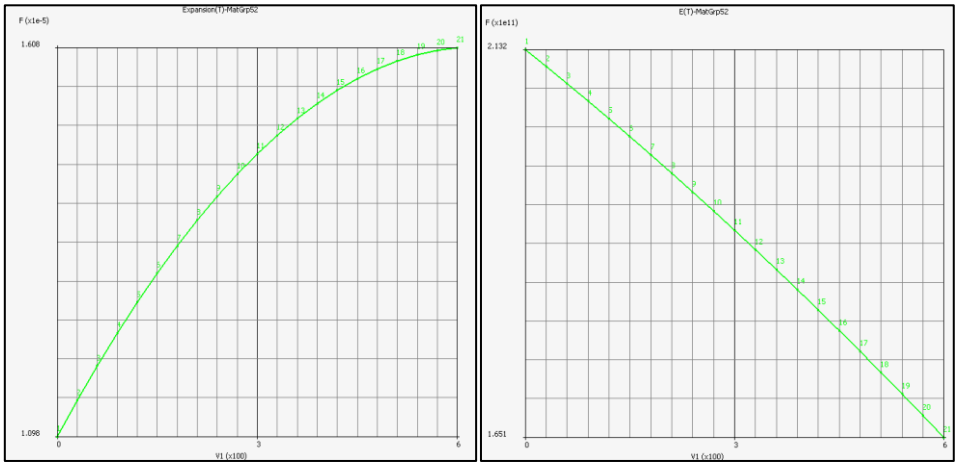

Figure 5-24: Material properties – Thermal expansion (Left) & Young's modulus (Right).

See polynomial equations *(5-1)* and *(5-2)* for the modulus of elasticity and the thermal expansion respectively. Both the equations are a function of the metal temperature in ℃. Since the expected stresses should not exceed yield, only linear elastic behaviour was analysed. Thus, plasticity was not considered.

$$E = [213.16 - 6.91 \times 10^{-2}(T) - 1.824 \times 10^{-5}(T^2)] \times 10^9 \qquad (5\text{-}1)$$

$$\alpha = [10.98 + 1.623 \times 10^{-2}(T) - 1.287 \times 10^{-5}(T^2)] \times 10^{-6} \qquad (5\text{-}2)$$

6. Results and discussions

6.1 Thermocouple results

After reviewing the thermocouple data, it was found that the temperature on the right-hand side (at stub 34 and facing the rear of the boiler, see Figure 6-1) of the outlet stubbox header was consistently higher than that of the left side (at stub 1 and facing the front of the boiler). The maximum temperature differences across the stubs for the outlet stubbox were 40 ℃ at full load and 43 ℃ at partial loads. The temperature difference between these two sides can be attributed to the difference in the final superheater element tube loop lengths. The final superheater element consists of 34 tube loops connected between the inlet and outlet header and are situated within the boiler, below the roof tubes of the penthouse. The tube loop lengths increase from stub 1 to 34. The longer tube loops have greater surface areas than the shorter tube loops and thus more heat can be transferred from the flue gas to the tube material. The longer tube loops also have more friction against internal steam flow and thus could result in the steam flow slightly reducing.

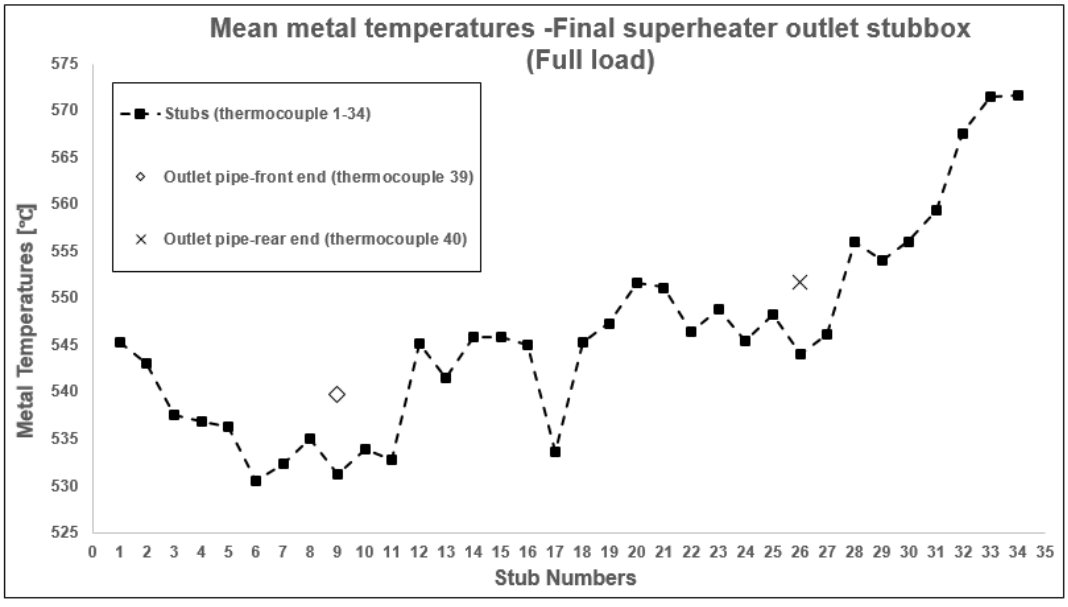

Figure 6-1: *Mean metal temperature – Final superheater outlet stubbox at full load.*

The temperature profile dips slightly at stub 9 and stub 26. These two stubs are perfectly aligned with the outlet branches at the top of the header and the temperature dip can be attributed to the higher mass flow at these two stubs. The metal temperatures fluctuate during steady state conditions; however the fluctuation is such that the mean and the median temperature values should be approximately equal to each other and thus the data distribution is symmetrical. It can be seen from Figure 6-2 that the mean line passes through the median line of the box and whiskers

charts. The box and whiskers charts also show that the maximum and minimum thermocouple values for each stub are approximately equal in distance from the median lines.

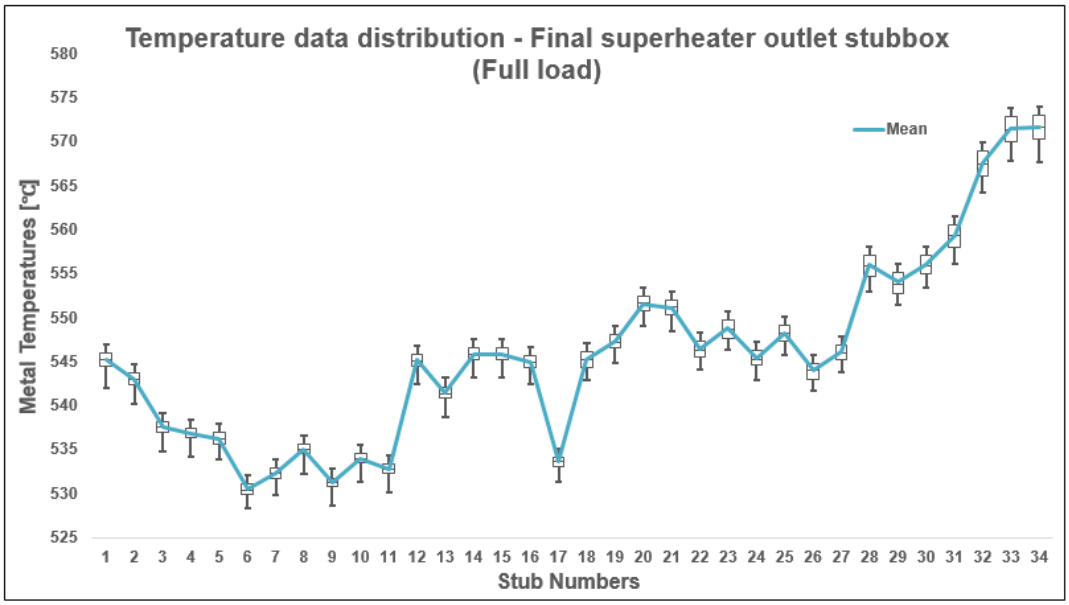

Figure 6-2: Temperature data distribution – Final superheater outlet stubbox.

The temperature profile at full load, across the outlet stubbox stubs, are similar for 80% and 60% loads, see Figure 6-3. The avergage temperatures at 80% load are higher than that of full load and are due to higher temperature spikes during the same measured time range. At 60% load, it can be seen that the average temperatures are less than full load from stub 1 to 11, approximately equal to full load from stub 12 to 18 and fluctuates above full load from stub 19 to 34. Even though the overal average temperatures for 60% load are less than full load, there are higher temperature difference across the stubs at 60% load. The higher temperature difference at the partial steady state loads lead to higher thermal stresses, as shown in section 6.4.

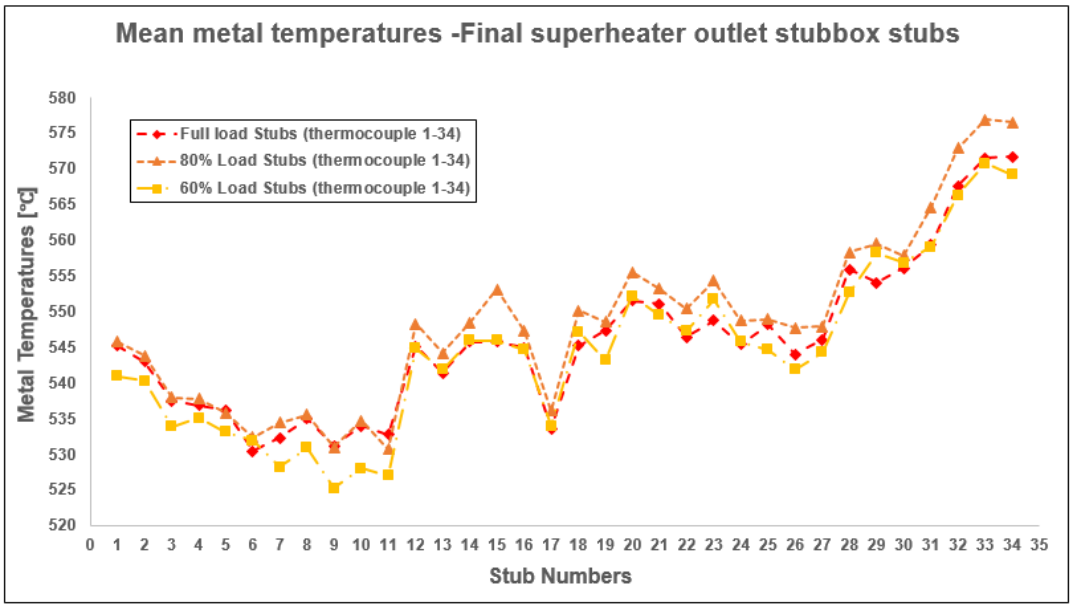

Figure 6-3: Final superheater outlet stubbox for each of the three loads.

From Figure 6-4, the lowest temperatures were found at element 1 and element 28, supposedly due to the additional cooling provided by the evaporator walls to the flue gas. Element number 1 to 7 represents the measurements taken on the left-hand side of manifold header 1, element number 8 to 21 represents the measurements taken on the middle of manifold header 2 and elements 22 to 28 represents the measurements taken on the right-hand side of manifold header 1. The temperature readings for element are hotter (LHS of boiler) than elements 15 to 28 (RHS of boiler) and illustrates that temperature maldistribution does occur across these elements and thus the manifold headers. There is maximum of 40 ℃ temperature difference at manifold header 1 (elements 1 to 14) during partial loads.

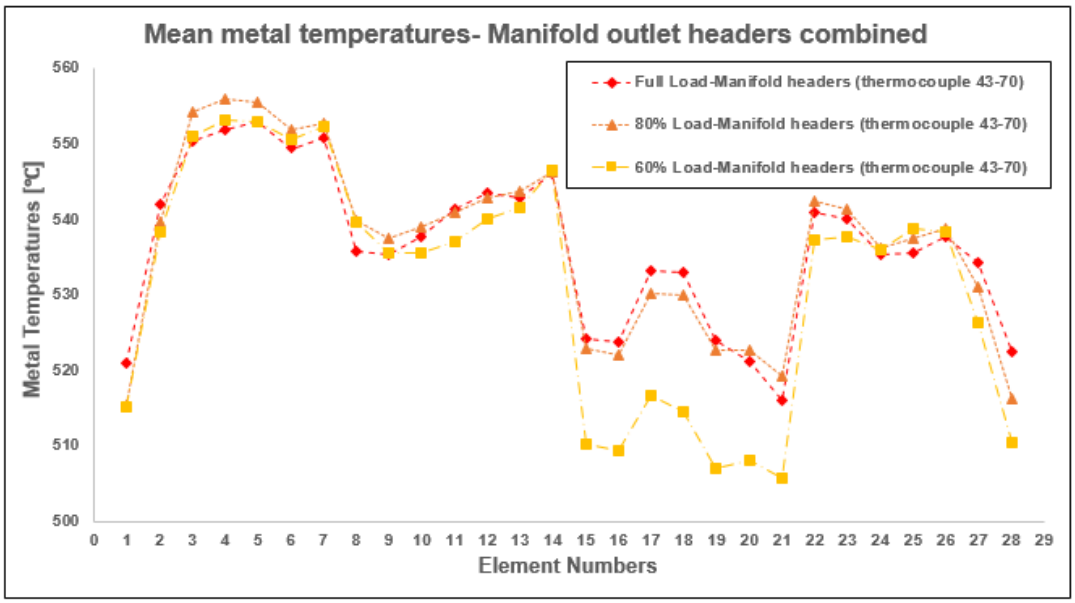

Figure 6-4: Manifold header temperature distribution for all three load conditions.

6.2 CFD results

6.2.1 Adiabatic Model Results

Figure 6-5 shows the surface plot of the solid temperature distribution at full load. The thermocouple readings indicated (see Figure 6-3) that the tubes at the rear side of the header (right-hand side) were consistently hotter than the tubes at the front of the header. The hotter tubes, and by implication the hotter steam flow, resulted in the rear side of the header being hotter than the front side.

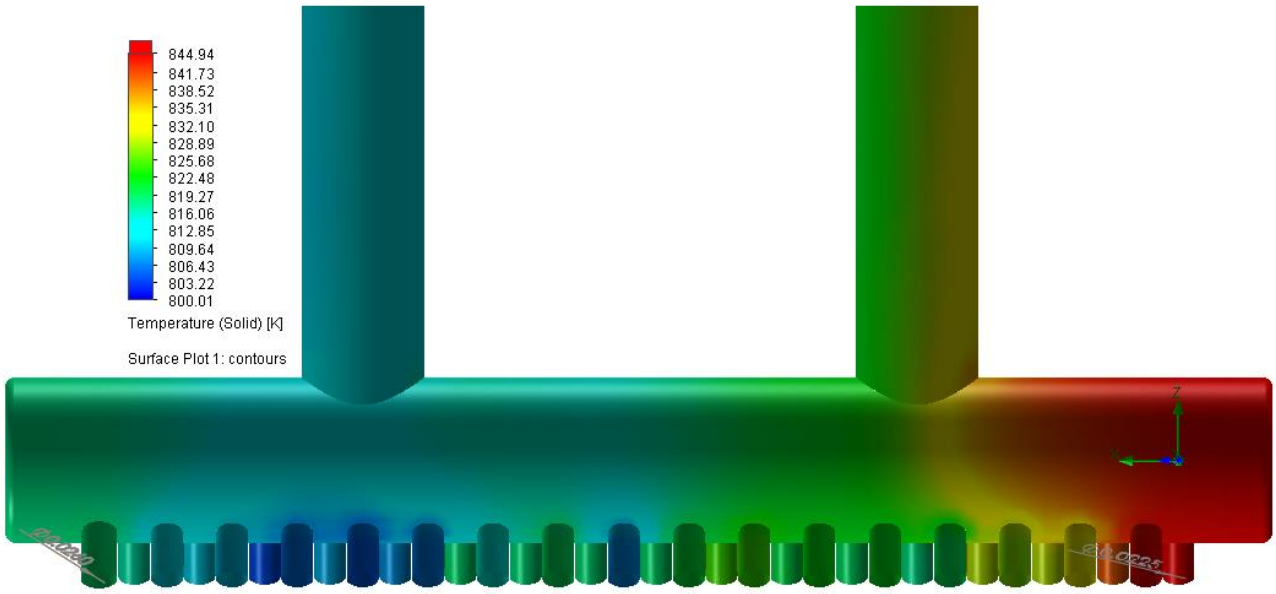

Figure 6-5: Solid temperature surface plot at full load [K].

It was assumed that the metal temperature readings for each of the stubs are approximately the same as the respective steam temperatures. The assumption is justified by the results shown in Table 6-1. The highest temperature difference between the assumed steam temperature and the CFD metal temperature for tube 34 was 0.1 Kelvin. The difference is negligible and indicates that the steam and metal temperatures are almost exactly the same during steady state conditions.

Table 6-1: Steam temperature vs tube temperature.

	Tube 1			Tube 34		
Loading condition	Steam temperature [K]	Tube temperature [K]	Temperature difference [K]	Steam temperature [K]	Tube temperature [K]	Temperature difference [K]
100% Load	818.41	818.35	0.06	844.87	844.97	0.1
80% Load	819.00	818.93	0.07	849.75	849.79	0.04

	Tube 1			Tube 34		
Loading condition	Steam temperature [K]	Tube temperature [K]	Temperature difference [K]	Steam temperature [K]	Tube temperature [K]	Temperature difference [K]
60% Load	814.10	814.03	0.07	842.39	842.41	0.02

In order to validate the CFD results, the thermocouple readings at the outlet branches were compared to the CFD solid temperatures. Table 6-2 shows the temperature difference between the CFD temperature results and the thermocouple readings at the three different load conditions. For the outlet pipes, the highest temperature difference was found to be 0.82 Kelvin. Thus, the assumed mass flow distribution together with the converged mesh resulted in acceptable CFD temperature distribution values.

Table 6-2: CFD results vs thermocouple readings.

	Front Outlet Branch			Rear Outlet Branch		
Loading condition	CFD temperature [K]	Thermocouple [K]	Temperature difference [K]	CFD temperature [K]	Thermocouple [K]	Temperature difference [K]
100% Load	812.59	812.87	0.28	825.72	824.89	0.83
80% Load	814.67	814.08	0.59	828.27	828.272	0.002
60% Load	809.96	810.29	0.33	823.69	823.96	0.27

The temperature distribution of the steam inside the header can be seen from Figure 6-6 and Figure 6-7. The complex steam temperature distribution inside the header explains why one-dimensional process models, such as Flownex, cannot accurately predict the temperature and flow distributions.

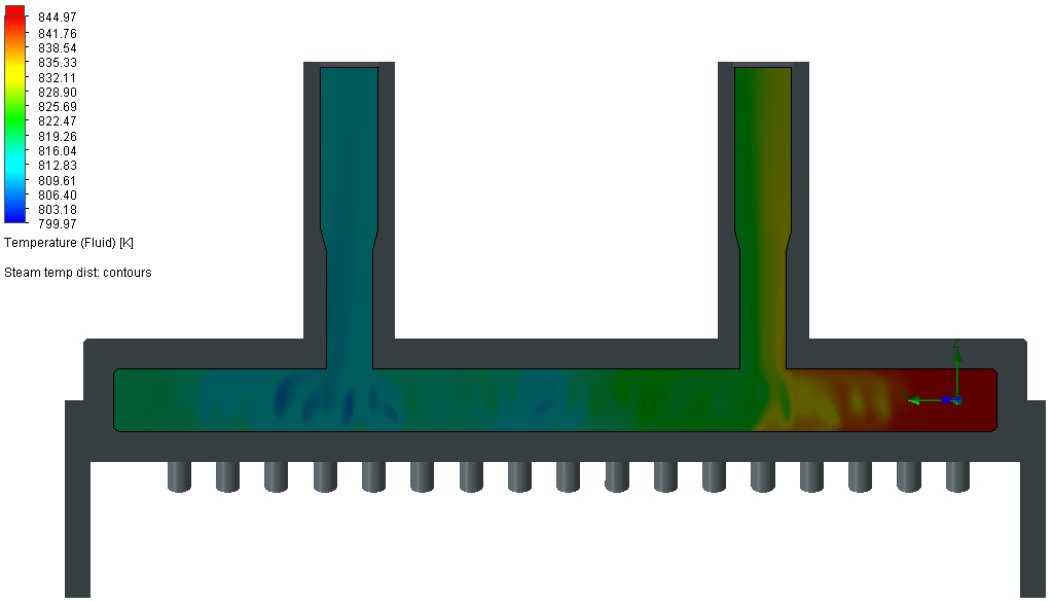

Figure 6-6: Cut plot of steam temperature distribution at full load [K].

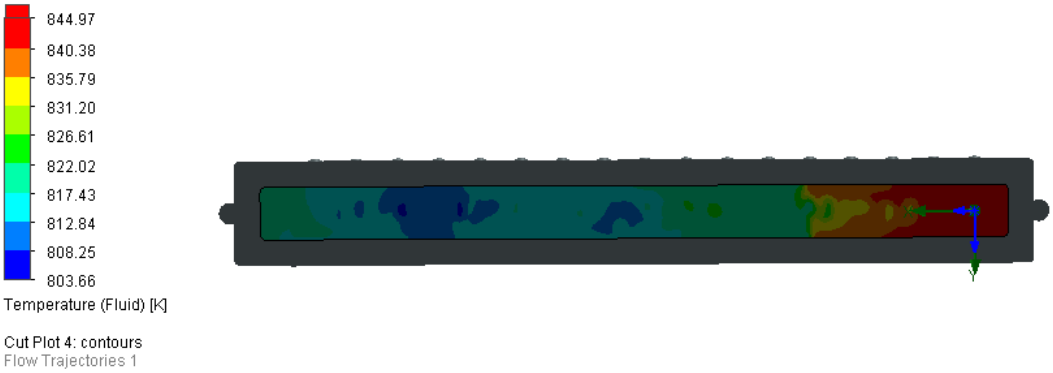

Figure 6-7: Plan view of steam temperature distribution at full load [K].

The velocity of the steam flow increased at the entrance of the two outlet branches, see Figure 6-8. The mass flow at the inlet of the outlet branch ranges between 32m/s to 39m/s and correlates well with the mean velocity of 32m/s, calculated by using the cross-sectional area of the inlet and by assuming that each outlet receives approximately half the total mass flow across the header. The equation for mass flow in terms of the mean velocity across the cross section of a tube is shown below:

$$\dot{m} = \rho A V_m \qquad (6\text{-}1)$$

where $\dot{m}$ is the mass flow rate, ρ is the water or steam density and V_m is the mean velocity.

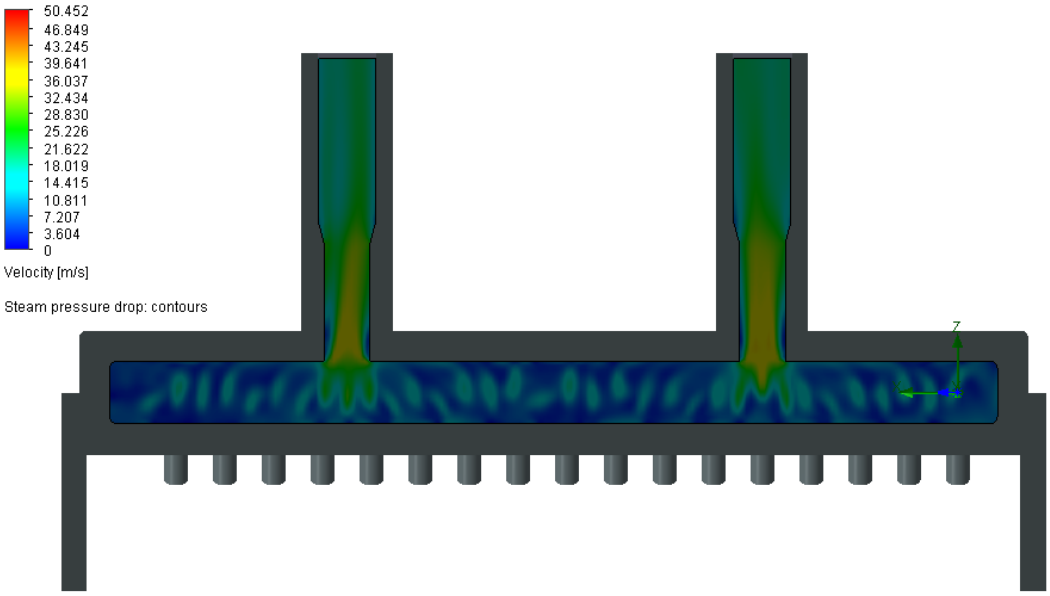

Figure 6-8: Cut Plot of steam flow velocity [m/s].

At full load, it was found that the maximum pressure drop across the header was 81kPa.

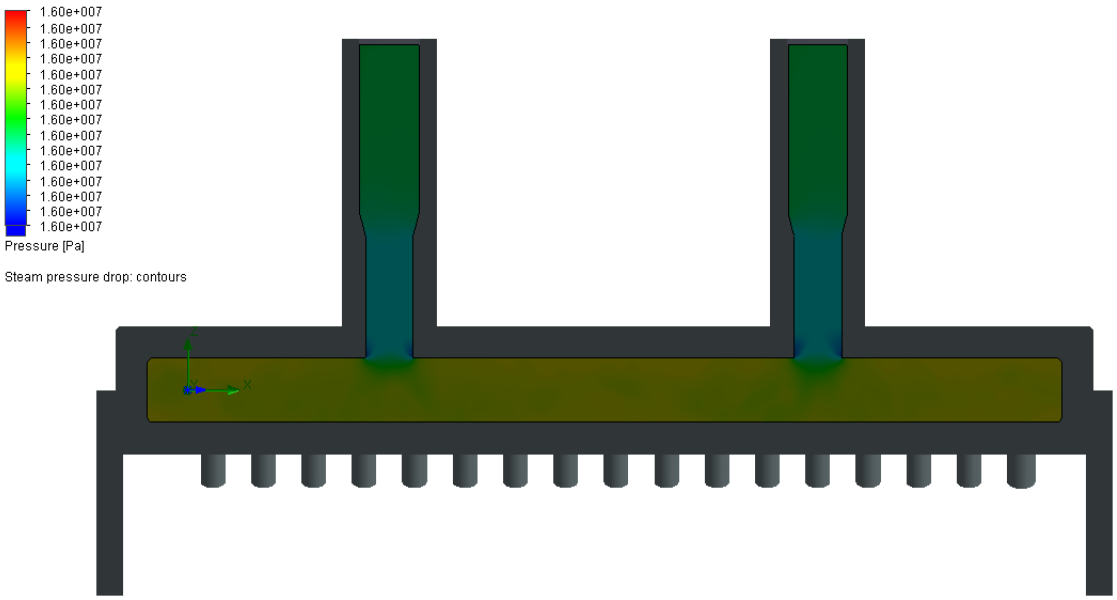

Figure 6-9: Steam pressure distribution in CFD [Pa].

6.3 FEA temperature distribution

6.3.1 FEA-CFD temperature distribution

The temperature distribution across the header can clearly be seen from the FEA (MSC Patran) contour plots in Figure 6-10 and Figure 6-11. Even though the temperature distribution in Figure 6-10 and Figure 6-5 are the same, the temperature contours are more distinguisable when plotted

in MSC Patran.The highest temperature gradient can be seen across the rear outlet branch (right-hand side) and thus higher thermal stresses can be expected in this region.

The CFD temperature distribution at full load, 80% load and 60% load was applied to load case 1, 2 and 3 respectively.

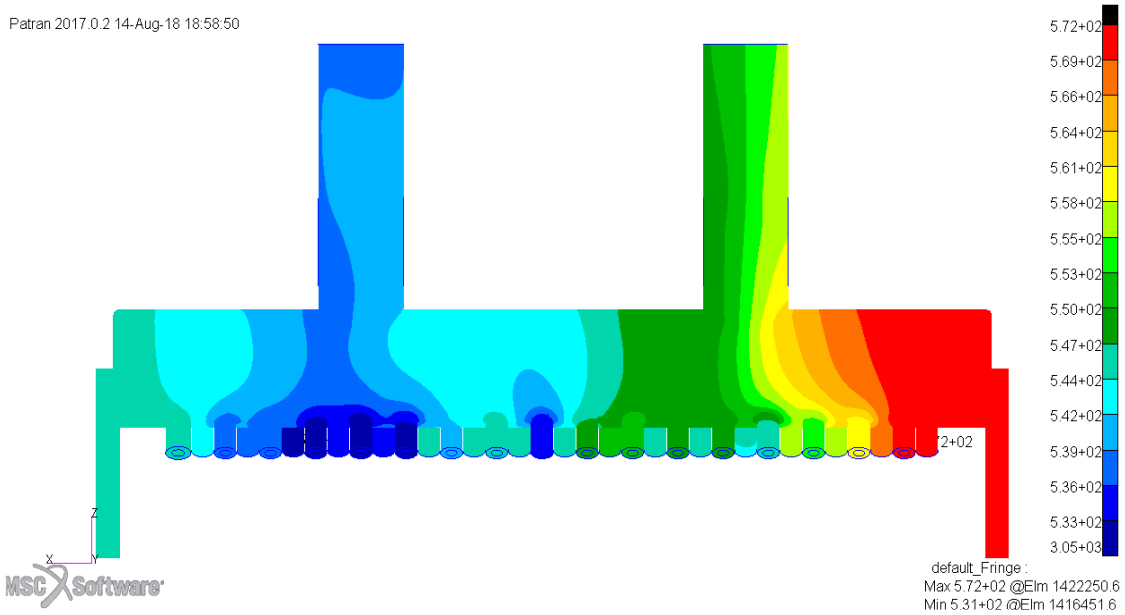

Figure 6-10: Case 1 - front view contour plot of nodal temperatures at full load [°C].

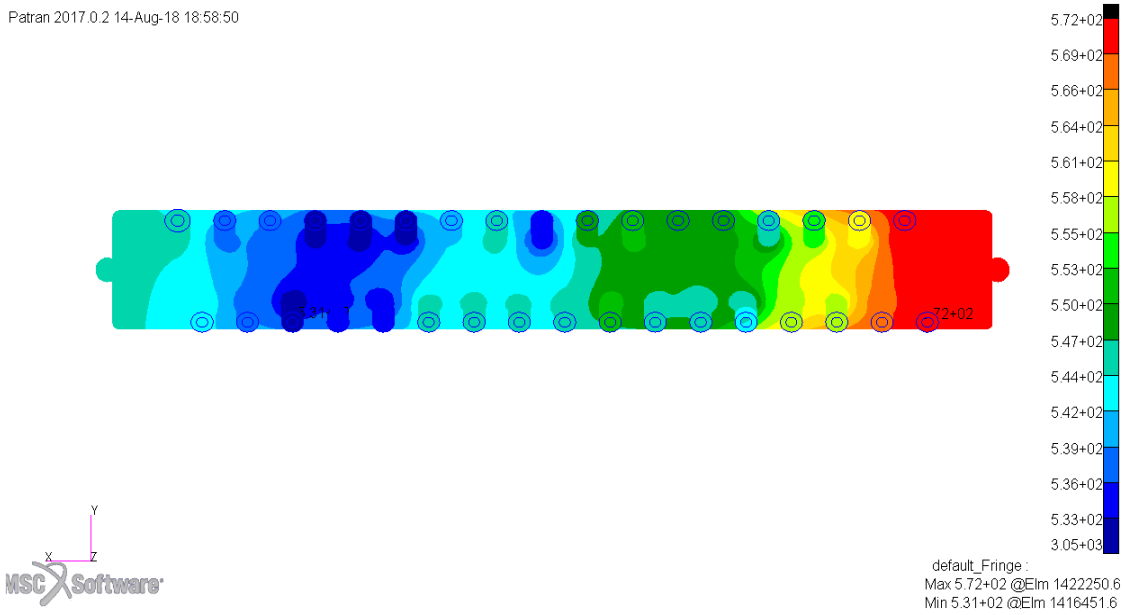

Figure 6-11: Case 1 - bottom view contour plot of nodal temperatures at full load [°C].

As mentioned in section 5.3.1, FloEFD provides a means to export the CFD temperature results to a sectioned model, such as the quarter model shown in Figure 6-12 below. The temperature distribution for the quarter model, is exactly the same as for the whole model, Figure 6-10, in the corresponding region.

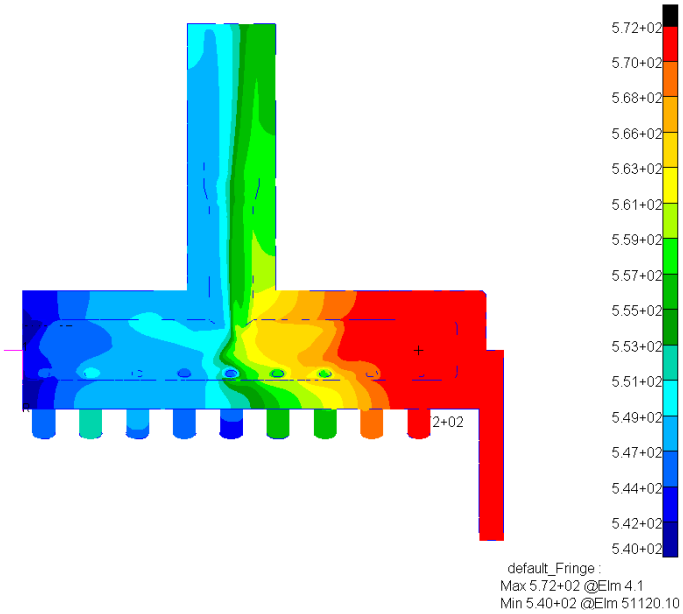

Figure 6-12: Case 5-quarter model at full load [°C].

6.3.2 FEA model without CFD results

The thermal analysis for load case 7 was performed in Marc Mentat and imported into MSC Patran. The thermal analysis assumed adiabatic conditions on the internal and external surfaces of the model and thus only conductive heat transfer was considered, see section 5.4.4.The resulting temperature disruptions are shown in Figure 6-13 and Figure 6-14. The temperature distribution in Figure 6-14 closely resembles Figure 6-11, indicating that conduction heat transfer by itself will provide similar results to CFD results at the stub connection to the header. By comparing the temperature distributions between Figure 6-10 and Figure 6-13, it is noticeable that that two heat transfer methods would render similar thermal stresses at the stub connections but differ at the outlet branches. The metal temperatures of the two outlet branches in Figure 6-13, do not match the thermocouple readings tabulated in Table 6-2.

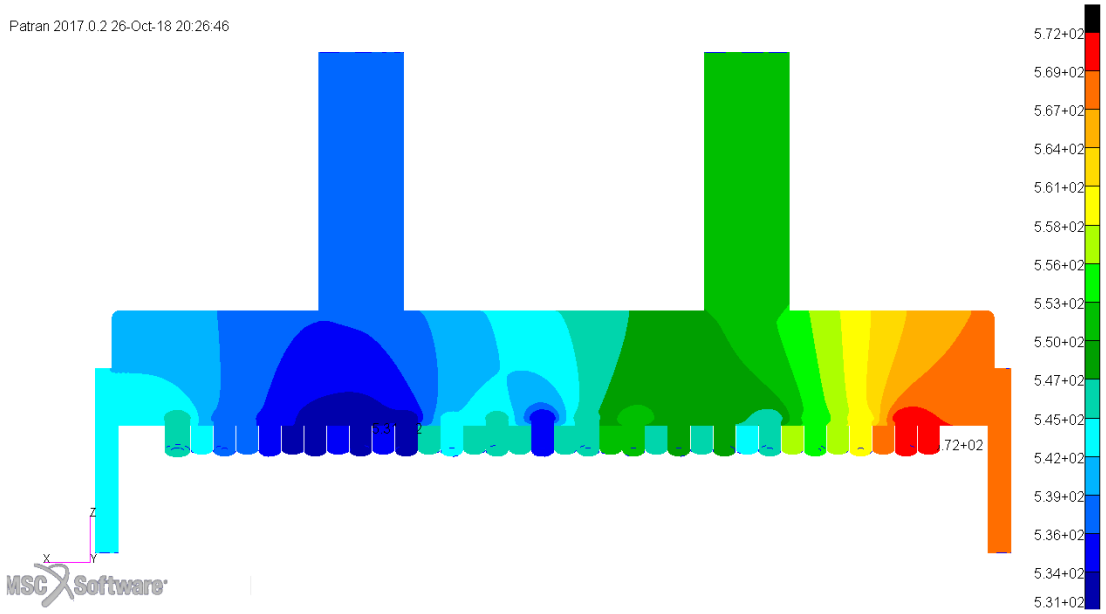

Figure 6-13: Case 7- front view of temperature contour plot at full load [°C].

Figure 6-14: Case 7 - bottom view of temperature contour plot at full load [°C].

The difference in temperature distribution between the FEA-CFD (case 1) and uncoupled FEA method (case 7) at full load are shown in Figure 6-15 and Figure 6-16. Figure 6-15 compares the temperatures at stub 17, with the temperature range set between 530°C and 544°C. The difference in temperature distributions at stub 17 are minimal, which indicates that the thermal stress values will be similar in range in this region.

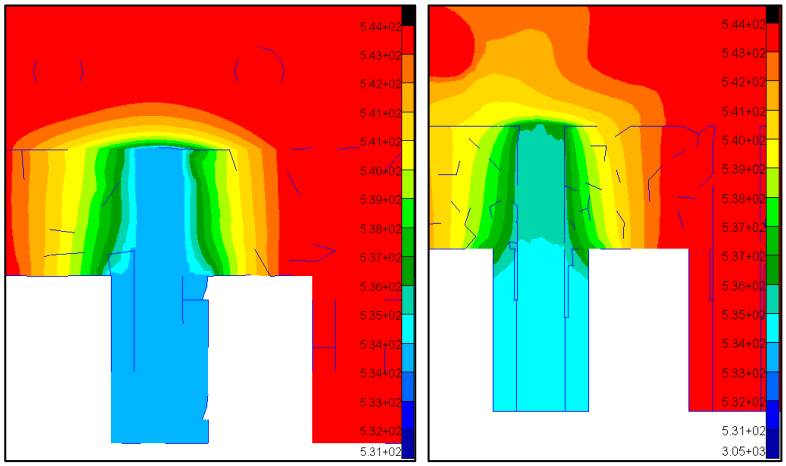

Figure 6-15: Temperature distributions at stub 17-case 7 (Left) vs case 1(Right).

From Figure 6-16, it can be seen that the difference in temperature distribution at the rear outlet branch is substantial. For load case 4, the temperature difference across the outlet branch and by implication the thermal stresses, are less than that of load case 1. The comparison indicates that the temperature profile from adiabatic heat transfer in FEA does not fully resemble the temperature profile from complex heat transfer in CFD, which included a combination of internal convection and conduction. It can thus be concluded that the effect of internal steam flow distribution plays an important role in determining the correct temperature profile for estimating thermal stresses.

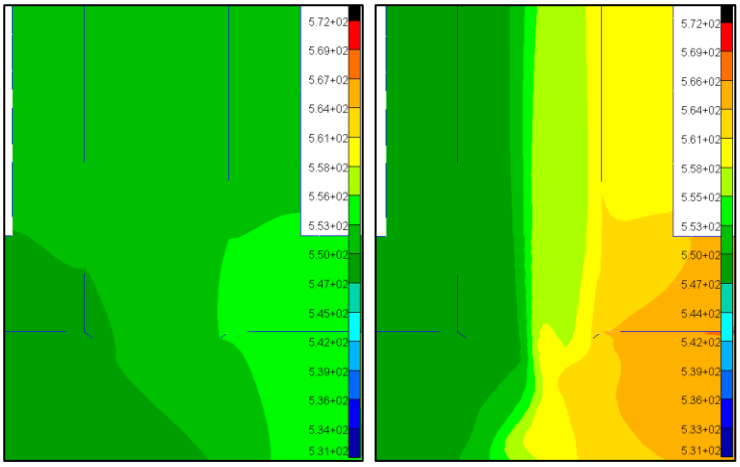

Figure 6-16: Temperature distribution at rear outlet header-Case 7 (Left) vs Case 1(Right).

6.4 FEA results

The FEA results are presented in five main categories, namely: thermal stresses, mechanical stresses, combined stresses and displacements. At the end of each result section, a summary of the results is tabulated and discussed. As mentioned in section 5.4, there are eleven different load cases. The results for each load case, was divided into each of the categories as follows:

- FEA thermal stress results: load case 1 to 7.

- FEA mechanical stress results: load case 8.
- FEA combined stress results: load case 9 to 11.
- FEA displacements: all load cases.

The description of each of the eleven load cases, as listed in section 5.4, are restated below:

Case 1 -3: FEA models for all three load conditions, using CFD results. Only stresses due to thermal expansion were considered. Case 1-3 will indicate full, 80% and 60% load respectively. The whole header was simulated using MSC Patran.

Case 4-6: FEA models for all three load conditions, using CFD results. Only stresses due to thermal expansion were considered. Case 4-6 will indicate full, 80% and 60% load respectively. A quarter of the model was simulated using MSC Patran.

Case 7: FEA model for full load, without using CFD results. Only stresses due to thermal expansion were considered, with heat transfer performed in Marc Mentat and the structural analysis performed in MSC Patran.

Case 8: FEA model for internal pressure without thermal expansion. A quarter of the model was simulated using MSC Patran.

Case 9-11: FEA models for all three load conditions, using CFD results. Stresses due to internal pressure and thermal expansion were considered. A quarter of the model was simulated using MSC Patran.

6.5 FEA thermal stress results

6.5.1 Thermal stress results for load case 1 to 3

The von Mises stress distribution fringe plots for load case 1, are shown in Figure 6-17 and Figure 6-18, with Figure 6-18 being the cross sectional view of Figure 6-17. The highest thermal stress at full load was found to be 35.5MPa at stub 27, which is located at the rear (right-hand side) outlet branch.

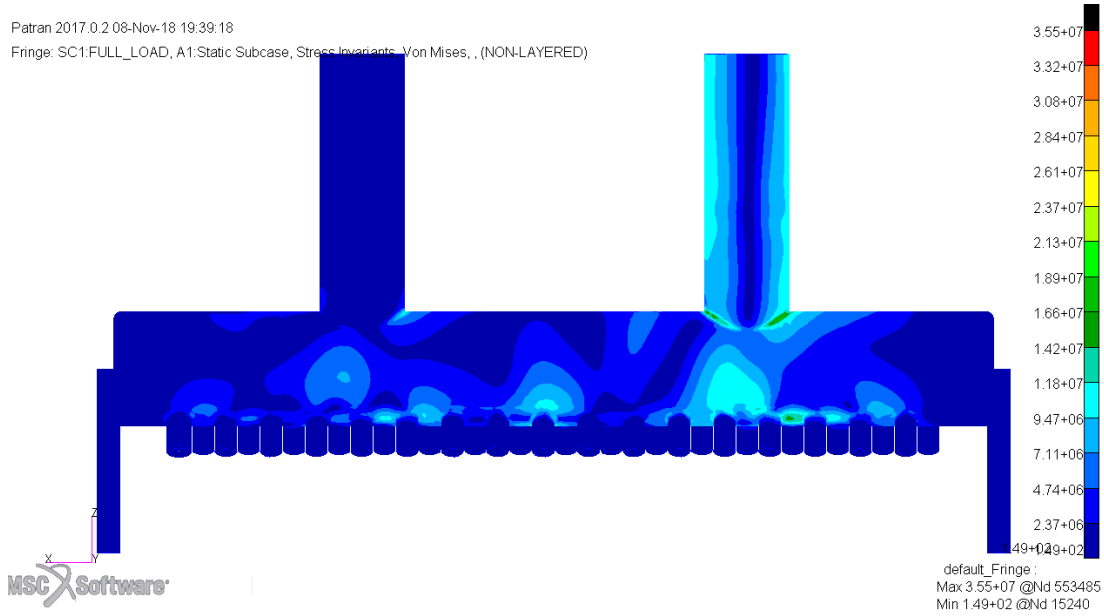

Figure 6-17: Case 1 - von Mises thermal stress distribution of the outside surface at full Load [Pa].

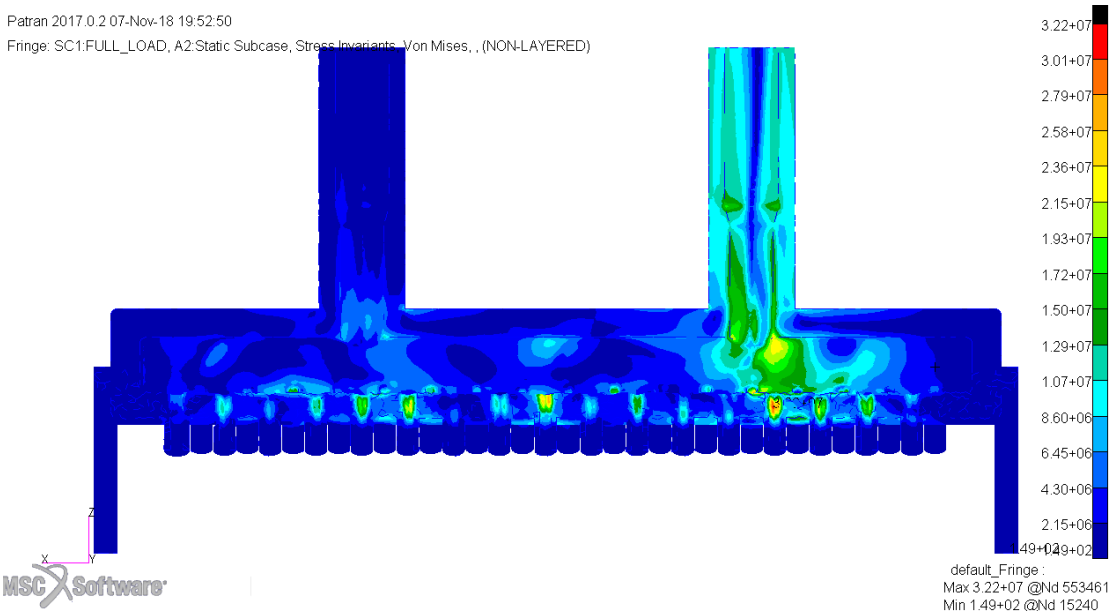

Figure 6-18: Case 1 - Cross section of von Mises thermal stress distribution at full load [Pa].

Three different nodes (see Figure 6-19 to Figure 6-21) were used to compare borehole stresses between the three different load conditions. Either end of the rear outlet branch borehole and the borehole at stub 27 were used for the locations of each of the three nodes. The highest borehole stresses were found at 80% load and correlates well with thermocouple reading in Figure 6-3, which indicated the highest temperature differences occur at 80% load.

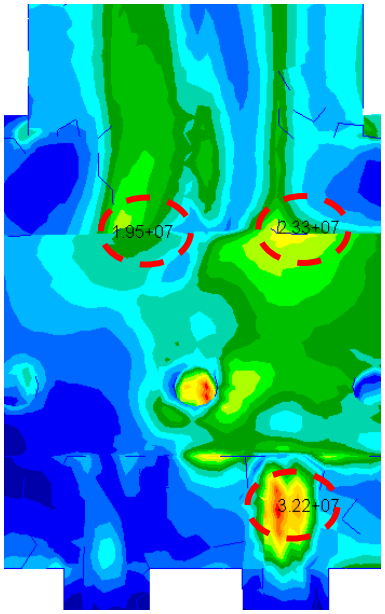

Figure 6-19: Case 1 – nodal thermal stresses at full load [Pa].

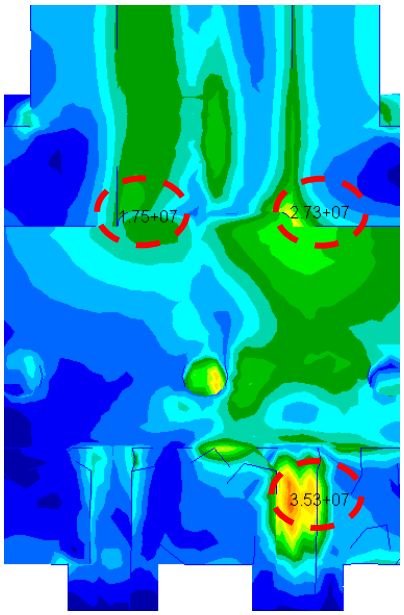

Figure 6-20: Case 2 – nodal thermal stresses at 80% load [Pa].

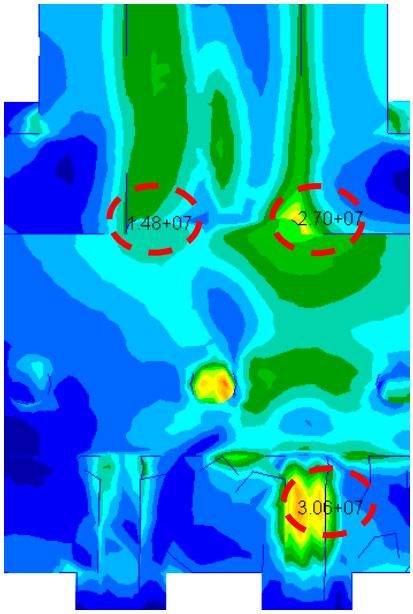

Figure 6-21: Case 3 - nodal stresses at 60% Load [Pa].

The stress range in Figure 6-22 to Figure 6-24, was set between 10MPa and 30MPa. It can be seen from the filtered stress range, that that the majority of the header is below 10MPa (dark blue region). The stresses above 10MPa are mainly found at the rear outlet branch and its associated borehole. There are also higher local stresses at the boreholes of stub 27, at the rear outlet branch, and stub 17, at the centre of the header. From the filtered stress results, it can be concluded that the front half of the header (left-hand side) does not significantly contribute to thermal stresses and can be excluded from the model.

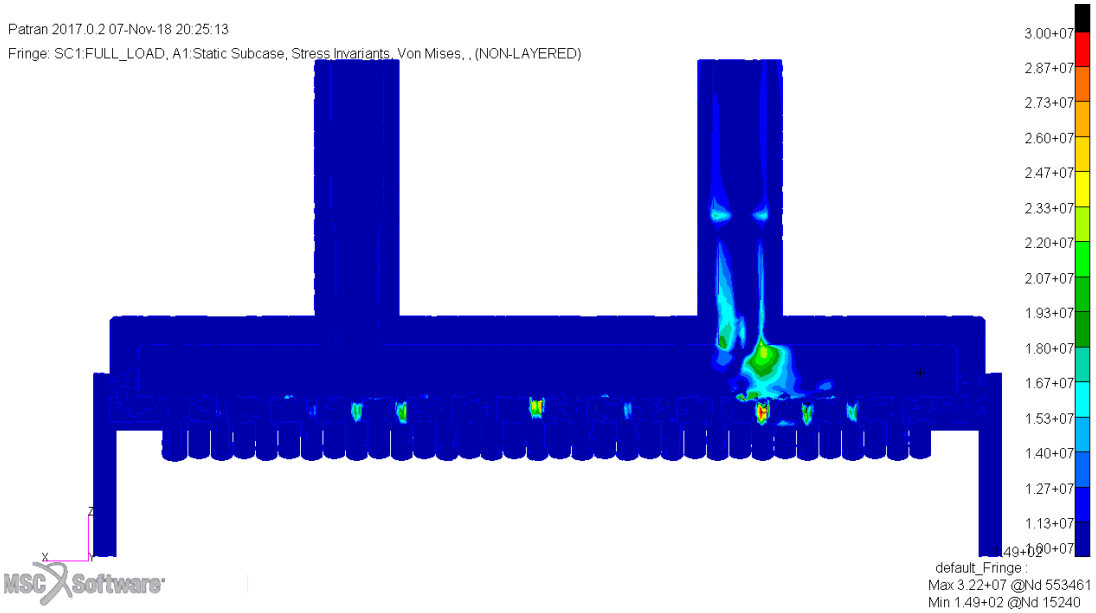

Figure 6-22: Case 1 - von Mises stress range from 10MPa to 30MPa, at full load [Pa].

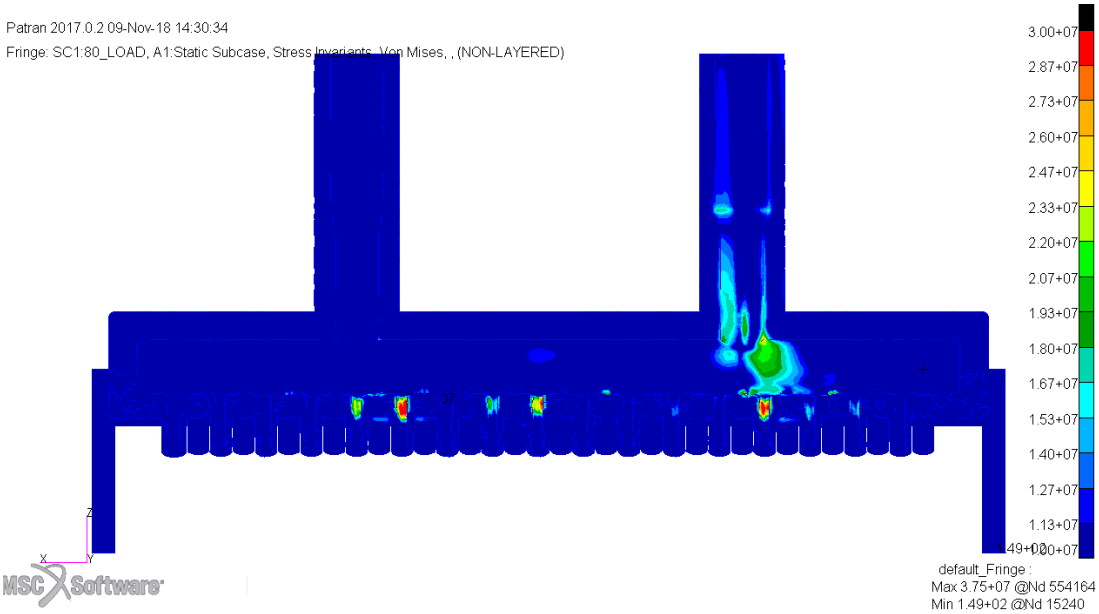

Figure 6-23: Case 2 - von Mises stress range from 10MPa to 30MPa, at 80% load [Pa].

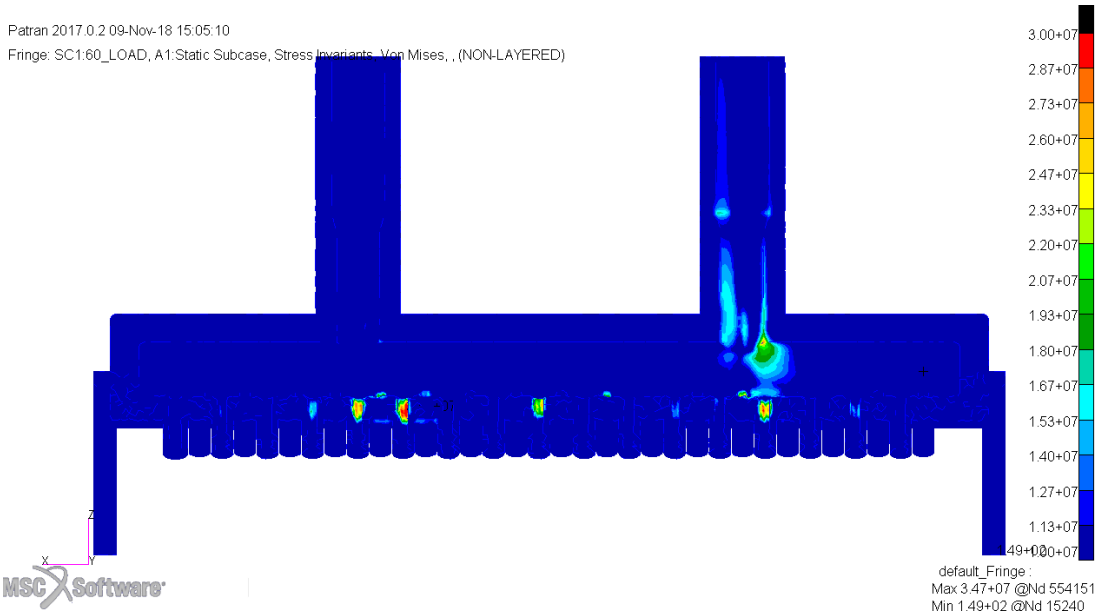

Figure 6-24: Case 3 - von Mises stress range from 10MPa to 30MPa, at 60% load [Pa].

6.5.2 Thermal stress results for load case 4 to 6

The quarter model (see Figure 6-25) represent the rear half (right-hand side) of the header, which as mentioned in the results above, is the region that experiences the highest thermal stresses. The quarter model, at the different load conditions, has similar stress values when compared to the whole model. The thermal stresses for load case 4 differed by 2.9 to 3.5MPa when compared to the load case 1 and indicated that the quarter model correlated well with the whole model. See Figure 6-26 for the thermal borehole stresses at full load. The thermal stress results for load case 4 to 6 are listed in Table 6-3.

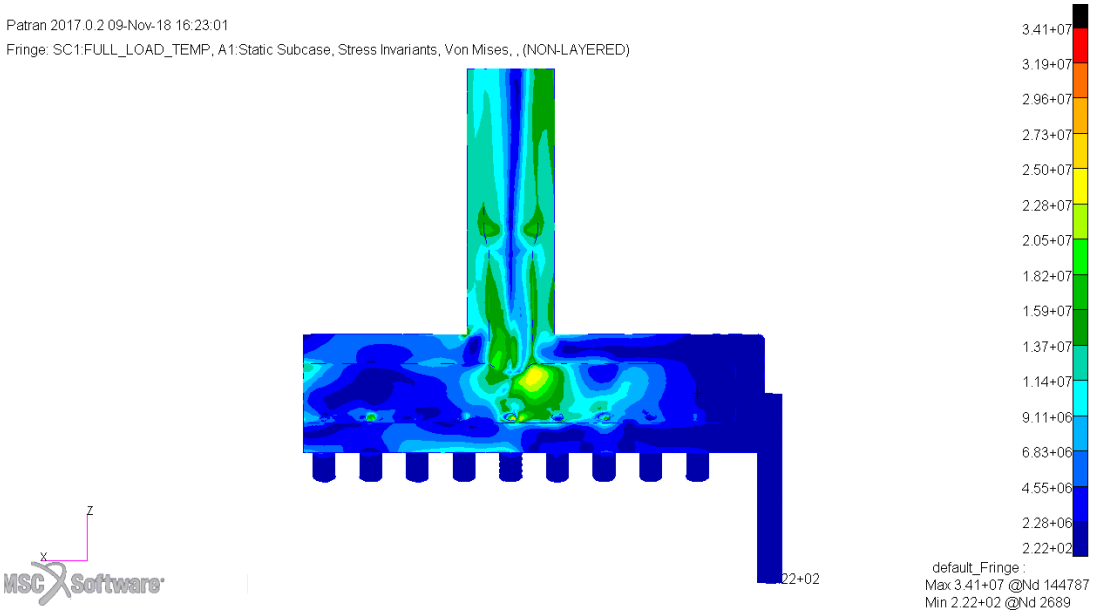

Figure 6-25: Case 4 -quarter model von Mises thermal stress distribution at full load [Pa].

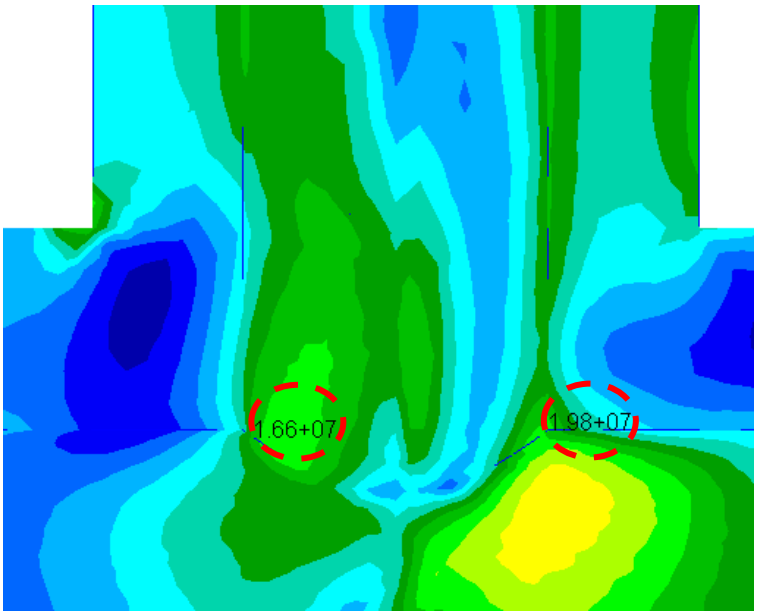

Figure 6-26: Case 4 –quarter model borehole thermal stress at full load [Pa].

6.5.3 Thermal stress results for load case 7

For load case 7, the highest thermal stress value of 37.3MPa was found at the borehole of stub 17. The thermal stress distribution in Figure 6-18, is more prominent than that of Figure 6-25 at the same load condition. The difference in thermal stress distribution between load case 1 and 7, is due to the difference in temperature distributions discussed in section 6.3.2. The temperature profile for load case 7 was more uniform across the outlet branches (see Figure 6-13) and as such the thermal stress in these regions is negligible.

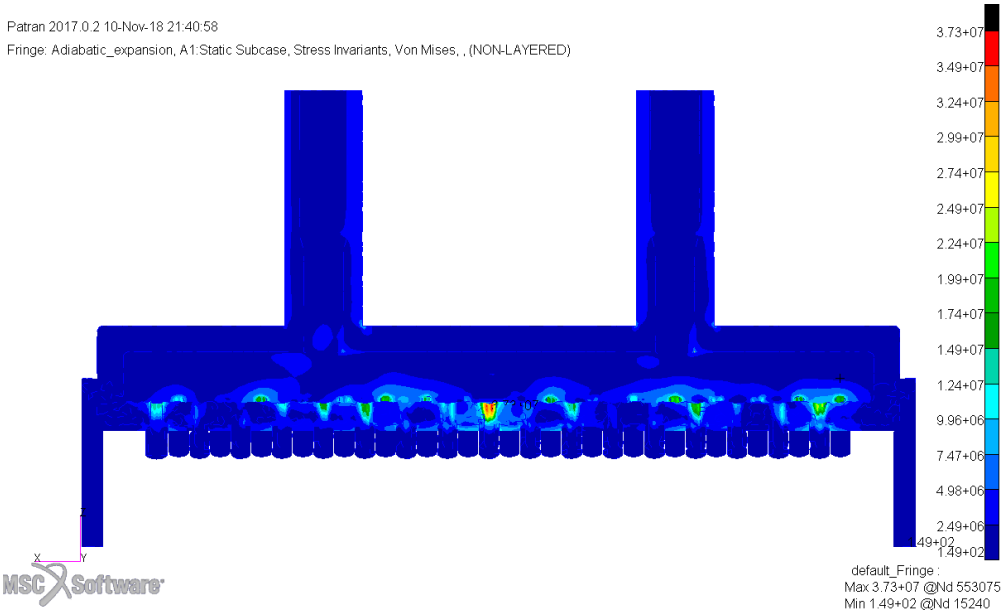

Figure 6-27: Case 7 - Cross section of von Mises thermal stress distribution at full load [Pa].

By comparing the nodal thermal stress values in Figure 6-28 to that of Figure 6-19, it is clear that rear outlet borehole stress values are considerably less for load case 7 than that of 1.

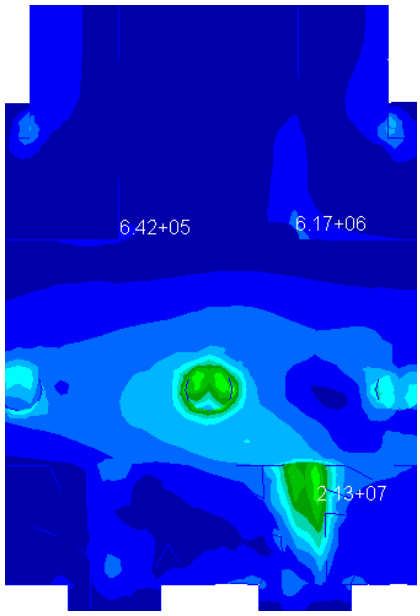

Figure 6-28: Case 7 – nodal thermal stresses at full load [Pa].

6.5.4 Thermal stress results summary for load case 1 to 7

The thermal stress results for load cases 1 to 7 are tabulated in Table 6-3. The FEA results were compared to thermal hoop stress values, calculated using the European code EN 12952-3. The calculation uses the header and outlet branch dimensions as well as the required thermal properties, to estimate the thermal hoop stress at the borehole region. The calculated thermal stress values indicate that the FEA results are within the correct range. The stress results from the

quarter model are slightly less than that of the whole model, due to the fact that the temperature distribution is not perfectly symmetrical about the planes of symmetry and because the quarter model has a finer mesh at the borehole regions. The maximum von Mises stress of 27.3MPa, for load case 2 at 80% load, is well below the 0.2% proof strength of 160MPa. The proof strength was estimated at the highest metal temperature of 577°C. The stresses caused by thermal expansion alone are not substantial. Thermal stresses at steady state conditions can contribute to other stresses caused by mechanical loads and creep.

From Table 6-3, it is shown that the stress at the outlet borehole for the uncoupled FEA method, load case 7, does not correspond with the stress values for load case 1 and 4. The comparison indicates that the steam flow distribution in a header should not be assumed to be negligible, but must rather be considered when the estimating thermal stresses.

Table 6-3: Thermal stress results.

Model description	Location of borehole stress	Whole model-von Mises [MPa]	Quarter model-von Mises [MPa]	EN 12952 Thermal hoop stress [MPa]
FEA-CFD model, only thermal stress. Full load	Rear outlet branch	23.3 (Case 1)	19.8 (Case 4)	21.4
FEA-CFD model, only thermal stress. 80% Load	Rear outlet branch	27.3 (Case 2)	25.9 (Case 5)	22
FEA-CFD model, only thermal stress. 60% Load	Rear outlet branch	27 (Case 3)	25.4 (Case 6)	21.4
FEA without CFD, only thermal stress. Full load	Rear outlet branch	6.17 (Case 7)	-	8.5

6.6 FEA mechanical stress results for load 8

For load case 8, only mechanical loads were considered. The mechanical loads described in sections 5.4.2 and 5.4.3 were applied to the stubs, together with the symmetrical displacement constraints

shown in Figure 5-18. The model was set at a uniform temperature of 566°C, which is the design temperature of the header. At a uniform temperature, there will be no internal temperature difference throughout the model and thus no thermal stresses will occur. Since the internal pressure of 16MPa stays approximately constant for all three boiler load conditions, only one mechanical model was required.

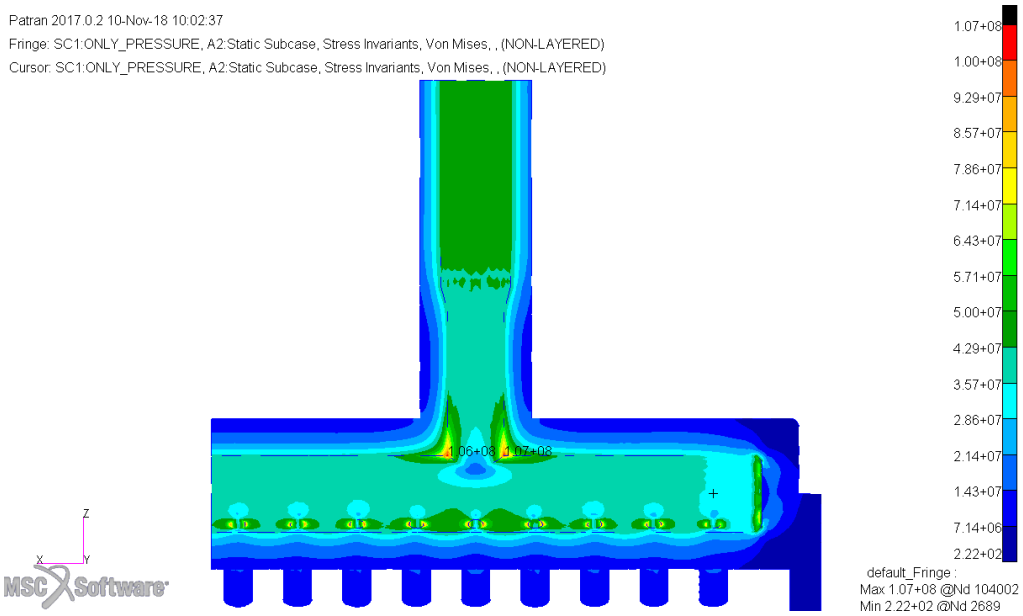

Figure 6-29: Case 8- von Mises stress distribution due to mechanical loading [Pa].

The pressure loading resulted in a symmetrical stress distribution across the rear outlet pipe, Figure 6-30, and the stubs, Figure 6-31, with either node at the same von Mises stress.

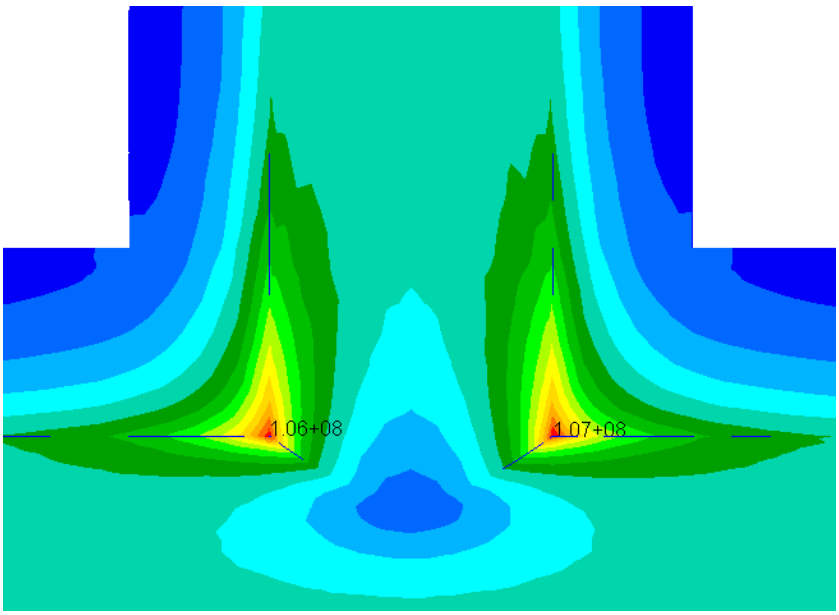

Figure 6-30: Case 8- rear outlet pipe borehole mechanical stresses [Pa].

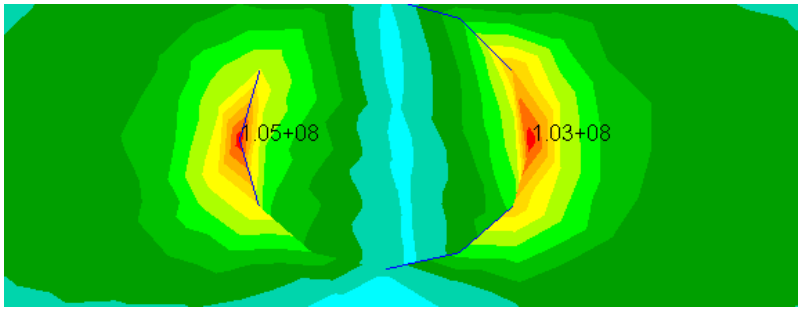

Figure 6-31: Case 8 – stub 22 borehole mechanical stress [Pa].

The mechanical FEA stress values were compared to hand calculated mechanical von Mises stresses. The hand calculations were based the European code EN 12952-3. The agreement between the values indicates that no gross input errors have been made in the FEA model and that the mesh density provides results in the correct stress range. It should be noted that the two values must not be equal to one another as the calculation does not take neighbouring header ligaments into account. See Appendix A for an example of the mechanical and thermal branch calculations, as per EN 12952.

Table 6-4: Mechanical stress results.

Model description	Location of borehole stress	Quarter model – von Mises [MPa]	EN 12952 Mechanical von Mises stress [MPa]
FEA-CFD model, only mechanical stress.	Stub 22 to the header	103 (Case 8)	89.9
	Rear outlet branch	107 (Case 8)	95.5

6.7 FEA combined stress results for load case 9 to11

For load case 9, the temperature distribution from load case 1 was added to the mechanical model used in load case 8. The mechanical stress value of 106MPa, Figure 6-30, together with the thermal stress value of 16.6MPa, Figure 6-26, approximately contributed to the combined stress of 119MPa at the rear outlet branch. See Figure 6-32 for the maximum stress at combined loads. The exact combined stress value cannot directly be calculated by adding the two stress components, but a close approximation can be estimated.

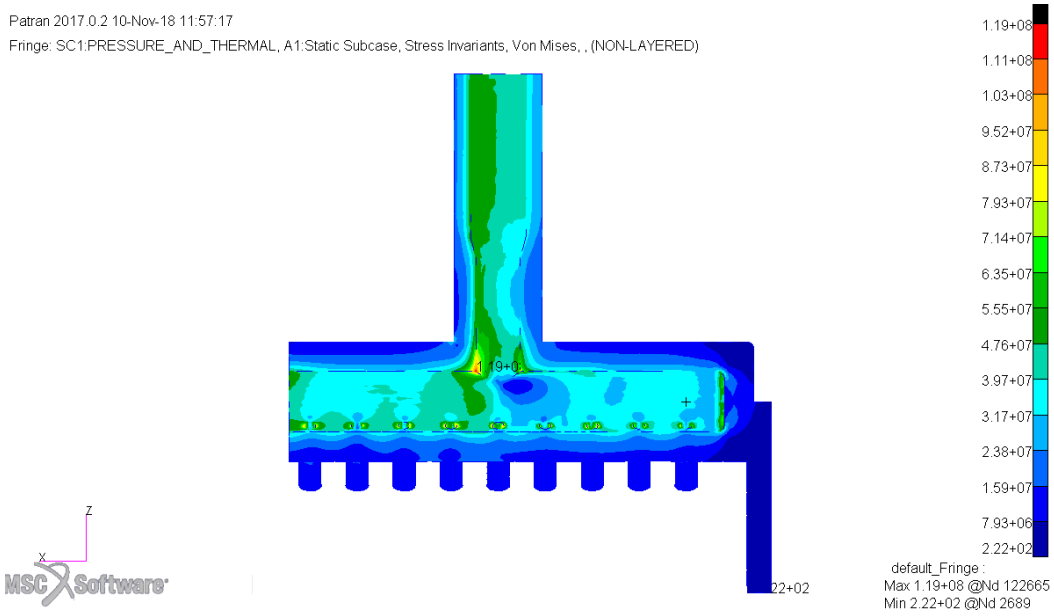

Figure 6-32: Case 9 - von Mises stress distribution due mechanical and thermal loading [Pa].

From the nodal combined stress values in Figure 6-33, it was found that one nodal stress value increased while the other nodal stress value decreased. The mechanical stress value of 107MPa, Figure 6-30, decreased by the thermal stress value of 19.8MPa, Figure 6-26, to result in a combined stress value of 87.5MPa. A possible reason for the decrease in stress at this node can be attributed to the decrease in nodal displacement. The internal pressure can cause the node to displace in the opposite direction than that of the thermal expansion and the net displacement decreases.

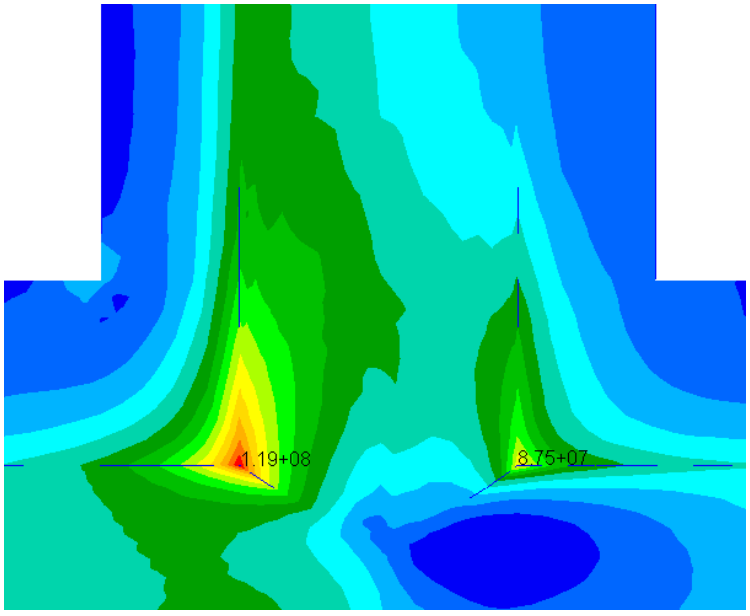

Figure 6-33: Case 9- rear outlet pipe borehole combined stresses [Pa].

6.8 FEA combined stress result summary

The stress results from load case 4 to 6 and 8 to 11 are tabulated in Table 6-5. The results indicate that in some regions the combination of mechanical and thermal loads will result in larger stresses and in other regions it will result in smaller stresses. The highest thermal stresses were found at 80% load; however the combined stress values are approximately the same for all three load conditions. The results indicate that the combined stress values at steady state conditions do not vary significantly with a change in boiler load conditions. The highest combined stress of 119MPa is less than that of the 0.2% proof strength of 160 MPa at 577°C, which indicates that no plastic deformation will occur. The combined stress values, however, are high enough that they can exacerbate the header's life by contributing to common steady state failure mechanisms, such as creep.

Table 6-5: Combined stress result summary.

Model description	Location of borehole stress	Mechanical stress [MPa]	Thermal stress [MPa]	Combined stress [MPa]
FEA-CFD model at full load	Rear outlet branch: node on the left-hand side	106 (case 8)	16.6 (case 4)	119 (case 9, stress values added)
	Rear outlet branch: node on the right-hand side	107 (case 8)	19.8 (case 4)	87.5 (case 9, stress values subtracted)
FEA-CFD model, at 80% load	Rear outlet branch: node on the left-hand side	106 (case 8)	15.4 (case 5)	118 (case 10, stress values added)
	Rear outlet branch: node on the right-hand side	107 (case 8)	25.9 (case 5)	81.5 (case 10, stress values subtracted)
FEA-CFD model, at 60% load	Rear outlet branch: node on the left-hand side	106 (case 8)	12.9 (case 6)	116 (case 11, stress values added)

Model description	Location of borehole stress	Mechanical stress [MPa]	Thermal stress [MPa]	Combined stress [MPa]
	Rear outlet branch: node on the right-hand side	107 (case 8)	25.4 (case 6)	81.9 (case 11, stress values subtracted)

The high stress values found in load case 1 to 11, were all highly localised and with a stress distribution that decreases through the thickness of the header. In order to plot the stress distribution through the thickness, a curve (see Figure 6-34) was created between the borehole notch corner and the outside surface of the header. Using the curve, a graph was created that plotted the stress distribution along the curve's distance. See Figure 6-35.

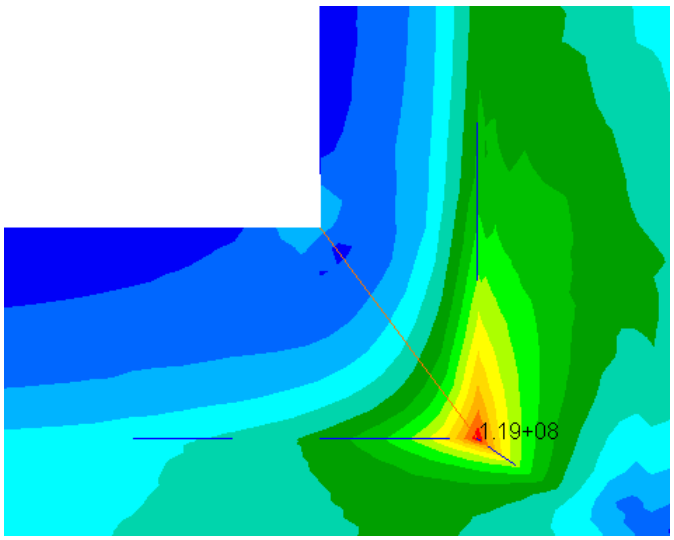

Figure 6-34: Case 9 – curve for FEA graph result [Pa].

For load case 9, the stress value sharply decreased through the thickness of the header's walls. From the graph it can be concluded that the highest stresses in a header occur at the borehole crotch corner.

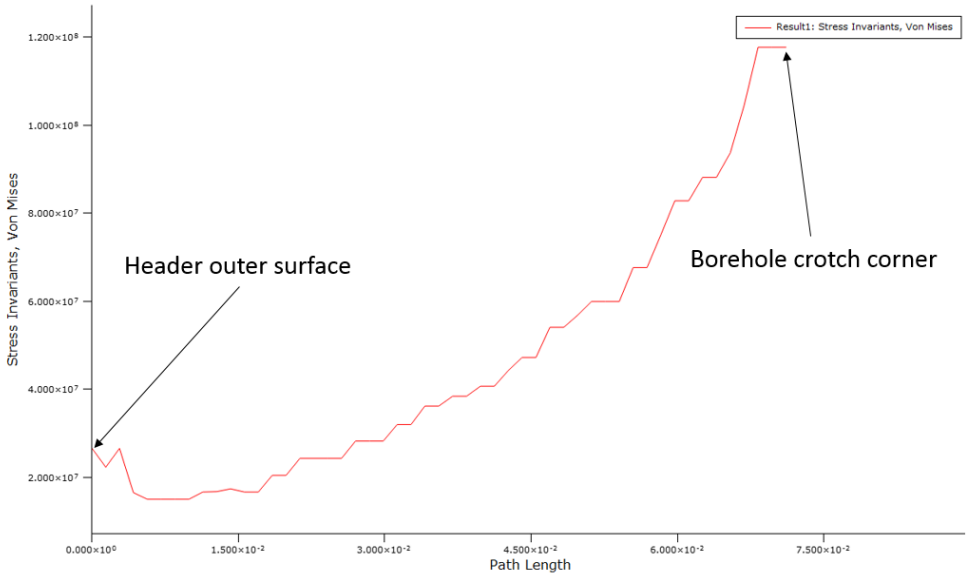

Figure 6-35: Case 9 -von Mises stress distribution along specified curve at full load [Pa].

6.9 FEA thermal displacements

By observing the displacements in FEA, it can be determined whether the constraints have correctly been applied. The displacement magnitude ,for load case 2, is shown in Figure 6-36 and it correctly indicates that the header is constrained so that it can only expand sideways and downwards without rotating. The highest thermal stress values of the three load conditions were found at 80% load, load case 2, and subsequently the highest displacements were also found at 80% load.

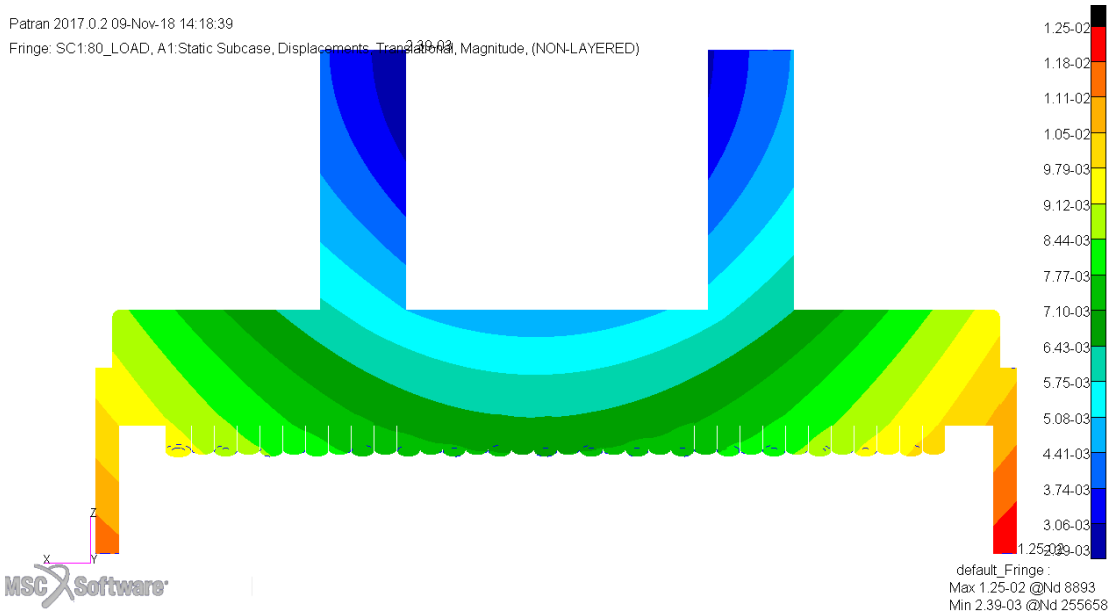

Figure 6-36: Case 2 -magnitude of displacement at 80% load [mm].

The maximum displacement in the X-direction, see Figure 6-37, was 7.78mm towards the front (left hand side) and 8.4mm towards the rear (right hand side).

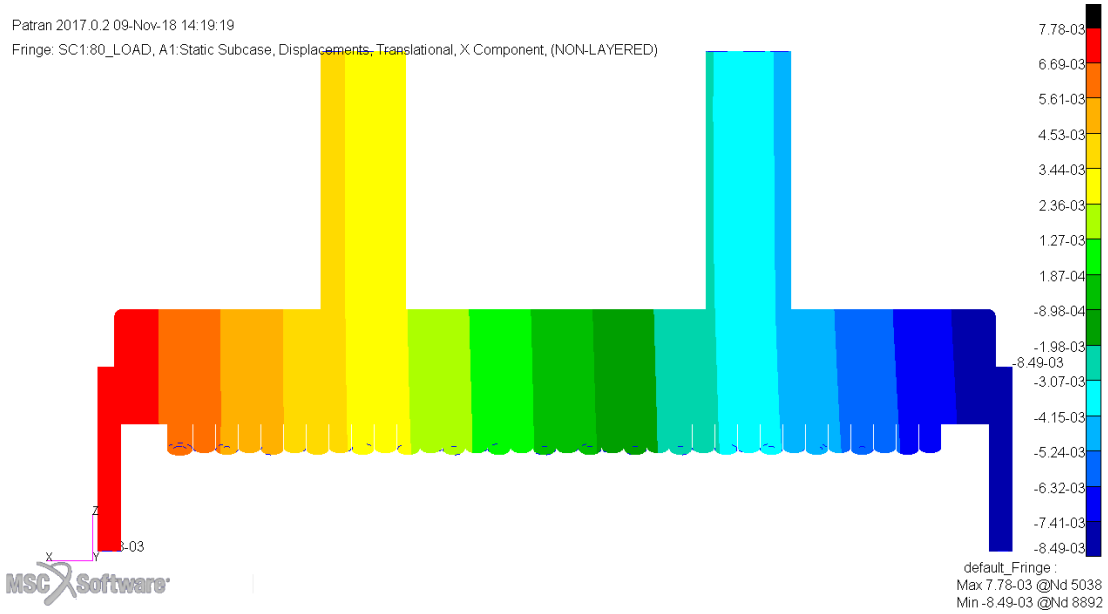

Figure 6-37: Case 2 -displacement in the X-direction at 80% load [mm].

The symmetrical constraints applied to the quarter model, resulted in almost identical displacements than that of the whole model. See Figure 6-38 for the displacements in the x-direction of the quarter model at 80% load.

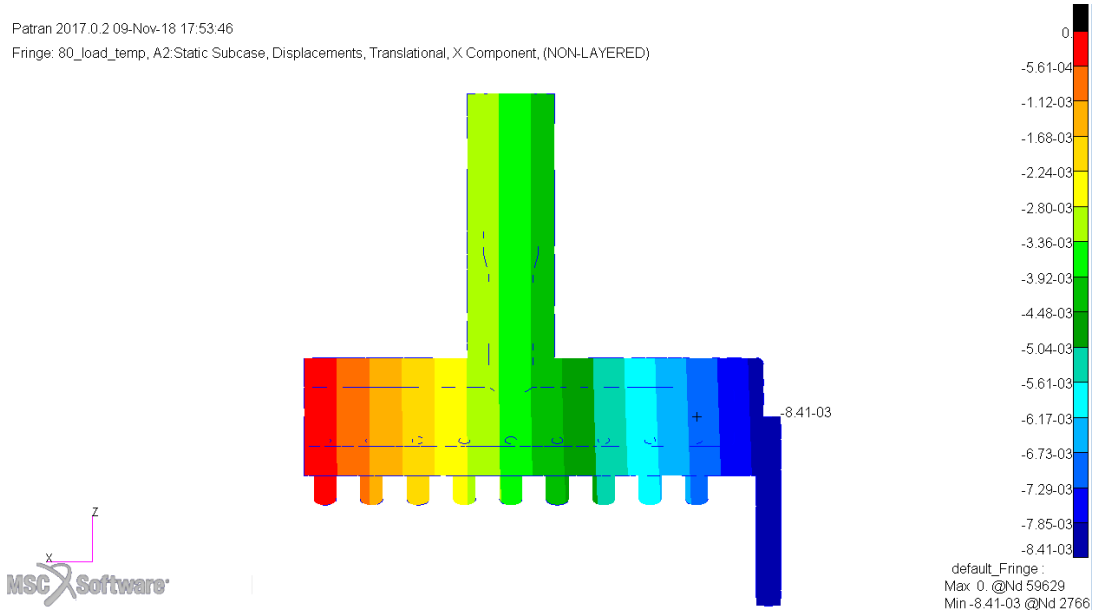

Figure 6-38: Case 5 - displacement in the X-direction at 80% load [mm].

The constraints only permit the header to expand downwards and thus Figure 6-39 correctly shows that negative displacement in the Z-direction with a maximum value of 9.31mm. The downward displacement in Figure 6-40 is at 9.2mm.

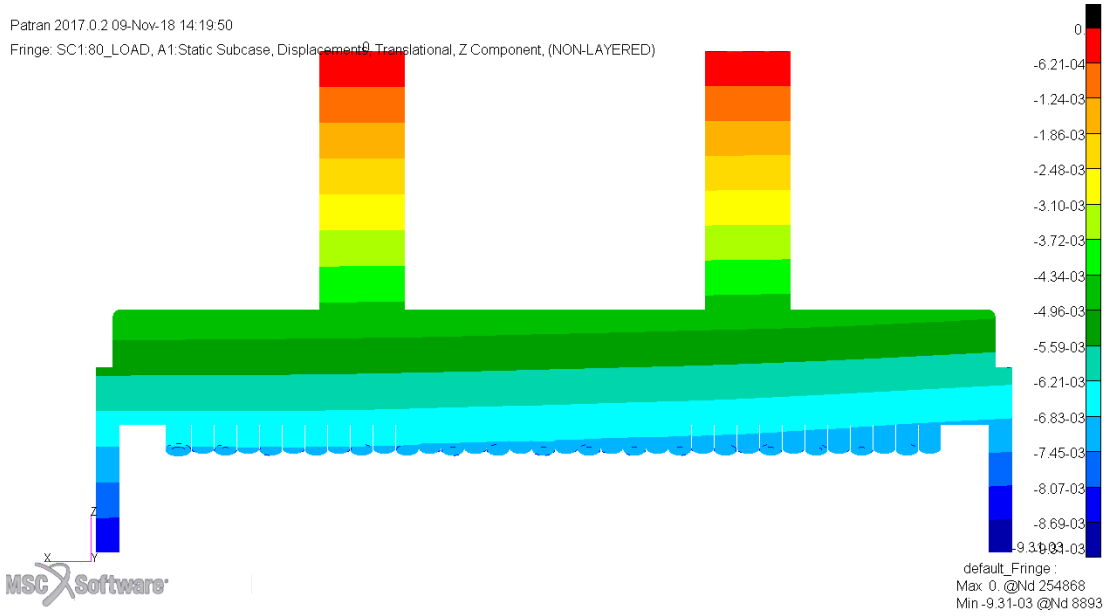

Figure 6-39: Case 2 - displacement in the Z-Direction at 80% load [mm].

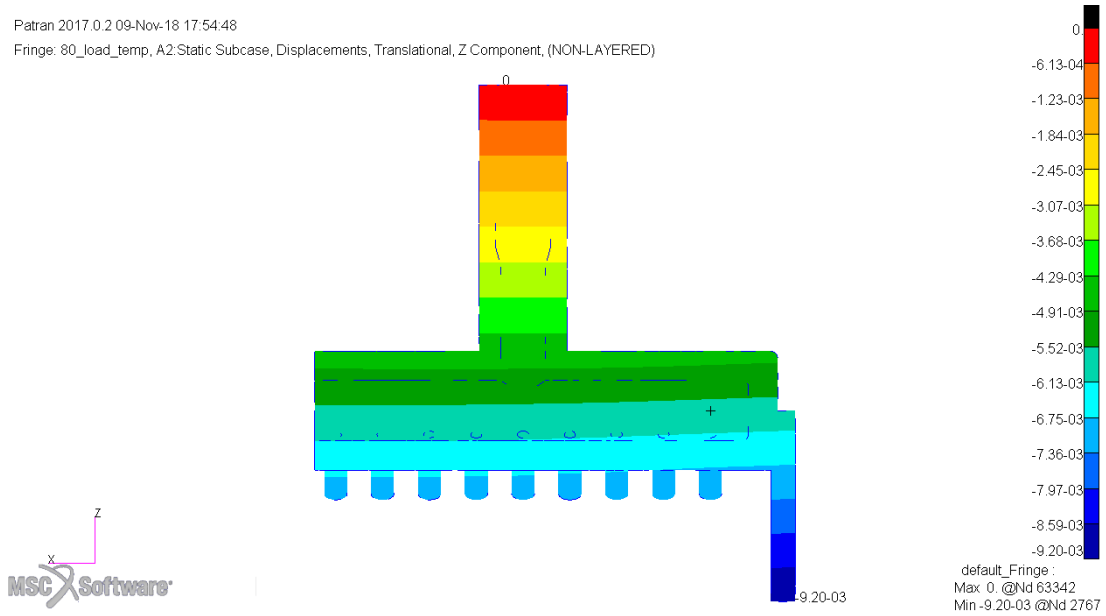

Figure 6-40: Case 5 - displacement in the Z-direction at 80% load [mm].

The summary of the displacement results for each of the load case 1 to 6 are shown in Table 6-6. The differences in displacements are marginal between the three load conditions, with the highest difference being 0.11mm. The displacements found for the mechanical and combined stress models were close to identical to that of the thermal expansion.

Table 6-6: FEA thermal displacement results [mm].

FEA Load Case	Load Condition	Displacement towards the front of the Boiler [mm]	Displacement towards the rear of the Boiler [mm]	Displacement Z-direction [mm]
Case 1	100%	7.75	8.42	9.23
Case 2	80%	7.78	8.49	9.31
Case 3	60%	7.72	8.41	9.2
Case 4	100%	-	8.35	9.13
Case 5	80%	-	8.41	9.2
Case 6	60%	-	8.33	9.09

7. Conclusion and future work

It is evident from the thermocouple measurements that there were temperature differences across the final superheater headers. The temperature differences can be attributed to the difference in superheater tube lengths inside the boiler, as longer tubes have larger surface areas and thus more heat is transferred to these tubes. The headers were designed for thermal expansion due to these temperature differences and thus external constraints do not impose stresses on the header material. Only internal constraints caused by local temperature differences within the header material, resulted in thermal stresses at the borehole crotch corners. The highest thermal stress values were located at the borehole of the rear outlet branch and stub borehole connections and occurred during partial loads. The extent of thermal stresses at the three quasi-steady state conditions matched the EN 12952 calculations and indicated that the adiabatic CFD assumption as well as the CFD mass flow estimation resulted in stresses in the correct range. The stresses due to pressure only also correlated well with the EN 12952 calculations (see Appendix A) and indicates that the FEA displacement boundary conditions were valid and that a quarter model can be used to simplify FEA simulations. The difference between the combined stress models (case 9 to 11) and the pressure model (case 8) was found to be approximately that of the thermal stress values from case 4 to 6. The thermal stresses, although small in magnitude, do occur at steady state conditions and together with the mechanical loads resulted in higher stresses. The maximum combined stress of 119MPa, at full load, is below that of the 0.2% proof strength of 160MPa, indicating that no plastic deformation will occur. The combined stress values, however, are high enough that they can exacerbate the header's life by contributing to common steady state failure mechanisms, such as creep.

For future work it is recommended to proceed with quasi-steady state conditions but include creep damage in the FEA analysis. The combination of local thermal expansion and pressure loads can possibly accelerate creep damage. It is also further recommended to look at transient conditions, as these conditions lead to greater thermal stress distributions through the header wall and between the header and the connecting stubs. A preliminary Flownex model was created for the mass flow estimation. However, further development of Flownex header models should be investigated, especially in terms of calibrating the Flownex models to match that of the CFD models, the major focus points being to estimate the pressure loss factors due to the header's geometry as well as the correct mass flow distribution through the header.

8. List of references

[1] S. Kakac and H. Liu, HEAT EXCHANGERS Selection, Rating and Thermal Design, Florida: CRC PRESS, 2002.

[2] V. Viswanathan and D. Gray, “Damage to power plants due to cycling,” EPRI, California, 2001.

[3] A. Fabricius and P. Jackson, “Premature Grade 91 failures-worldwide plant operational,” *Engineering Failure Analysis,* pp. 398-406, 2016.

[4] H. Thielsch, R. Smoske, F. Cone and J. Husband, “Failure analysis of superheater outlet header,” Thielsch Engineering, Cranston, 2000.

[5] R. Tilley, “Impact of Operating Factors on Boile Availability,” EPRI, California, 2006.

[6] I. Paterson and J. Wilson, “Use of damage monitoring systems for component life optimisation in power plant,” *International Journal of Pressure Vessels and Piping,* pp. 541-547, 2002.

[7] J. King, “Condition Assessment of Boiler Piping and Header Components,” Babcock Power Inc, Washington, 2000.

[8] J.Nakoneczny and C.Schultz, “Life Assessment of High Temperature Headers,” Babcock & Wilcox, Ohio, 1995.

[9] M. Myers and I. Rawlings, “Unstable steam and thermal fatigue,” Aurecon, Queensland, 2012.

[10] H. Roy, D. Ghosh, P. Roy, A. Saha, A. Shukla and J. Basu, “Failure investigation of Platen Superheater Outlet Header,” ResearchGate, Durgapur, 2010.

[11] O. Kwon, M. Myers, A. Karstensen and D. Knowles, “The effect of the steam temperature fluctuations during steady state operation on the remnant life of the superheater header,” *International Journal of Pressure Vessels and Piping,* vol. 83, pp. 349-358, 2006.

[12] L. Xu, J. Khan and Z. Chen, “Thermal load deviation model for superheater and reheater of a utility boiler,” *Applied Thermal Engineering,* vol. 20, pp. 545-558, 2000.

[13] T. Farragher, S. Scully, N. O'Dowd and S. Leen, "Development of life assessment procedure for power plant headers operated under flexible loading scenarios," *International Journal of Fatigue,* vol. 49, pp. 50-61, 2013.

[14] O. Yasniy, Y. Pyndus, V. Brevus, V. Iasnii and Y. Lapusta, "Lifetime estimation of superheater header," *Procedia Structural Intergrity,* vol. 2, pp. 840-846`, 2016.

[15] J. Okrajni, "Thermo-mechanical fatigue conditions of power plant components," *Journal of achievements ,* vol. 33, no. 1, 2009.

[16] S. Lalot, P. Florent, S. Lang and A. Bergles, "Flow maldistribution in heat exchangers," *Applied Thermal Engineering,* vol. 19, pp. 847-863, 1999.

[17] M. Gandhi, A. Ganguli, J. Joshi and P. Vijayan, "CFD simulation for steam distribution in header and tube assemblies," *Chemical Engineering Research and Design,* vol. 90, pp. 487-506, 2012.

[18] A. Kandil, "Analysis of thick-walled cylindrical pressure vessels under the effect of cyclic internal pressure and cyclic termperature," *International Journal Mechanical Science,* vol. 38, pp. 1319-1332, 1996.

[19] A. Shahani and S. Nabavi, "Analytical solution of the quasi-static thermoelasticity problem in a pressurized thick-walled cylinder subjected," *Applied Mathematical Modelling,* vol. 31, pp. 1807-1818, 2007.

[20] I. Al-Zaharnah, "Thermal Stresses in Pipes," Dublin City University, Dublin, 2002.

[21] L. He and M. Oldfiled, "Unsteady Conjugate Heat Transfer Modeling," *Journal of Turbomachinary,* vol. 133, 2011.

[22] F. Larsson, "Transferring Information from CFD to FE Thermal Analysis," CHALMERS University of Technology, Gothenburg, 2016.

[23] Z. Sun, J. Chew, N. Hills and K. Volkov, "Efficient Finite Element Analysis/Computational Fluid Dynamics Thermal Coupling for Engineering Applications," *Journal of Turbomachinary,* vol. 132, 2010.

[24] J. Dixon, A. Guijarro Valencia, P. Ireland and P. Ridland, "A COUPLED CFD FINITE ELEMENT ANALYSIS METHODOLOGY IN A BIFURCATION PIPE IN A NUCLEAR PLANT HEAT EXCHANGER," Rolls-Roycs plc, Guilford, 2010.

[25] J. Holman, Heat Transfer- Tenth Edition, New York: McGraw-Hill , 2010.

[26] T. B. a. W. Company, STEAM-its generation and use 41st Edition, The Babcock and Wilcox Company.

[27] Y. A. Cengel, HEAT AND MASS TRANSFER - A Practical Approach Third Edition.

[28] "ASME VIII- Division 2," 1998, pp. 339-341 Appendix 4.

[29] "Calcstress," Stress, [Online]. Available: http://www.calcstress.com/combined-stress. [Accessed 15 11 2016].

[30] T. Chanyalew, "Thermal stresses and creep analysis of boiler tubes," Addis Adaba University, Addis Adaba, 2004.

[31] H. Jahed and J. Bidabadi, "An axisymmetric method of creep analysis for primary and secondary creep," *Journal of Pressure Vessels and Piping,* pp. 597-606, 2003.

[32] "EN 13445-3 Unfired pressure vessels," 2012, p. Annex B.

[33] R. G. Budynas and J. Nisbett, Shigley's Mechanical Engineering Design-Ninth edition, New York: McGraw-Hill, 2011.

[34] "Stress in Thick Tubes or Cylinders," The Engineering Toolbox, [Online]. Available: http://www.engineeringtoolbox.com/stress-thick-walled-tube-d_949.html. [Accessed 15 11 2016].

[35] R. Barron and B. Barron, Design for Thermal Stresses, New Jersey: John Wiley & Sons, 2012.

[36] R. Bhaskaran and L. Collins, "Introduction to CFD Basics".

[37] J. Wendt, Computational Fluid Dynamics- An Introduction, Heidelberg: Springer, 2009.

[38] D. Logan, A First Course in the Finite Element Method, Thomson Canada Limited, 2007.

[39] M. Duff and J. Towey, “Two Ways to Measure Temperature Using Thermocouples Feature Simplicity,Accuracy and Flexibility,” *Analog Dialogue,* Vols. 44-10, 2010.

[40] K. Schreve, “Statistics of Measurements and Reliability,” EPPEI, Statistics, 2015.

[41] “FloEFD Technical Reference Software Version 15,” Mento Graphics Corporation, Oregon, 2015.

[42] E. R. Van Driest, “On Turbulent Flow Near a Wall,” *Journal on the Aeronautical Science,* vol. 23, no. 10, p. 1007, 1956.

[43] K. Vosloo, “Report on design by analysis of stub headers for Lethabo Power Station,” Babcock International Group| Africa Division Ntuthuko Generation, Bedfordview, 2015.

[44] E. Wang, T. Nelson and R. Rauch, “Back to Elements-Tetrahedra vs Hexahedra,” CAD-FEM GmbH, Munich.

[45] *Linear Static Analysis Using MSC Nastran and Patran - NAS 120 Course Notes,* MSC Software Corporation, 2014.

[46] G. Jackson, H. Chen and D. Tripping, “Shakedown of creep rupture assessment of a header branch pipe using the linear mathcing method,” *Procedia Engineering,* vol. 130, pp. 1705-1718, 2015.

[47] R. G. Budynas and J. K. Nisbett, Shigley's Mechanical Engineering Design Ninth Edition, New York: The McGraw-Hill, 2011.

Appendix A.

The branch borehole stresses as per EN 12952 are shown below and were used to estimate the borehole stresses due to pressure and thermal loading respectively. The calculated von Mises stresses are shown in Table 6-4.

1.Branch Borehole Stress due to Pressure

1.1 Process Inputs:

$P := 16MPa$ Operating pressure

$e_{ms} := 57mm$ Header thickness

$e_{mb} := 42.5 \cdot mm$ Outlet branch thickness

$ID_s := 116.8 \cdot mm$ Header ID

$ID_b := 86mm$ Stub ID

1.2 Geometry Factor Calculations:

$d_{mb} := ID_b + e_{mb} = 128.5 \cdot mm$ Mean branch diameter

$d_{ms} := ID_s + e_{ms} = 173.8 \cdot mm$ Mean shell/header diameter

$$\xi := \frac{d_{mb}}{d_{ms}} \sqrt{\frac{d_{ms}}{2 \cdot e_{ms}}} = 0.913$$

$$A1 := -1.14 \left(\frac{e_{mb}}{e_{ms}} \right)^2 - 0.89 \left(\frac{e_{mb}}{e_{ms}} \right) + 1.43 = 0.133$$

$$B := 0.326 \left(\frac{e_{mb}}{e_{ms}} \right)^2 - 0.59 \left(\frac{e_{mb}}{e_{ms}} \right) + 1.08 = 0.821$$

$\alpha_m := 2.2 + e^{A1 \cdot \xi^B}$ $\alpha_m = 3.259$ Correction of pressure stress.

1.3 Pressure Stress at Borehole Crotch Corner:

$\sigma_{tang\_press} := \frac{\alpha_m \cdot d_{ms}}{2e_{ms}} \cdot P = 79.509 \cdot MPa$ Pressure hoop stress

$\sigma_{rad\_press} := -P = -16 \cdot MPa$ Pressure radial stress

$\sigma_{axial\_press} := -P = -16 \cdot MPa$ Pressure longitudinal stress

---

$\sigma 1 := \sigma_{tang\_press}$

$\sigma 2 := \sigma_{rad\_press}$

$\sigma 3 := \sigma_{axial\_press}$

$$\sigma_{VM} := \frac{1}{\sqrt{2}} \cdot \sqrt{(\sigma 1 - \sigma 2)^2 + (\sigma 2 - \sigma 3)^2 + (\sigma 3 - \sigma 1)^2} = 95.5 \cdot MPa$$

2.Branch Borehole Stress due to Temperature Difference

2.1 Process Inputs:

$h_f := 1000$ Recommended unitless heat transfer coefficient for steam.

$z_d := \frac{d_{mb}}{d_{ms}} = 0.739$

$$\alpha_t := \left[\left[\left(2 - \frac{h_f + 2700}{h_f + 1700} \right) (z_d) + \frac{h_f}{(h_f + 1700)} \left(e^{-7 z_d} \right) - 1 \right]^2 + 0.81 \cdot z_d^2 \right]^{0.5} = 0.852$$

$T_{o1} := 556$ Temperature outside header, at reat outlet branch

$T_{i1} := 554$ Temperature inside header at borehole crotch corner

$T_o := (T_{o1} + 273.15)K = 829.15\,K$

$T_i := (T_{i1} + 273.15)K = 827.15\,K$

$\Delta t := T_o - T_i = 2\,K$ Temperature difference

$t_m := \frac{T_{o1} + T_{i1}}{2} = 555$ Mean temperature

2.2 Youngs Modulus Polynomial Equation

$E_t := \left[213.16 - 6.91 \cdot 10^{-2}(t_m) - 1.824 \cdot 10^{-5}(t_m)\right]GPa = 174.799 \cdot GPa$

2.3 Thermal Expansion Polynomial Equation

$\beta_{Lt} := \left[10.98 + 1.623 \cdot 10^{-2}(t_m) - 1.287 \cdot 10^{-5}(t_m)\right] \cdot 10^{-6}(K)^{-1} = 1.998 \times 10^{-5}\,\frac{1}{K}$

2.4 Thermal Stress at Borehole Crotch Corner:

$\nu := 0.3$ Poisson ratio for steel

$\sigma_{tang\_\Delta t} := \alpha_t \cdot \frac{\beta_{Lt} \cdot E_t}{1 - \nu} \cdot \Delta t = 8.504 \cdot MPa$ Thermal hoop stress